An Environmentally Friendly and Cost-Free Catalyst with Exceptionally High and Stable Performance for CO_x-Free Hydrogen Generation from Ammonia: Red Mud Modified by Simple Treatments

by

Samira Fatma Kurtoğlu

A Dissertation Submitted to the
Graduate School of Sciences and Engineering
in Partial Fulfillment of the Requirements for
the Degree of

Master of Science
in
Chemical and Biological Engineering

KOÇ UNIVERSITY

August 12, 2016

Koç University

Graduate School of Sciences and Engineering

This is to certify that I have examined this copy of a master's thesis by

Samira Fatma Kurtoğlu

and have found that it is complete and satisfactory in all respects,
and that any and all revisions required by the final
examining committee have been made.

Committee Members:

____

Asst. Prof. Alper Uzun

____

Prof. Ahmet Erhan Aksoylu

____

Assoc. Prof. Uğur Ünal

Date: ______________________

ABSTRACT

Hydrogen, considered as one of the most promising alternative energy carriers, faces storage and transportation problems due to its very low boiling point, extremely low density in gaseous phase and very high density in liquid phase. Therefore, the utilization of ammonia as a storage medium for hydrogen can be a solution to the safe and effective storage problem of hydrogen. Because, it is carbon free, has a high hydrogen density (17.7 wt.%), and has an already existing infrastructure. Best performing catalysts for hydrogen production by ammonia decomposition are Ru-based catalysts suffering from high costs, whereas Ni- and Fe-based counterparts have significantly lower costs. Red mud is a by-product formed during the alumina production process, produced approximately two tons for each ton of aluminum produced. It is considered as a hazardous industrial waste due to its high alkalinity and toxic content, which makes it harmful to the environment. It contains compounds which are the oxides of mainly Fe, Al, Si, and Ti. These elements makes red mud attractive in utilizing it in application areas such as ceramics, construction, and catalysis. In this thesis, Turkish red mud, from Seydişehir, with an iron oxide content of more than 35%, was converted into a cost-free catalyst for hydrogen production by ammonia decomposition with record high stable performance. Firstly, as received red mud was subjected to simple treatment methods including acid digestion followed by ammonia precipitation to enhance the physical and chemical properties. While performing these modifications, treatment parameters were systematically varied and resulting samples were deeply characterized by XRD, XRF, and FTIR spectroscopy, SEM, TGA, and ICP-MS before and after modification. The parameters which were investigated were the type of acid used for digestion (HCl and H_2SO_4), molarity of the acid (2M-6M), digestion temperature (85 and 220 °C), and calcination temperature (300 - 500 °C). In general, in the modified samples, iron oxide amount was enhanced and surface area values were increased. After performing the catalytic activity measurements of these modified red mud samples at 500 °C, it was revealed that the sample with the highest

surface area value of 232 m^2/g (that was digested at 220 °C in 6M HCl, MRM-2) has an exceptionally high activation energy indicating a high temperature dependency. Thus, this modified red mud sample was further investigated for hydrogen production by ammonia decomposition at a higher temperature, at 700°C. MRM-700R@700 provided stable 97 ± 0.5 % conversion for a space velocity of 72 000 cm^3 NH_3 h^{-1} g_{cat}^{-1} at 700 °C, which is a record high value among all non-noble metal catalyst reported in the literature. It was elucidated that an activation period of 10 h under NH_3 flow prior to the reaction forms the nitrided iron specie ε-Fe_2N in MRM-700R@700, which is responsible for this high and stable performance. Detailed feasibility study was also performed on the economics of hydrogen production on such a cost-free catalyst based on these performance values. Utilization of red mud as a catalyst for hydrogen production by ammonia decomposition provides opportunities for i) the utilization of such a hazardous waste produced in vast amounts; ii) having a cost-free, highly active and stable catalyst for CO_x-free hydrogen production by ammonia.

ÖZET

Fosil yakıtlara alternatif en çok umut vadeden enerji taşıyıcısı hidrojenin depolanmasında ve taşınmasında, hidrojenin oldukça düşük kaynama sıcaklığı, gaz fazında düşük yoğunluğu ve sıvı fazda yüksek yoğunluğu gibi özelliklerinden dolayı, sorunlarla karşı karşıya kalınmaktadır. Bu sebeple, hidrojenin güvenli ve etkili depolanmasına bir çözüm olarak amonyağın bir depolama aracı olarak kullanılması önem kazanmaktadır. Çünkü amonyak karbon içermemekte, kütlece oldukça yüksek bir miktarda hidrojen içermekte (%17.7) ve var olan altyapısı sayesinde taşınmasında sorun yaşanmamaktadır. Amonyaktan hidrojen üretme tepkimesi için en yüksek performansı gösteren katalizörler yüksek maliyetli Ru bazlı katalizörlerdir ve bu katalizörlere alternatif Ni ve Fe bazlı katalizörler önemli ölçüde daha az maliyetlidir. Kırmızı çamur, alüminyum üretimi esnasında her bir ton alüminyum üretilirken iki ton açığa çıkan bir endüstriyel atıktır. Kırmızı çamur, yüksek alkalilik ve içerdiği bazı toksik malzemelerden dolayı tehlikeli atıklar kategorisinde yer alarak çevre için bir tehdit oluşturmaktadır. İçeriğinde Fe, Al, Si ve Ti gibi elementlerin oksitleri bulunmaktadır. Kırmızı çamur, içerdiği bu malzemeler dolayısıyla seramik, yapı malzemeleri ve kataliz gibi alanlarda kullanılmak için oldukça uygundur. Bu tezde, Seydişehir Eti Alüminyum'dan alınan % 35'den fazla demir oksit içeren kırmızı çamur, amonyaktan hidrojen üretme reaksiyonu için maliyeti olmayan, yüksek ve stabil performans gösteren bir katalizöre dönüştürülmüştür. İlk olarak, fabrikadan geldiği haliyle olan kırmızı çamur, asitte çözme ve ardından sıvı amonyak ile çöktürme gibi basit muamele yöntemlerine maruz bırakılmış ve bu sayede fiziksel ve kimyasal özelliklerinin geliştirilmesi sağlanmıştır. Bu modifikasyon yöntemlerini uygularken, muamele parametreleri sistematik bir biçimde değiştirilmiş ve muameleden önce ve sonra numuneler ayrıntılı bir şekilde XRD, XRF ve FTIR spektroskopisi ile, SEM, TGA ve ICP-MS karakterizasyon yöntemleri ile incelenmiştir. Asitle modifikasyon sırasında değiştirilen parametreler; kullanılan asit çeşidi (HCl ve H_2SO_4), kullanılan asidin molaritesi (2M-6M), asit muamelesinin yapıldığı sıcaklık (85 ve

220 °C) ve kalsinasyon sıcaklığıdır (300 - 500 °C). Genel olarak tüm muamele edilmiş kırmızı çamur numunelerinde, demir oksitin kütlece yüzdesinin arttığı ve yüzey alanının arttığı gözlemlenmiştir. Bu muamele edilmiş numunelerin 500 °C'de katalitik performans ölçümleri göstermiştir ki, 232 m^2/g değerinde en yüksek yüzey alanına sahip numune (220 °C'de 6M HCl asidi ile muamele edilen MRM-2 isimli numune) olağanüstü yüksek bir aktivasyon enerjisine sahiptir. Bu yüksek aktivasyon enerjisi bu numunenin katalitik performansının sıcaklığa oldukça hassas olduğunu göstermektedir. Bu sebeple, bu muamele edilmiş numune daha ileri bir düzeyde incelenmiş ve 700°C'de de amonyaktan hidrojen üretme tepkimesi için performansı test edilmiştir. Sonuçlar göstermiştir ki, 700 °C 'de ve 72 000 cm^3 NH_3 h^{-1} g_{kat}^{-1} akışı altında, MRM-700R@700, stabil % 97 ± 0.5 değerinde bir dönüşüm oranı vermektedir. Bu değer, literatürdeki diğer soy olmayan metaller arasında en yüksek değerdir. MRM-700R@700 katalizöründe bu yüksek ve stabil performansı veren parçacıkların, reaksiyon öncesi katalizörü 10 saat boyunca NH_3 akışına maruz bıraktıktan sonra oluşan nitrürlenmiş demir (ε-Fe_2N) olduğu açığa çıkarılmıştır. Bu maliyeti olmayan yüksek performanslı katalizör ile detaylı fizibilite çalışması da yapılmıştır. Kırmızı çamurun amonyaktan hidrojen üretimi reaksiyonu için katalizör olarak kullanımı başlıca iki olanak sağlamaktadır. Bunlardan ilki, çok yüksek miktarlarda açığa çıkan ve tehlikeli sınıfına giren bir endüstriyel atığın kullanımını sağlamaktır. İkincisi ise, CO_x açığa çıkarmayan amonyaktan hidrojen üretimi reaksiyonu için, stabil, yüksek performansa sahip ve maliyeti olmayan bir katalizör elde etmiş olmaktır.

ACKNOWLEDGEMENTS

First I would like to thank my advisor Asst. Prof. Dr. Alper Uzun, who has guided me throughout my research with his patience and knowledge. His door was always open for any questions. One simply could not wish for a friendlier advisor entering the lab by asking a motivating question: “How is it going Rocky?"

I want to express my sincere thanks to my thesis committee members Prof. Dr. Ahmet Erhan Aksoylu and Assoc. Prof. Dr. Uğur Ünal.

My sincere thanks got to the Scientific and Technological Council of Turkey (TUBITAK) (Project number: 213M028), Science Academy BAGEP program, Graduate School of Sciences and Engineering for Academic Excellence Award and Koç University TÜPRAŞ Energy Center (KUTEM) for providing support and giving me the opportunity to work on this project and also to Seydişehir Eti Alüminyum for providing us red mud.

Special thanks to Dr. Rıza Kızılel for always providing help during my two years in KUTEM. I would like to also thank Dr. Barış Yağcı and Cansu Yıldırım for patiently teaching me to use SEM, XRD and XRF instruments, for performing numerous measurements and for always supporting me when I was in a hurry. I would like to thank Assoc. Prof. Dr. Uğur Ünal for providing help during my article revision period. I would also like to thank Asst. Prof. Sezen Soyer-Uzun for her kind assistance when I was writing my first article. Without her, red mud would not exist in this thesis at all.

I was very lucky to have been blessed with a friendly and cheerful group of students while working in KUTEM. My special thanks go to my project mate F. Eylül Saraç Öztuna, my neighbor Navid Solati, my calculator supplier Salim Şimşek, Ehsan Sarayloo and Ekin Esen. I am also grateful to my dear group members Elif Kocaman, Melike Babucci, Özge Akarçay, Özge Deniz Bozkurt, Ahsan Jalal, Burak Koyutürk, Pelin Kınık, Volkan Balcı, Çiğdem Altıntaş, Vahid Nozari, Sadi Gürses and İbrahim Şahin for their friendship, motivating attitude and for being always helpful in the lab.

I also want to thank Naz Ecem Çınaryılmaz for making life easier in my first year at Koç University.

I owe more than thanks to my beloved soul-mate and best friend Sefa Öztulum. Thank you for encouraging me throughout this experience and for being always by my side.

Finally, my very special gratitude goes to my family, who provided me unflagging love and unconditional support during my whole life. You made me live a unique childhood that has made me who I am now.

To my parents Beatrice and Ertuğrul

Table of Contents

LIST OF TABLES

LIST OF FIGURES

Chapter 1

INTRODUCTION

Undoubtedly the biggest environmental and health problems of the last century is the enormous use of fossil fuels. This excessive use results in greenhouse gas emissions causing problems, such as global warming, climate change, and air pollution. Furthermore, oil reserves will not be able to meet the energy demand, which is expected to double or triple by 2050 [1]. The decreasing availability, harmful effects to health and environment of fossil fuels and the increasing demand for energy are the reasons for the investigation on alternative fuels, which are sustainable, environmentally friendly, and easy to handle. As a result, hydrogen energy has gained importance.

Hydrogen can be considered as an excellent new generation fuel when compared to fossil fuels because it is the most abundant element in the world, the only product of hydrogen combustion is water with no CO_x, SO_x, and unburned hydrocarbon emissions [2], and it has approximately 3 times larger energy yield then hydrocarbon fuels making it more energy efficient [3]. One important disadvantage of hydrogen is that it needs four times more volume when compared to gasoline. In other words there are several obstacles to use hydrogen energy, such as the challenges in storage, production, and distribution of hydrogen [4]. In this regard, one possible compound which can be used as a storage medium for hydrogen is ammonia. Ammonia has several advantages i) it has a high hydrogen density; ii) it is non-carbon containing, thus does not produce any CO_x side products; iii) it is one of the most known and handled chemical in the world; and iv) it is easy to transport [5].

Active components for ammonia decomposition reaction include Ru, Ni, Fe, Pt, Pd, and Ir based catalysts together with some alloys, nitrides, and carbides of metals [6]. Ruthenium based catalysts are known to be the most active catalyst for this reaction [5]. However, ruthenium based catalysts suffer from very high costs. Ammonia decomposition catalyst should be cost effective with sufficiently high catalytic activity. This is why some Ni and Fe based catalysts are also proposed and research is going on for increasing the activities of these catalysts.

Red mud (RM) is a harmful by-product of the aluminum production process called Bayer process. It is highly alkaline and contains some toxic components such as heavy metals and trace amount of radioactive materials which causes RM to be classified as a toxic industrial waste [7]. Since around two tons RM is produced for each ton of alumina produced, it is produced in significantly huge amounts. Bayer process is being used over 120 years and this unwanted by-product is mainly disposed of in long-term storage on land [8, 9]. Therefore, the application of RM is of great importance.

RM is a mixture of several metal oxides such as Fe_2O_3, SiO_2, Al_2O_3, TiO_2, Na_2O, SO_3, ZrO_2, and MgO. The amount of these metal oxides varies according to the origin of RM. These components contained in RM and the fine particle size with a considerable surface area (18 m^2/g) makes RM interesting and important for chemical applications. Regarding the catalytic activity of Fe for ammonia decomposition and the 37 wt%. Fe_2O_3 amount in RM produced in Turkey, RM can be used as a catalyst for ammonia decomposition.

Within the scope of this thesis the properties of RM were tuned to convert it into an efficient catalyst for ammonia decomposition to produce hydrogen by acid dilution followed by ammonia precipitation. By changing some parameters a series of modified red mud (MRM) samples were obtained. Each of these samples was characterized deeply by a wide range of characterization techniques, such as x-ray diffraction (XRD), x-ray fluorescence (XRF), Brunauer-Emmett-Teller (BET) pore volume and surface area analysis, scanning electron microscopy coupled with energy-dispersive x-ray spectroscopy (SEM/EDX), inductively coupled plasma-mass spectrometry (ICP-MS), temperature programmed reduction (TPR), thermogravimetric analysis (TGA) and Fourier transform infrared spectroscopy (FTIR). These synthesized MRM samples were tested for their catalytic activity for ammonia decomposition. The relation between catalysts' chemical and structural properties and the catalytic activities were investigated.

Chapter 2 comprises of a literature review on ammonia decomposition, also including information on hydrogen as a fuel and ammonia as a storage medium. Besides Fe-based catalysts, Ni- and Ru- based catalysts were also reviewed and some information about the reaction mechanism was included.

Chapter 3 provides a literature review on RM characteristics, literature on its modification and applications.

Chapter 4 describes experimental methods, including sample preparation techniques, characterization methods, and catalytic testing details.

Chapter 5 is reporting modification of RM by simple treatments with systematically varying treatment parameters and detailed characterization of each emerging MRM sample. Results presented in this chapter has been submitted to *Ceramics International* for publication (entitled "Tuning the Structural Characteristics of RM by Simple Treatments") and as of August 2016, it is currently under review.

Chapter 6 provides briefly the experimental data of the catalytic testing of various RM and MRM samples characterized in Chapter 5 under ammonia decomposition conditions.

Chapter 7 presents the most important findings of this thesis study that RM can be converted into an efficient catalyst for ammonia decomposition with exceptional stable and high activity. Detailed characterization helped to identify the species responsible for this exceptional catalytic performance. An article presented these results have just been accepted for publication with a title "Red Mud as an Eco-Friendly, Efficient, Stable, and Cost-free Catalyst for CO_x-free Hydrogen Production from Ammonia" in *Scientific Reports*, a journal published by Nature Publishing Group.

Chapter 8 includes a brief feasibility study on the economics of various hydrogen production methods. Furthermore, the economic analysis for hydrogen fueling stations or on-board hydrogen production is determined for RM, Ru-based, and Ni-based catalyst.

In conclusion, this thesis is a guide in providing detailed and extensive characterization data of RM. During the modification of RM, parameters were systematically varied and the resulting samples were compared. Furthermore, it was shown that iron nitride species forming due to the nitriding of iron with ammonia are the active species for ammonia decomposition making that specific MRM catalyst an excellent alternative for this reaction. Finally, using this catalyst in high amounts either on-board or in fueling stations to produce hydrogen, adds no cost to the system making it an ideal candidate to use in hydrogen production units from ammonia.

References

[1] S. Sharma and S.K. Ghoshal, Hydrogen the future transportation fuel: From production to applications, Renewable and Sustainable Energy Reviews. 43 (2015) 1151-1158.

[2] M. İlbas, İ. Yılmaz, and Y. Kaplan, Investigations of hydrogen and hydrogen–hydrocarbon composite fuel combustion and emission characteristics in a model combustor, Int. J. Hydrogen Energy. 30 (2005) 1139-1147.

[3] I.K. Kapdan and F. Kargi, Bio-hydrogen production from waste materials, Enzyme Microb. Technol. 38 (2006) 569-582.

[4] A. Klerke, C.H. Christensen, J.K. Nørskov, and T. Vegge, Ammonia for hydrogen storage: Challenges and opportunities, J. Mater. Chem. 18 (2008) 2304-2310.

[5] F. Schüth, R. Palkovits, R. Schlögl, and D.S. Su, Ammonia as a possible element in an energy infrastructure: Catalysts for ammonia decomposition, Energy and Environmental Science. 5 (2012) 6278-6289.

[6] S.F. Yin, B.Q. Xu, X.P. Zhou, and C.T. Au, A mini-review on ammonia decomposition catalysts for on-site generation of hydrogen for fuel cell applications, Applied Catalysis A: General. 277 (2004) 1-9.

[7] N. Ye, J. Yang, S. Liang, Y. Hu, J. Hu, B. Xiao, and Q. Huang, Synthesis and strength optimization of one-part geopolymer based on red mud, Construction and Building Materials. 111 (2016) 317-325.

[8] F.F. Dias, A.A.S. Oliveira, A.P. Arcanjo, F.C.C. Moura, and J.G.A. Pacheco, Residue-based iron catalyst for the degradation of textile dye via heterogeneous photo-Fenton, Applied Catalysis B: Environmental. 186 (2016) 136-142.

[9] G. Power, M. Gräfe, and C. Klauber, Bauxite residue issues: I. Current management, disposal and storage practices, Hydrometallurgy. 108 (2011) 33-4

Chapter 2

LITERATURE REVIEW ON HYDROGEN ENERGY, AMMONIA AS A HYDROGEN CARRIER AND AMMONIA DECOMPOSITION REACTION

2.1 Hydrogen as a Fuel

One of the most important problems the world is facing in the 21st century is undoubtedly the increasing energy demand due to increasing population and higher living standards. This energy demand is supplied mainly by fossil fuels which are in limited availability causing harmful effects to the environment. To overcome the problems of global warming, which is related to the increasing green-house gas emissions, an increasing amount of research focuses on clean, renewable, and sustainable alternative fuels. By 2050; 12, 25, and 30 TW of carbon-free power is required to lower the CO_2 amount of the atmosphere to 550, 450, and 350 ppm levels [1]. To eliminate the dependency on fossil fuels, to meet the energy demand of the current population and to reach the mentioned CO_2 levels, a revolution in energy production, conversion, storage, and distribution is required [2].

Hydrogen can be considered as one of the most promising alternative energy carriers. Hydrogen is the most abundant and lightest element. It is a gas at normal pressure and temperature. This gas is odorless, tasteless, and colorless. Physical and chemical properties of hydrogen and gasoline (for comparison) are given in Table 2.1. As indicated, H_2 has a wide range of flammability, a very low ignition energy, high energy content, and high diffusivity.

Table 2.1. Physical and chemical properties of hydrogen and gasoline [3].

Property	Hydrogen	Gasoline
Molecular weight (g/mol)	2.016	110
Mass density (kg/Nm^3) at P=1atm, T=0°C	0.09	720-780 liquid)
Mass density of liquid H_2 at 20K (kg/Nm^3)	70.9	-
Boiling point (K)	20.2	310-478
Higher heating value (MJ/kg) (assumes water is produced)	142.0	47.3
Lower heating value (MJ/kg) (assumes steam is produced)	120.0	44.0
Flammability limits (vol%)	4.0-75.0	1.0-7.6
Detonability limits (vol%)	18.3-59.0	1.1-3.3
Diffusion velocity in air (m/s)	2.0	0.17
Ignition energy (mJ)		
-At stoichiometric mixture	0.02	0.2
-At lower flammability limit	10	n/a
Flame velocity in air (cm/s)	265-325	37-43
Toxicity	Non-toxic	Toxic above 50 ppm

Several advantages of hydrogen can be listed as follows:

- Stable, non-corrosive, abundant element.
- Direct use in fuel cells for electricity generation.
- Use as a fuel in combustion engines.
- No toxic emissions while energy production with water being the only product.
- High energy conversion efficiency.
- Higher lower heating value than fossil fuels per unit mass.
- Ease of conversion to other energy forms [2,4,5].

Several disadvantages of hydrogen can be listed as follows.

- Unavailability in nature in the form of H_2.
- Expensive production processes.
- Greater storage and transportation barriers.
- Currently, fossil fuel based H_2 production methods.
- Volatile, wide flammability limits, invisible flame.
- Leakage from vessels due to small size of molecules [5,6].

By regarding these points, the aim of H_2 production in the most economical way with a very low CO_2 foot-print is the basis of many researches. There are several H_2 production methods such as steam methane reforming, auto-thermal reforming of oil, gasification of coal and/or other hydrocarbons, electrolysis of water, hydrogen production from biomass, nuclear energy and biological processes [7]. Currently, non-renewable sources dominate the hydrogen production processes as from coal, oil and natural gas [8, 9]. Producing hydrogen from the other mentioned renewable sources can be a breakthrough for the future energy need. Especially in the transportation sector 92% of the energy demand is supplied by fossil fuel based fuels which causes 17% of global CO_2 emission corresponding to approximately 30.4 gigatonnes in 2010 [7].

Transportation and storage of hydrogen seems to be one of the most critical issues especially for fuel cell driven transportation [10]. Hydrogen storage requires pressurized liquid hydrogen tanks which are costly and encounter some crucial safety issues. The very low boiling point, extremely low density in gaseous phase and very high density in liquid phase as mentioned in Table 2.1 make hydrogen storage complicated. Up to 700 bar pressure is needed to store hydrogen in vehicles as liquidor and cooling down to -253 °C is required to store it as a liquid in cryogenic reservoirs. However, here a significant energy loss occurs during compression and another issue is the perception of public about safety [9]. This is why storage of hydrogen in various different ways other than only by compression in tanks gained importance.

The summary of hydrogen storage materials and their limitations are given in Table 2.2. Sorbent materials, such as nano-tubes, graphene or metal organic frameworks store hydrogen by physisorption. They suffer from high costs, require low temperatures and needs more investigations. Chemisorption of hydrogen on complex metal hydrates (such as $LiAlH_4$, $NaBH_4$, $Al(BH_4)_3$) results in high hydrogen density but poor reversibility. Much research is needed to determine the appropriate catalyst, stability of these materials and the kinetics [11]. Due to the limitation of these methods, the molecular storage of hydrogen in chemical compounds is considered. There are some carbon containing storage molecules which are hydrocarbons or alcohols such as methanol. For example CH_4 has a relatively high hydrogen content such as 25 wt.%. However it should be noted that breaking the chemical bonds of these storage molecules to obtain hydrogen causes significant amounts of CO_x formation. This is why some of non-carbon containing chemical compounds having high hydrogen density such as $Mg(NH_3)$, NH_3BH_3 and NH_3 got attention. Due to the limitations of storage in materials mentioned in Table 2.2, the molecular hydrogen storage in ammonia will be considered as a solution to storage and transportation of hydrogen. Furthermore, direct usage of ammonia in fuel cell driven cars is also another possibility. Further information on ammonia as a storage molecule will be given in the following section.

Table 2.2. Limitations of hydrogen storage materials [11].

Hydrogen Storage Materials	**Limitation**
Carbon Nanostructures	Reversible but requires low temperature
Metal Hydrides	Reversible nut too heavy and expensice
Metal Organic Frameworks	Reversible but requires low temperature
Complex Chemical Hydrides	High hydrogen density, appropriate temperature but irreversible
Metal Clusters	Computationally predicted but hard to prove results experimentally
Nanostructure Materials	Needs to be explored

2.2 Ammonia as a Fuel and/or Hydrogen Storage Medium

2.2.1 Characteristics of Ammonia as a Possible Energy Carrier

Ammonia has a high content of hydrogen by both unit volume and weight (108 kg H_2/m^3 NH_3 and 17.8 wt%, respectively). By considering the most advanced methods for hydrogen storage, such as metal hydrides which only reaches approximately 25 kg H_2/m^3, ammonia's storage capacity is four times higher [12]. More information can be found in Figure 2.2 illustrating the plot of gravimetric H_2 density (wt.%) vs. volumetric H_2 density (kg H_2/ m^3) for several hydrogen storage materials. According to Figure 2.2 liquid ammonia is clearly located at both high volumetric and high gravimetric density region.

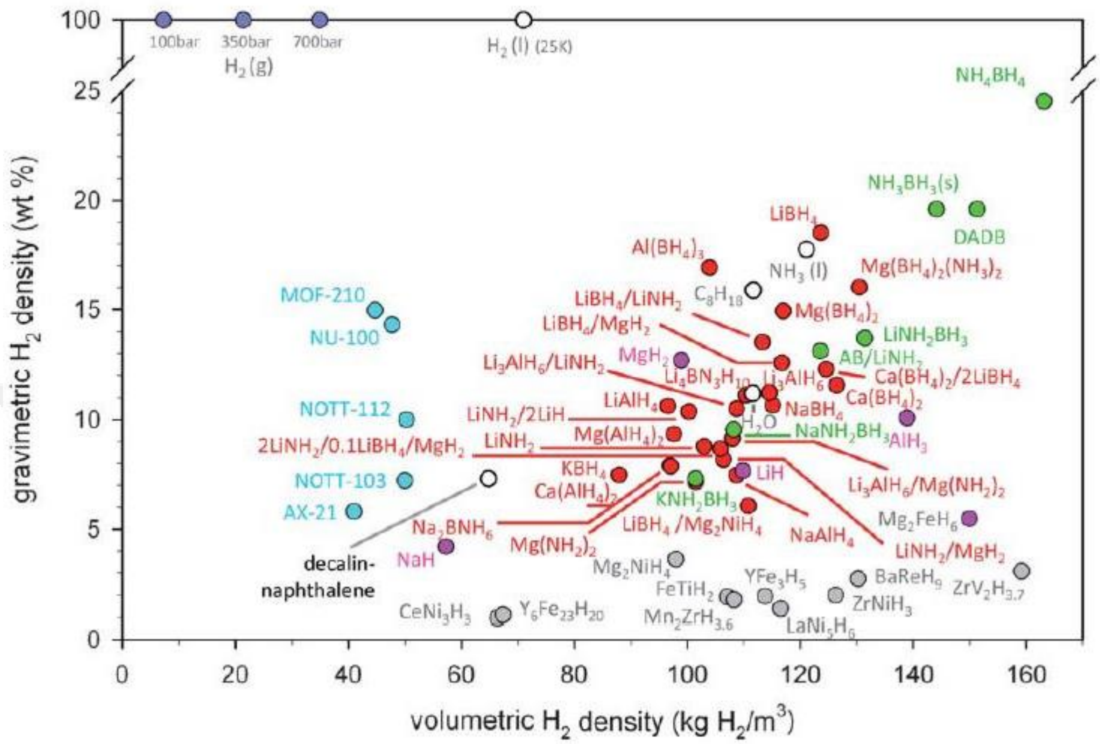

Figure 2.1. Gravimetric H_2 density (wt%) plotted against volumetric H_2 density (kg H_2/m^3) for several hydrogen storage materials [13] (Reproduced with permission of Royal Society of Chemistry).

Ammonia can be cracked into hydrogen and nitrogen thermally and catalytically for the use of hydrogen in fuel cells. Besides the application of ammonia as a hydrogen carrier due to its good hydrogen storage capacity, another advantage is the direct use in internal combustion engines [14]. It has a high octane number of 110-130. The storage and transportation systems for ammonia already exists since this chemical is one of the oldest used in the world and is produced 100 million tons yearly [15,16]. Even if toxic, ammonia can be considered safer than many other mentioned hydrogen storage options. It is lighter than air, so it can rapidly escape into the atmosphere. Any leakage as low as 5 ppm can be detected even by nose. It can be considered as non-flammable and has no explosion danger.

Ammonia is produced by the Haber Bosch process, which is one of the largest and best studied chemical processes in the world [17]. Hydrogen for the synthesis process of ammonia is nowadays mostly produced by steam reforming of natural gas. 50% of produced hydrogen is then used to produce ammonia which is most likely used for agricultural purposes. This arises the environmental problems and CO_2 remains a big challenge. This is why biomass or nuclear hydrogen and electrolysis methods should be considered as alternatives [18].

Ammonia decomposition reaction is one of the key important aspects for hydrogen energy by ammonia. Even though, this reaction was previously investigated to understand the ammonia synthesis, nowadays it is investigated due its increasing acceptance to be used as an energy carrier. Also according to Department of Energy of the United States, DOE [19], one of the research priorities for the potential role of ammonia for the usage in hydrogen production is the design of a highly efficient ammonia cracking catalysts. Ruthenium catalysts are known to be the most active ones for this reaction; however, the high cost and limited availability of ruthenium are important drawbacks for this catalyst.

2.2.2 Ammonia Decomposition Catalysts

Ammonia synthesis is one of the oldest studied reactions due to its high industrial relevance and since it is a key reaction for the understanding of catalysis in general which makes this reaction scientifically and culturally important [17]. That is why ammonia synthesis reaction is a heterogeneous reaction with most complete understanding. Ammonia decomposition catalysts on the other hand, were firstly investigated to understand the ammonia synthesis catalysts which makes it also one of the first catalytic reactions studied [20]. However, Boisen *et al*. came to a conclusion that the conditions for ammonia synthesis and decomposition are quite different which suggests that optimal synthesis catalyst is not an optimal decomposition catalyst [21,22].

Active components for NH_3 decomposition were ranked by Ganley *et al.* as Ru > Ni > Rh > Co > Ir > Fe >> Pt > Cr > Pd > Cu >> Te, Se, Pb [23]. Beside the catalysts prepared by these mentioned active components, the alloys of them [24], nitrides, [25] and carbides [26] of some of these metals were also found to be active. As also mentioned in the ranking of Ganley *et al.*, Ru is the most active metal. Ru-based catalysts are the most studied ones in the last decade even though the decomposition studies were mostly focusing on Fe-based catalysts for the understanding of ammonia synthesis in the early years [27].

A very comprehensive study was conducted by Yin *et al.* in which Ru catalyst on various supports were compared [28]. At 823 K and 30 000 cm^3 NH_3 h^{-1} g_{cat}^{-1} space velocity, the Ru/CNT catalyst showed 33.4 mmol H_2 min^{-1} g_{cat}^{-1} production. In addition to this result it was shown that the catalyst with increased basicity due to the promoter K, showed the same H_2 production rate even at 743 K. By this study it came out that CNT's are the best support materials for Ru since this material restricts the growth of Ru particles. Yin *et al.* were also able to make a comparison between supports and they were ranked as Ru/CNT's > Ru/MgO > Ru/TiO_2 = Ru/Al_2O_3 = Ru/ZrO_2 > Ru/AC > Ru/ZrO_2-BD [28]. One of the most important properties of a support is that it should possess a high surface area. However, for ammonia decomposition, supports have also different kind of impact to the performance other than providing high surface area. For example, basicity, conductivity, low concentration of electron withdrawing groups and high thermal stability of the support are important parameters [27]. Similarly, Yin *et al.* claim that the basic nature and good electronic conductivity beneficial for electron transfer from support to Ru are the reasons that CNT is an excellent support [28]. Promoters consisting of generally alkali, alkali earth, and rare earth metal ions, play also an important role in the catalytic activity, as for example for the promoter K. Because of this finding further investigations were done for Ru based catalyst by searching for the effect of different promoters. The study comprises of the already best performing Ru/CNT catalysts promoted by some metal nitrates. Activities were ranked according to the promoter as K-Ru > Na-Ru > Li-Ru > Ce-Ru > Ba-Ru > La-Ru > Ca-Ru > Ru [29]. Atomic ratio of K/Ru=2 was found as most effective. In a recent study, Hill and Torrento-Murciano determined that cesium promotion can also develop the activity of Ru catalyst on graphitized CNT due to high electron conductivity [30].

The fact that Ru is a precious metal, and thus, it suffers from high cost and limited availability, Ni-, Fe-, and Co- based catalysts are considered as non-noble alternatives. In one of the first attempts investigating the Ni-based catalysts Choudhary *et al.* showed that Ni-based catalysts have comparable activity for ammonia decomposition [31]. When comparing

Ni with Ir and Ru, it was concluded that Ni is attractive due to its low cost and does not have a significantly different activity then Ru even if it costs much less than Ru. However, they observed also deactivation of Ni nanoparticles due to sintering into larger ones at higher temperatures than 400 °C. For Ni based catalysts CNT's may not be the ideal support [20]. Muroyama *et al.* showed that Ni/SiO_2 and Ni/Al_2O_3 showed high activity due to the supports high surface area (200 m^2/g for Al_2O_3 and 280 m^2/g for SiO_2) [32]. Even though La_2O_3 (surface area of 4.7m^2/g) having a much less surface area showed comparable activity due to $LaNiO_3$ formations.

Improvements for both dispersion and thermal stability are important facts for Ni catalysts for ammonia decomposition. In order to overcome the sintering problems of Ni at high temperatures, Inokawa *et al.* showed that when synthesizing Ni nanoparticles from $Ni(C_5H_5)$ in the pores of zeolites, the stability of nanoparticles smaller than 5 nm could be maintained for more than 100 h [33]. Zhang *et al.* suggested the encapsulation of Ce modified Ni nanoparticles in SiO_2 to overcome stability problems. In this study at 923 K H_2 production was 33.24 mmol H_2 min^{-1} g_{cat}^{-1} for Ce-Ni@SiO_2 catalyst at a space velocity of at 99.3 % conversion [34].

Other non-noble metal catalysts like iron-based ones are also good alternatives to Ru-based catalysts. However, different than Ni-based catalysts, they require even higher temperatures for ammonia decomposition activity due to the slow recombinative desorption of absorbed nitrogen atoms which cannot take place at temperatures lower than 550 °C [35]. However, since direct ammonia fuel cells are operated at temperatures between 500 to 700 °C, low temperature requirement is not so crucial once a highly active iron catalyst can be synthesized [36]. That is why even though Fe-based catalysts show lower activity than Ni-based catalysts at lower temperatures, they are still extensively investigated due to their low cost and wide availability [37]. An important issue that should be considered for the iron catalysts is that during ammonia decomposition, in parallel to this, nitriding reaction of iron occurs [25,38]. Producing iron nitride from iron by the exposure to ammonia is a known concept and can be done at varying temperatures resulting in various iron nitride species [39]. This changes the characteristics of the catalyst, and thus, also the reaction kinetics. There are even efforts to produce iron nitride species other than the ammonia method [40] since it is known that iron nitride (in this case Fe_3N) is active for ammonia decomposition [41]. Thermal stability and dispersion are also of great importance as for other catalysts. Furthermore, several iron catalysts have a remarkably long activation period which is generally due to new formations such as Fe_xN species [41,42]. To overcome thermal stability problems SiO_2 encapsulation was performed by Li *et al*. and it was observed that the core shell structured iron nanoparticles are superior to naked Fe or silica supported Ni catalysts due to their stability [43]. Another core shell structured catalyst was introduced by Feyen *et al.* [36], having iron and iron nitride cores with long term stability. The 35 and 75 nm diameter particle sizes seemed to have less influence on activity. Li *et al.* observed also a better stability after testing the core-shell catalyst Fe@SiO_2 modified by Cs [44]. Ceria or titania was used as a shell coating of iron spheres by Cui *et al.* in order to increase stability and surface area [45].

Similarly to Ni- and Ru-based catalysts, Fe catalysts on CNT (carbon nanotube) and CNF (carbon nanofiber) supports were investigated for ammonia decomposition. Duan *et al*. synthesized Fe nanoparticles on CNFs and mica surface, which enabled the control of Fe particle size and shape [42]. Mica isolated Fe particles enabled a high and stable performance. Another study using CNFs as supports was conducted by Ji *et al.* revealing that increasing growth time of CNFs resulted in a higher activity [46]. The highest catalytic activity reported by a Fe-based catalyst was recorded by Lu *et al.* by the Fe on carbon nanotubes catalyst [47]. At 600 °C and at a space velocity of 60 000 cm^3 NH_3 h^{-1} g_{cat}^{-1} h the catalyst was able to maintain 78% conversion. Furthermore, the catalyst deactivates quickly at 700 °C at a space velocity of 120 000 cm^3 NH_3 h^{-1} g_{cat}^{-1} showing an initial activity of more than 90%. However it decreases constantly to 50% within 16 hours. Even if these are the highest recorded values, the unstable performance and the complicated procedure in synthesizing this catalyst remain as an obstacle for having a cheap and active catalyst for ammonia decomposition.

As mentioned above, Ru shows significantly high H_2 production rates from ammonia decomposition; however, it suffers deeply from low availability and high cost. On the other hand, Ni and Fe catalysts are clearly much more cost effective. Ni catalysts are more promising than Fe based catalysts at low temperatures. However by considering the direct ammonia fuel cell's working principles for the onsite generation of H_2, the necessary temperatures of 500 to 700 °C do not give rise to a big challenge. Nevertheless, these high working temperatures of iron based catalysts cause certain stability problems and therefore most of the studies focus on cautions for the stability of the catalyst like encapsulation (core-shell catalysts). Even if Fe on carbon nanotube catalyst has an outstanding performance, it extremely suffers from instability. So, there is still a need for a cheap catalyst with high and stable performance. Moreover, the synthesis procedure should be easy and environmentally friendly. The main objective of this thesis is to find an appropriate catalyst having the mentioned characteristics.

2.2.3 Ammonia Decomposition Mechanism

NH_3 (gas) → 0.5 N_2 (gas) + 1.5 H_2 (gas) $\Delta H = +46$ kJ/mol

Ammonia decomposition is a gas phase endothermic reaction. Due to thermodynamic limitations, this reaction requires elevated temperatures. A wide variety of mechanisms are proposed for this reaction and the most accepted thought about the rate determining step is that the recombinative desorption of N_2. However, for different metals, support materials and NH_3 concentration conditions different findings were published. It should be noted that the kinetic analysis was mostly done for Ru- and Ni- based catalysts. The most widely accepted steps of the mechanism are as given below:

2NH_3 (gas) → 2NH_3 (ads)

2NH_3 (ads) → 2NH_2 (ads) + 2H (ads)

2NH_2 (ads) + 2H (ads) → 2NH (ads) + 4H (ads)

2NH (ads) + 4H (ads) → 2N (ads) + 6H (ads)

2N (ads) + 6H (ads) → N_2 (ads) + 3 H_2 (ads)

N_2 (ads) + 3 H_2 (ads) → N_2 (gas) + 3H_2 (gas)

According to Egawa *et al*. a nearly first order (0.75) dependence on NH_3 and a dependence of H_2 of negative second order were determined for Ru single crystal surfaces [48]. Consequently, they confirm that H_2 has an inhibitory effect because of the equilibrium established between gas phase NH_3 and adsorbed N atoms. They also determined the rate controlling step as associative desorption of N atoms (2N (ads) → N_2 (gas)). Tsai and Weinberg determined the rate determining step for two conditions for Ru surface [49]. At low temperature the rate is controlled by the desorption of nitrogen with no dependency on ammonia pressure. At high temperatures they found that rate is controlled by a competition between desorption of ammonia and the dissociation of N-H bond occurring at the surface. McCabe observed that for nickel at temperatures below 727 °C rate is independent of NH_3 pressure whereas above 727 °C first order kinetics occurs [50]. The rate determining step for temperatures below 727 °C was found as dissociation of strongly adsorbed nitrogen; however, in the first order dependent region rate is controlled by adsorption of NH_3. Bradford *et al.*, investigating the Ru/C catalyst found similarly to Egawa *et al.* the inhibitory effect of H_2 [51]. They found a first order dependence with NH_3 and negative 3/2 to negative second order dependence on H_2. Furthermore, they presented a kinetic model that proposes two rate determining steps which are NH_2-H bond cleavage step and recombinative nitrogen desorption. Chellappa *et al.* used pure ammonia for kinetic studies for Ni-Pt/Al_2O_3 catalyst for similarity to real conditions especially when ammonia decomposition is applied for fuel cell applications [52]. At high temperature and high ammonia concentrations a first order rate with respect to ammonia was observed. So, the transition from zero order to first order was not observed as it was previously reported. Stolbov and Rahman conducted a comparative study of Pd and Ni catalysts by investigating NH_3 decomposition on various surfaces [53]. For Ni they found that besides the desorption of nitrogen the first step of ammonia decomposition (NH_3 to NH_2 and H) is also of great importance when considered as rate limiting step.

Based on these findings, in a recent study Takahashi and Fujitani created their model including several assumptions and using the kinetically most important steps [54]. They claimed that in most of the studies no simultaneous kinetic analysis was conducted for Ni and Ru catalysts. They neglected the multistep NH_3 dehydrogenation and due to the inhibitory effect of H_2 equilibrium was considered between the adsorbed H atoms and the gas phase H_2. Their mechanism simplified as illustrated below:

NH_3 (gas) + s $\leftrightarrow$ NH_3 (ads)

NH_3 + 3s $\rightarrow$ N (ads) + 3H (ads)

2N (ads) $\rightarrow$ N_2 (g) +2s

2H (ads) $\leftrightarrow$ H_2 (g) +2s

While N_2 desorption was found to be rate determining for Ru catalyst, NH_3 dehydrogenation step was rate determining for Ni catalyst.

On the whole, it is not easy to determine a general mechanism. Different kinds of studies suggest distinct pathways or rate limiting steps. The mechanism of ammonia decomposition reaction should be still investigated deeply.

References

[1] M.I. Hoffert, K. Caldeira, G. Benford, D.R. Criswell, C. Green, H. Herzog, A.K. Jain, H.S. Kheshgi, K.S. Lackner, J.S. Lewis, H.D. Lightfoot, W. Manheimer, J.C. Mankins, M.E. Mauel, L.J. Perkins, M.E. Schlesinger, T. Volk, and T.M.L. Wigley, Engineering: Advanced technology paths to global climate stability: Energy for a greenhouse planet, Science. 298 (2002) 981-987.

[2] S.E. Hosseini and M.A. Wahid, Hydrogen production from renewable and sustainable energy resources: Promising green energy carrier for clean development, Renewable and Sustainable Energy Reviews. 57 (2016) 850-866.

[3] M. Balat, Potential importance of hydrogen as a future solution to environmental and transportation problems, Int. J. Hydrogen Energy. 33 (2008) 4013-4029.

[4] I. Dincer and C. Acar, Review and evaluation of hydrogen production methods for better sustainability, Int. J. Hydrogen Energy. 40 (2015) 11094-11111.

[5] F.H. Sobrino, C.R. Monroy, and J.L.H. Pérez, Critical analysis on hydrogen as an alternative to fossil fuels and biofuels for vehicles in Europe, Renewable and Sustainable Energy Reviews. 14 (2010) 772-780.

[6] T. Abbasi and S.A. Abbasi, 'Renewable' hydrogen: Prospects and challenges, Renewable and Sustainable Energy Reviews. 15 (2011) 3034-3040.

[7] S. Singh, S. Jain, V. Ps, A.K. Tiwari, M.R. Nouni, J.K. Pandey, and S. Goel, Hydrogen: A sustainable fuel for future of the transport sector, Renewable and Sustainable Energy Reviews. 51 (2015) 623-633.

[8] M. Serban, M.A. Lewis, C.L. Marshall, and R.D. Doctor, Hydrogen production by direct contact pyrolysis of natural gas, Energy Fuels. 17 (2003) 705-713.

[9] S. Sharma and S.K. Ghoshal, Hydrogen the future transportation fuel: From production to applications, Renewable and Sustainable Energy Reviews. 43 (2015) 1151-1158.

[10] D. Mori and K. Hirose, Recent challenges of hydrogen storage technologies for fuel cell vehicles, Int. J. Hydrogen Energy. 34 (2009) 4569-4574.

[11] P. Jena, Materials for hydrogen storage: Past, present, and future, Journal of Physical Chemistry Letters. 2 (2011) 206-211.

[12] L. Schlapbach and A. Züttel, Hydrogen-storage materials for mobile applications, Nature. 414 (2001) 353-358.

[13] W.I.F. David, Effective hydrogen storage: A strategic chemistry challenge, Faraday Discuss. 151 (2011) 399-414.

[14] H. Nozari and A. Karabeyoğlu. *Combustion characteristics of ammonia as a renewable energy source and development of reduced chemical mechanisms*. in *13th International Energy Conversion Engineering Conference*. 2015.

[15] C.H. Christensen, T. Johannessen, R.Z. Sørensen, and J.K. Nørskov, Towards an ammonia-mediated hydrogen economy?, Catal. Today. 111 (2006) 140-144.

[16] C. Zamfirescu and I. Dincer, Ammonia as a green fuel and hydrogen source for vehicular applications, Fuel Process. Technol. 90 (2009) 729-737.

[17] R. Schlögl, Catalytic synthesis of ammonia - A "never-ending story"?, Angewandte Chemie - International Edition. 42 (2003) 2004-2008.

[18] R. Lan, J.T.S. Irvine, and S. Tao, Ammonia and related chemicals as potential indirect hydrogen storage materials, Int. J. Hydrogen Energy. 37 (2012) 1482-1494.

[19] G. Thomas, and G. Parks, Potential Roles of Ammonia in a Hydrogen Economy. Retrieved from https://www.hydrogen.energy.gov/pdfs/nh3_paper.pdf

[20] F. Schüth, R. Palkovits, R. Schlögl, and D.S. Su, Ammonia as a possible element in an energy infrastructure: Catalysts for ammonia decomposition, Energy and Environmental Science. 5 (2012) 6278-6289.

[21] A. Boisen, S. Dahl, J.K. Nørskov, and C.H. Christensen, Why the optimal ammonia synthesis catalyst is not the optimal ammonia decomposition catalyst, J. Catal. 230 (2005) 309-312.

[22] A. Boisen, J.K. Nørskov, S. Dahl, and C.H. Christensen. *Finding the optimal ammonia decomposition catalysts*. in *ACS National Meeting Book of Abstracts*. 2005.

[23] J.C. Ganley, F.S. Thomas, E.G. Seebauer, and R.I. Masel, A priori catalytic activity correlations: The difficult case of hydrogen production from ammonia, Catal. Lett. 96 (2004) 117-122.

[24] Z. Lendzion-Bieluń and W. Arabczyk, Fused FeCo catalysts for hydrogen production by means of the ammonia decomposition reaction, Catal. Today. 212 (2013) 215-219.

[25] W. Arabczyk and R. Pelka, Studies of the kinetics of two parallel reactions: Ammonia decomposition and nitriding of iron catalyst, J. Phys. Chem. A. 113 (2009) 411-416.

[26] S.S. Pansare and J.G. Goodwin Jr, Ammonia decomposition on tungsten-based catalysts in the absence and presence of syngas, Ind. Eng. Chem. Res. 47 (2008) 4063-4070.

[27] S.F. Yin, B.Q. Xu, X.P. Zhou, and C.T. Au, A mini-review on ammonia decomposition catalysts for on-site generation of hydrogen for fuel cell applications, Applied Catalysis A: General. 277 (2004) 1-9.

[28] S.-F. Yin, Q.-H. Zhang, B.-Q. Xu, W.-X. Zhu, C.-F. Ng, and C.-T. Au, Investigation on the catalysis of COx-free hydrogen generation from ammonia, J. Catal. 224 (2004) 384-396.

[29] S.J. Wang, S.F. Yin, L. Li, B.Q. Xu, C.F. Ng, and C.T. Au, Investigation on modification of Ru/CNTs catalyst for the generation of COx-free hydrogen from ammonia, Applied Catalysis B: Environmental. 52 (2004) 287-299.

[30] A.K. Hill and L. Torrente-Murciano, Low temperature H2 production from ammonia using ruthenium-based catalysts: Synergetic effect of promoter and support, Applied Catalysis B: Environmental. 172–173 (2015) 129-135.

[31] T.V. Choudhary, C. Sivadinarayana, and D.W. Goodman, Catalytic ammonia decomposition: COx-free hydrogen production for fuel cell applications, Catal. Lett. 72 (2001) 197-201.

[32] H. Muroyama, C. Saburi, T. Matsui, and K. Eguchi, Ammonia decomposition over Ni/La 2O 3 catalyst for on-site generation of hydrogen, Applied Catalysis A: General. 443-444 (2012) 119-124.

[33] H. Inokawa, T. Ichikawa, and H. Miyaoka, Catalysis of nickel nanoparticles with high thermal stability for ammonia decomposition, Applied Catalysis A: General. 491 (2015) 184-188.

[34] L.-F. Zhang, M. Li, T.-Z. Ren, X. Liu, and Z.-Y. Yuan, Ce-modified Ni nanoparticles encapsulated in SiO_2 for CO_x-free hydrogen production via ammonia decomposition, Int. J. Hydrogen Energy. 40 (2015) 2648-2656.

[35] L. Wang, Y. Zhao, C. Liu, W. Gong, and H. Guo, Plasma driven ammonia decomposition on a Fe-catalyst: Eliminating surface nitrogen poisoning, Chem. Commun. 49 (2013) 3787-3789.

[36] M. Feyen, C. Weidenthaler, R. Güttel, K. Schlichte, U. Holle, A.H. Lu, and F. Schüth, High-temperature stable, iron-based core-shell catalysts for ammonia decomposition, Chemistry - A European Journal. 17 (2011) 598-605.

[37] H.Z. Cui, Y.Q. Gu, X.X. He, S. Wei, Z. Jin, C.J. Jia, and Q.S. Song, Iron-based composite nanostructure catalysts used to produce CO_x-free hydrogen from ammonia, Science Bulletin. 61 (2016) 220-226.

[38] R. Pelka, I. Moszyńska, and W. Arabczyk, Catalytic ammonia decomposition over Fe/Fe_4N, Catal. Lett. 128 (2009) 72-76.

[39] K. Rohith Vinod, P. Saravanan, M. Sakar, V.T.P. Vinod, M. Cernik, and S. Balakumar, Large scale synthesis and formation mechanism of highly magnetic and stable iron nitride (ε-Fe_3N) nanoparticles, RSC Advances. 5 (2015) 56045-56048.

[40] Z. Schnepp, M. Thomas, S. Glatzel, K. Schlichte, R. Palkovits, and C. Giordano, One pot route to sponge-like Fe_3N nanostructures, J. Mater. Chem. 21 (2011) 17760-17764.

[41] J. Zhang, M. Comotti, F. Schüth, R. Schlögl, and D.S. Su, Commercial Fe- or Co-containing carbon nanotubes as catalysts for NH_3 decomposition, Chem. Commun. (2007) 1916-1918.

[42] X. Duan, G. Qian, X. Zhou, Z. Sui, D. Chen, and W. Yuan, Tuning the size and shape of Fe nanoparticles on carbon nanofibers for catalytic ammonia decomposition, Applied Catalysis B: Environmental. 101 (2011) 189-196.

[43] Y. Li, S. Liu, L. Yao, W. Ji, and C.T. Au, Core-shell structured iron nanoparticles for the generation of CO_x-free hydrogen via ammonia decomposition, Catal. Commun. 11 (2010) 368-372.

[44] Y. Li, L. Yao, S. Liu, J. Zhao, W. Ji, and C.T. Au, Cs-modified iron nanoparticles encapsulated in microporous and mesoporous SiO_2 for CO_x-free H_2 production via ammonia decomposition, Catal. Today. 160 (2011) 79-86.

[45] H.Z. Cui, Y.Q. Gu, X.X. He, S. Wei, Z. Jin, C.J. Jia, and Q.S. Song, Iron-based composite nanostructure catalysts used to produce CO_x-free hydrogen from ammonia, Science Bulletin (2016) 1-7.

[46] J. Ji, X. Duan, G. Qian, P. Li, X. Zhou, D. Chen, and W. Yuan, Fe particles on the tops of carbon nanofibers immobilized on structured carbon microfibers for ammonia decomposition, Catal. Today. 216 (2013) 254-260.

[47] A.H. Lu, J.J. Nitz, M. Comotti, C. Weidenthaler, K. Schlichte, C.W. Lehmann, O. Terasaki, and F. Schüth, Spatially and size selective synthesis of Fe-based nanoparticles on ordered mesoporous supports as highly active and stable catalysts for ammonia decomposition, J. Am. Chem. Soc. 132 (2010) 14152-14162.

[48] C. Egawa, T. Nishida, S. Naito, and K. Tamaru, Ammonia decomposition on (1 1 10) and (0 0 1) surfaces of ruthenium, Journal of the Chemical Society, Faraday Transactions 1: Physical Chemistry in Condensed Phases. 80 (1984) 1595-1604.

[49] W. Tsai and W.H. Weinberg, Steady-state decomposition of ammonia on the Ru(001) surface, J. Phys. Chem. 91 (1987) 5302-5307.

[50] R.W. McCabe, Kinetics of ammonia decomposition on nickel, J. Catal. 79 (1983) 445-450.

[51] M.C.J. Bradford, P.E. Fanning, and M.A. Vannice, Kinetics of NH_3 decomposition over well dispersed Ru, J. Catal. 172 (1997) 479-484.

[52] A.S. Chellappa, C.M. Fischer, and W.J. Thomson, Ammonia decomposition kinetics over Ni-Pt/Al_2O_3 for PEM fuel cell applications, Applied Catalysis A: General. 227 (2002) 231-240.

[53] S. Stolbov and T.S. Rahman, First-principles study of some factors controlling the rate of ammonia decomposition on Ni and Pd surfaces, J. Chem. Phys. 123 (2005).

[54] A. Takahashi and T. Fujitani, Kinetic analysis of decomposition of ammonia over Nickel and Ruthenium catalysts, J. Chem. Eng. Jpn. 49 (2016) 22-28.

Chapter 3

LITERATURE REVIEW ON RED MUD CHARACTERISTICS, MODIFICATION METHODS AND UTILIZATION

3.1 Characteristics of Red Mud

The utilization of waste produced in vast amounts is important due to economic and environmental reasons. Wastes produced in high volume faces generally disposal problems, contain still some useful components and generally harm the environment [1]. One of the approaches for the reutilization of industrial wastes is the application in catalysis. Some frequently encountered high volume industrial wastes which can be utilized for catalytic purposes are red mud (RM), aluminum dross, fly ash, and slag from iron manufacture, chicken egg shells and rice husk ash [2]. In this thesis among these wastes RM was investigated deeply and its utilization in catalysis was the main approach.

RM is the by-product of the aluminum production process called Bayer process. Bauxite which is a natural source of aluminum hydroxide (mostly gibbsite) is processed into aluminum oxide. The mineral groups contained in the complex mixture RM can be divided into two groups: Unchanged mineral phases coming from the origin of bauxite ore (iron, titanium, unreacted alumina phases) and phases formed following the digestion stage where caustic soda is added to bauxite [3]. The main compounds in RM are, Fe_2O_3, Al_2O_3, SiO_2, TiO_2, Na_2O, CaO, MgO, and minor constituents which are the oxides of K, Cr, V, Ni, Ba, Pb, Cu, Mn, Zn, Ga, Ra Th, U [4]. The composition of RM changes according to the bauxite ore used and the process parameters [5]. In other words it is a fact that each aluminum production plant location has its specific composition for RM produced. The brick red color which is characteristic for RM is because of the high iron oxide content. Some of the most common mineral phases encountered in RM detected by XRD are hematite (Fe_2O_3), goethite (FeOOH), iron hydroxide ($Fe(OH)_3$), magnetite (Fe_3O_4), rutile (TiO_2), anatase (TiO_2), bayerite ($Al(OH)_3$), halloysite ($Al_2Si_2O_5(OH)_4$), boehmite (AlO(OH)), diaspore (AlO(OH)), gibbsite ($Al(OH)_3$), kaolinite ($Al_2Si_2O_5(OH)_4$), quartz (SiO_2), calcite ($CaCO_3$), perovskite ($CaTiO_3$), sodalite ($K_{1.4}Na_{5.3}Ca_{1.2}Al_6(SiO_4)_6(CO_3)_{0.3}(SO_4)_{0.8}Cl_{0.9}$) and cancrinite ($Na_6(Al_6Si_6O_{24}))(CaCO_3)_2$) [5]. Furthermore, RM has a relatively high surface area (13-16 m^2/g) and a fine particle size distribution (<10 micrometer) [6].

RM is produced 120 million tons globally and the global inventory has reached 3.5 billion tones in 2014 [7]. RM is considered as a hazardous industrial waste since it is highly alkaline with a pH ranging from 10 to 12.5 [8]. This high alkalinity also causes problems of the disposal or storage of this by-product produced in such high amounts. Mostly, RM is pumped to holding ponds which takes up a lot of land which has high maintenance cost, causes risks for living organisms, can cause leakage of alkaline material to groundwater, can cause overflow during storms and may cause fugitive dust [9]. An example of this area near to the Seydişehir Aluminum Factory in Turkey can be seen in Figure 3.1 taken from GoogleEarth. It is possible to see how near this storage area is to residential areas. Dewatering, soda recovery, neutralization, and ecological restoration are environmentally safe options for treating and disposing RM [10]. However, for reduced management costs another environmentally friendly option is the reutilization of RM.

Figure 3.1. RM storage area near the Seydişehir Aluminum Factory (Image was taken from GoogleEarth).

Above mentioned characteristics of RM, such as high iron content, high surface area, sintering, and poisoning resistance, low cost makes it an ideal candidate for the utilization in catalysis which will be one of the main scopes of this thesis [5]. Some of other proposed application areas for reutilization are, ceramics [11], building materials [12], adsorbents [13], and coagulants [14]. More detailed information of the potential applications of RM is illustrated in Figure 3.2 where the patent distribution between 1964 and 2008 is shown. Generally, before the utilization of RM in these mentioned areas several treatment methods (modifications) are applied to RM to enhance its physical and chemical properties. In the following section a summary of these modification methods will be given.

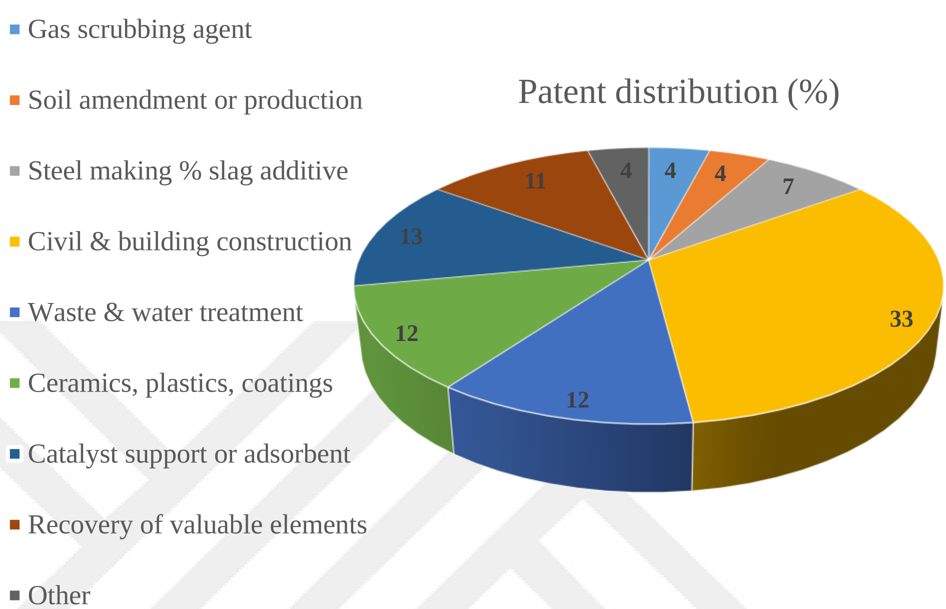

Figure 3.2. Current potential application areas of RM and corresponding patent distribution [4].

3.2 Modification Methods of Red Mud with Corresponding Application Areas

In the literature there are several modification methods proposed for RM to enhance its properties. Treatments are proposed according to the needs for the specific application area. The first modification method of RM was proposed by Pratt and Christoverson in which RM is boiled in 6 M HCl-distilled water mixture, then reprecipitated with ammonia solution until the pH of the slurry becomes 8 and the resulting sample is finally calcined in air [15]. Most of the present modification methods in the literature are based on this modification which was proposed for the hydrogenation of naphthalene.

Cengeloglu *et al.* washed RM with distilled water until the water- RM slurry reached a pH of 8 and synthesized magnetic Fe_3O_4 nanoparticles to remove V from underground water

[16]. For the removal of Pb (II) from aqueous solution Sahu *et al.* applied the same modification method of Pratt and Christoverson which resulted in a higher adsorption capacity for lead [17]. Liang *et al*. used the acids HCl, HNO_3, and H_2SO_4 without applying the reprecipitation method with ammonia which resulted in an improved adsorption property of RM for fluoride [18].

Kim *et al.* utilized RM as a catalyst by the same modification method of Pratt and Christoverson; however, they investigated the effect of changing calcination temperatures (400, 500, 600 °C) for the complete oxidation of volatile organic compounds where Pt was dispersed on modified RM [19]. A decrease in calcination temperature caused a decrease in surface area, and thus, a decrease in catalytic activity for oxidation of volatile organic compounds. Costa *et al.* investigated the effect of different reduction temperatures on RM where high reduction temperatures achieved higher activities for heterogeneous Fenton reaction and the reduction of Cr [20]. In the mentioned study RM was directly utilized by making use of the iron contained in it obtained by reduction. Oliviera *et al.* used CVD (chemical vapor deposition) reaction for the modification of RM for the utilization as a support for gold nanoparticles for biphasic oxidation of sulfur compounds [21]. Alvarez *et al.* used the same method as Pratt and Christoverson but they employed the same method also with the acid H_3PO_4 besides HCl which exhibits superior activity to HCl treated RM for the hydrogenation of antracene oil [22].

Besides these mentioned catalytic applications, there are a few articles published on RM utilized for hydrogen production by ammonia decomposition. Cao *et al*. applied the same method of Prat and Christoverson but without calcination at the end and they used the modified RM as a support material for Ni nanoparticles, which gave catalytic activity for ammonia decomposition [23,24]. Pei *et al.* modified the RM by HNO_3 and HCl treatment for 24 h but at room temperature. The resulting materials were used as supports for Ru but these catalysts exhibited lower catalytic activity compared to the most active Ru/CNT catalysts [25].

In addition to the published studies in the literature mentioned up to now where RM was modified for a single aim, there are also some characterization studies without any application but focusing on as is RM characterization. Magnetic properties of RM upon thermal treatment were investigated by Krimpalis *et al.* [26]. Thermal properties of RM with the addition of soda at varying wt% were examined by Alp and Goral [27]. Antunes *et al.* studied the thermal behavior and physical properties of RM from a Brazilian alumina plant [28]. Spanish RM characterization was published by Corpas *et al.* [29]. RM from Ireland was characterized by Atasoy [3]. Nath *et al.* performed RM characterization under high temperature of fluidization condition where fluidization temperatures were changed between 150 and 500 °C [30]. Wiu and Lu investigated the mineral phases and physical properties of Chinese RM from Guizhou by also investigating varying calcination temperatures between 100 to 1400°C [31]. The mentioned studies generally focus on characterization of single RM sample or each study only focuses on changing only one modification parameter, such as calcination temperature. Similarly, studies characterizing RM for a certain application, such as catalysis or adsorption focus also on limited parameters changed.

References

[1] J.A. Bennett, K. Wilson, and A.F. Lee, Catalytic applications of waste derived materials, Journal of Materials Chemistry A. 4 (2016) 3617-3637.

[2] M. Balakrishnan, V.S. Batra, J.S.J. Hargreaves, and I.D. Pulford, Waste materials - Catalytic opportunities: An overview of the application of large scale waste materials as resources for catalytic applications, Green Chemistry. 13 (2011) 16-24.

[3] A. Atasoy, An investigation on characterization and thermal analysis of the Aughinish red mud, J. Therm. Anal. Calorim. 81 (2005) 357-361.

[4] Z. Liu and H. Li, Metallurgical process for valuable elements recovery from red mud - A review, Hydrometallurgy. 155 (2015) 29-43.

[5] S. Sushil and V.S. Batra, Catalytic applications of red mud, an aluminium industry waste: A review, Applied Catalysis B: Environmental. 81 (2008) 64-77.

[6] R.K. Paramguru, P.C. Rath, and V.N. Misra, Trends in red mud utilization - A review, Miner. Process. Extr. Metall. Rev. 26 (2005) 1-29.

[7] S. Xue, F. Zhu, X. Kong, C. Wu, L. Huang, N. Huang, and W. Hartley, A review of the characterization and revegetation of bauxite residues (Red mud), Environmental Science and Pollution Research (2015).

[8] X. Liu and N. Zhang, Utilization of red mud in cement production: A review, Waste Manage. Res. 29 (2011) 1053-1063.

[9] H.I. Gomes, W.M. Mayes, M. Rogerson, D.I. Stewart, and I.T. Burked, Alkaline residues and the environment: A review of impacts, management practices and opportunities, Journal of Cleaner Production. 112 (2016) 3571-3582.

[10] W. Liu, X. Chen, W. Li, Y. Yu, and K. Yan, Environmental assessment, management and utilization of red mud in China, Journal of Cleaner Production. 84 (2014) 606-610.

[11] V.M. Sglavo, R. Campostrini, S. Maurina, G. Carturan, M. Monagheddu, G. Budroni, and G. Cocco, Bauxite 'red mud' in the ceramic industry. Part 1: Thermal behaviour, J. Eur. Ceram. Soc. 20 (2000) 235-244.

[12] K. Kaya and S. Soyer-Uzun, Evolution of structural characteristics and compressive strength in red mud-metakaolin based geopolymer systems, Ceram. Int. (2016).

[13] V.S. Yadav, M. Prasad, J. Khan, S.S. Amritphale, M. Singh, and C.B. Raju, Sequestration of carbon dioxide (CO_2) using red mud, J. Hazard. Mater. 176 (2010) 1044-1050.

[14] É. Poulin, J.F. Blais, and G. Mercier, Transformation of red mud from aluminium industry into a coagulant for wastewater treatment, Hydrometallurgy. 92 (2008) 16-25.

[15] K.C. Pratt and V. Christoverson, Hydrogenation of a model hydrogen-donor system using activated red mud catalyst, Fuel. 61 (1982) 460-462.

[16] I. Akin, G. Arslan, A. Tor, M. Ersoz, and Y. Cengeloglu, Arsenic(V) removal from underground water by magnetic nanoparticles synthesized from waste red mud, J. Hazard. Mater. 235-236 (2012) 62-68.

[17] M.K. Sahu, S. Mandal, S.S. Dash, P. Badhai, and R.K. Patel, Removal of Pb(II) from aqueous solution by acid activated red mud, Journal of Environmental Chemical Engineering. 1 (2013) 1315-1324.

[18] W. Liang, S.J. Couperthwaite, G. Kaur, C. Yan, D.W. Johnstone, and G.J. Millar, Effect of strong acids on red mud structural and fluoride adsorption properties, J. Colloid Interface Sci. 423 (2014) 158-165.

[19] S.C. Kim, S.W. Nahm, and Y.K. Park, Property and performance of red mud-based catalysts for the complete oxidation of volatile organic compounds, J. Hazard. Mater. 300 (2015) 104-113.

[20] R.C.C. Costa, F.C.C. Moura, P.E.F. Oliveira, F. Magalhães, J.D. Ardisson, and R.M. Lago, Controlled reduction of red mud waste to produce active systems for environmental applications: Heterogeneous Fenton reaction and reduction of Cr(VI), Chemosphere. 78 (2010) 1116-1120.

[21] A.A.S. Oliveira, D.A.S. Costa, I.F. Teixeira, and F.C.C. Moura, Gold nanoparticles supported on modified red mud for biphasic oxidation of sulfur compounds: A synergistic effect, Applied Catalysis B: Environmental. 162 (2015) 475-482.

[22] J. Álvarez, S. Ordóñez, R. Rosal, H. Sastre, and F.V. Díez, A new method for enhancing the performance of red mud as a hydrogenation catalyst, Applied Catalysis A: General. 180 (1999) 399-409.

[23] J. Cao, Y. Wang, G. Li, K. Li, Y. Wang, and M. Ma, Mesoporous modified red mud supported CuO nanocatalysts for carbon monoxide oxidation, Current Nanoscience. 11 (2015) 413-418.

[24] J.L. Cao, Z.L. Yan, Q.F. Deng, Z.Y. Yuan, Y. Wang, G. Sun, X.D. Wang, B. Hari, and Z.Y. Zhang, Homogeneous precipitation method preparation of modified red mud supported Ni mesoporous catalysts for ammonia decomposition, Catalysis Science and Technology. 4 (2014) 361-368.

[25] F.N. Pei, L. Li, S. Wang, Z. Zhu, G. Lu, and Z. Yan, Catalytic ammonia decomposition over industrial-waste-supported Ru catalysts, Environ. Sci. Technol. 41 (2007) 3758-3762.

[26] S. Krimpalis, N. Papadopoulos, K.G. Efthimiadis, C.S. Karagianni, and E. Hristoforou, Magnetic properties in red mud after thermal treatment, Journal of Optoelectronics and Advanced Materials. 10 (2008) 1085-1088.

[27] A. Alp and M.S. Goral, The influence of soda additive on the thermal properties of red mud, J. Therm. Anal. Calorim. 73 (2003) 201-207.

[28] M.L.P. Antunes, S.J. Couperthwaite, F.T. Da Conceição, C.P.C. De Jesus, P.K. Kiyohara, A.C.V. Coelho, and R.L. Frost, Red mud from Brazil: Thermal behavior and physical properties, Ind. Eng. Chem. Res. 51 (2012) 775-779.

[29] J. Pascual, F.A. Corpas, J. López-Beceiro, M. Benítez-Guerrero, and R. Artiaga, Thermal characterization of a Spanish red mud, J. Therm. Anal. Calorim. 96 (2009) 407-412.

[30] H. Nath, P. Sahoo, and A. Sahoo, Characterization of Red Mud treated under high temperature fluidization, Powder Technol. 269 (2015) 233-239.

[31] C.S. Wu and D.Y. Liu, Mineral phase and physical properties of red mud calcined at different temperatures, Journal of Nanomaterials. 2012 (2012).

Chapter 4

MATERIALS AND METHODS

4.1 Materials

Eti Seydişehir Aluminum Factory (Konya-Turkey) kindly supplied the red mud (RM) sample studied in this thesis. HCl 37% (Merck), H_2SO_4 95-97% (SigmaAldrich) and NH_3 solution 25% (Merck) were used for the modification of RM explained in detailed in the following section. H_2 (99.9999 %, Linde) was used for reduction, He (99.999 %, Messer) was used for purging and pure ammonia (99.99 %, Linde) was used for reaction.

4.2 Sample Preparation

RM was treated with two kinds of acids (HCl and H_2SO_4) at varying concentrations (2, 4, 6M) and in varying digestion temperatures (85 and 220 °C) follows by calcination at differing temperatures (300, 400, 500 °C) to obtain modified red mud (MRM) samples. MRM-1 was prepared by a similar modification method described by Pratt and Christoverson [1]. With this method, 25 g of RM is mixed with 100 ml distilled water. After 5 minutes of stirring 150 ml of 6M HCl solution is added to the slurry. A microwave digester (Milestone Microwave Digestion System (SK-10) with temperature control, operating at 350W) was used to digest the solution at 85 °C for 2h. After RM is digested in acid solution, for precipitation aqueous ammonia is added dropwise while the digested sample remains on a magnetic stirrer. The addition of aqueous ammonia proceeds until the pH of the solution becomes 8. The resulting precipitate is separated by centrifugation at 5000 rpm. The precipitate is also washed with distilled water two times. The resulting wet sample is dried for 12 hours at 110 °C before calcination. The sample prepared according to the explained method was named as MRM-1. Using the same modification method by only changing the digestion temperature from 85 to 220 °C MRM-2 was prepared. Furthermore the samples named as MRM-3, MRM-4, MRM-5, MRM-6, and MRM-7 were obtained by digesting RM with the acids at various concentrations which are 4M HCl, 2M HCl, 6M H_2SO_4, 4M H_2SO_4 and 2M H_2SO_4, respectively. RM-C500, MRM-1-C500, MRM-2-C500, MRM-3-C500, MRM-4-C500, MRM-5-C500, MRM-6-C500, and MRM-7-C500 were obtained by calcining RM, MRM-1, MRM-2, MRM-3, MRM-4, MRM-5, MRM-6, and MRM-7 in static air for 3 h at 500 °C with a temperature ramp of 5 °C/min, respectively. The samples MRM-2-C400 and MRM-2-C300 were obtained by the calcination of MRM-2 at temperatures of MRM-2-C400 and MRM-2-C300, respectively. Each sample specification and the corresponding names are summarized in Table 4.1.

Table 4.1. Abbreviations for each sample with corresponding treatment conditions.

Sample Name	Treatment parameters			
	Acid	Acid Molarity (M)	Digestion Temperature (°C)	Calcination Temperature (°C)
RM[a]	-	-	-	-
RM-C500	-	-	-	500
MRM-1	HCl	6M	85	-
MRM-1-C500	HCl	6M	85	500
MRM-2	HCl	6M	220	-
MRM-2-C500	HCl	6M	220	500
MRM-2-C400	HCl	6M	220	400
MRM-2-C300	HCl	6M	220	300
MRM-3	HCl	4M	85	-
MRM-3-C500	HCl	4M	85	500
MRM-4	HCl	2M	85	-
MRM-4-C500	HCl	2M	85	500
MRM-5	H_2SO_4	6M	85	-
MRM-5-C500	H_2SO_4	6M	85	500
MRM-6	H_2SO_4	4M	85	-
MRM-6-C500	H_2SO_4	4M	85	500
MRM-7	H_2SO_4	2M	85	-
MRM-7-C500	H_2SO_4	2M	85	500

[a] As-received RM

4.3 Characterization Methods

4.3.1 X-Ray Diffraction (XRD)

X-Ray diffraction spectrometer is used for the qualitative identification of the crystal structure of a compound. To produce X-rays, a tungsten hot filament is used to emit a beam of electrons to bombard a metal target such as Cr, Fe, Co, Ag, Cu or Mo which results in X-ray production. When X-rays passes through a sample, the electric vector of the radiation interacts with the electrons in the atoms of the sample which produces scattering. The ordered environment of a crystal causes this scattering and as a result either constructive or destructive interference occurs among the scattered rays. The reason is the same order of magnitude of the distances between scattering centers and wavelength of the radiation. This is called diffraction. The conditions for constructive interference is expressed by Bragg's law (equation 1) where Θ is the angle between crystal surface and beam of radiation, n is an integer, d is the interplanar distance of the crystal and λ is the wavelength of the incident wave. If the angle of incidence does not satisfies equation 1, at all other angles destructive interference takes place [2-4].

$$\sin\Theta = n\lambda / 2d \qquad \text{(equation 1)}$$

The intensity of the reflected X-rays are recorded by a detector. The XRD spectra consist of peaks of different intensities at certain 2Θ values showing that the sample satisfies Bragg's law proving that constructive interference occurs.

A Bruker D8 Discover X-Ray Diffraction instrument with a Cu $K\alpha_1$ radiation source with a employed wavelength of 1.5418 Å was utilized for phase detection. 40 kV and 40 ma were set as the power rating values. A divergence slit was set to 1mm and a 1D detector (Vantec-1) was used to detect diffracted X-rays. The range of the of 2Θ was between 10-90° with a step size of 0.01263°.A sample amount of approximately 5 to 10 mg was put on a double sided tape. This double sided tape was attached to a glass slide and it was put on a sample holder. To level the sample a gum was used between the glass slide and the sample holder. ICDD PDF-4 2014 database was used for phase identification by subtracting the background.

4.3.2 X-Ray Fluorescence

X-Ray Fluorescence spectrometer is a non-destructive method to determine the chemical compounds in rocks, minerals, sediments or fluids quantitatively. X-Ray beams with sufficient energy hits the electrons of the inner shells of the sample to be analyzed. Electrons are displacing from the inner orbital shell if the energy of the X-ray affecting the sample has a higher energy than the binding energy of the electrons it interacts. Since the energies of the shells of the electrons are unique, once an electron is knocked out and this space is replaced by an outer electron, an X-ray is released unique to its atom. The detector measures the intensity of the released beam. The intensity of these detected beams is proportional to the amount of each element in the sample [5].

Elemental composition was determined by a Bruker S8 Tiger XRF Spectrometer in standardless mode working under helium atmosphere with a 18 mm mask. Powdered samples were loaded in to a sample cup (Chemplex Industries Inc., Cat.No:1430) with a thin film support (Prolene film with 4μm thickness, Chemplex Industries, Inc., Cat.No:426). For this film the typical impurities are detected as Ca, P, Fe, Zn, Cu, Zr, Ti, Al at the ppm level. “Loose powder” method was used for measurements by choosing “Best analysis” and “Oxides”. For the measurement a 4 KW, Rh anode X-ray tube was used to generate X-rays. To interpret data SpectraPlus Eval2 V2.2.454 was used.

4.3.3 Thermogravimetric Analysis (TGA)

Thermogravimetric analysis is a test method of measuring the mass of a sample online under varying temperature and gas atmosphere conditions for stability measurements. Usually the temperature of the sample is increased linearly with time. If necessary, the behavior of the mass loss of a sample under constant temperature can be also observed for a certain time period. The sample is placed on a pan (made of aluminum, alumina or platinum) and placed into a furnace where temperatures up to 1000 °C can be reached. To prevent oxidation of the sample, in general, nitrogen or argon is used to purge the furnace. Quantitative information is obtained by a thermobalance [2]. It is possible to measure whether the sample exhibits weight change due to thermal degradation, heterogeneous reaction, oxidation, crystallization, evaporation, phase change etc. The weight change as a function of temperature gives the TGA curve where % mass change is on the vertical axis and temperature or time is on the horizontal axis [6]. The factors which influence the TGA curve are heating rate, sample amount, pan material, volume of sample and scanning rate.

A TA Instruments TGA Q500 model instrument was used for thermogravimetric analysis. In flowing N_2 atmosphere (60 ml/min) 800 °C was reached with a ramp of 2 °C/min. Approximately 15 mg powder sample was loaded on a platinum pan.

4.3.4 Fourier Transform Infrared (FTIR) Spectroscopy

Infrared spectroscopy is used for the determination of molecular species of all types qualitatively and quantitatively. By IR absorption, emission, and reflection spectra of a molecular specie it is possible to assume that all are due to the changes in energy by the transition from one vibrational or rotational energy state to another. In other words, a molecule have to undergo a net change in dipole moment as it vibrates or rotates in order to absorb IR radiation. There are three types of IR absorption instruments which are: dispersive instruments, nondispersive instruments, and Fourier transform spectrometers. Using Fourier transform instruments has several advantages such as, speed, reliability, signal-to-noise ratio advantage, and convenience [2]. In an IR spectrometer a source is emitting IR energy and enters an interferometer. Most of the instruments are based on Michelson interferometers. The interferometer produces a single type of signal resulting in an interferogram signal. This beam is directed to the sample and some of the specific frequencies of energy unique to a sample is absorbed whereas some of it passes through. The beam passing to the detector is measuring the signal which results in a spectrum showing either transmittance or absorbance at specific wavenumbers. FTIR spectroscopy enables to detect the frequencies of vibrational motion of the atoms in a molecule. In other words it gives information about the bond structure. Therefore FTIR is used widely in organic material identification [7,8].

A Bruker Vertex 80v spectrometer in transmission mode at a spectral resolution of 2 cm^{-1} was used for measuring the FTIR spectra. Air and moisture were excluded while recording. Two KBr windows were used to press approximately 10mg of sample. The sample between KBr windows was then loaded into the vacuum sample chamber of the instrument. 256 scans were collected when the sample chamber was evacuated and averaged for each measurement. For background signal 64 scans were collected before each measurement in also under vacuum.

4.3.5 Brunauer-Emmett-Teller (BET) Pore Volume and Surface Area Analysis

The specific surface area of a powder can be determined by the physical sorption of a gas (generally nitrogen) on the surface of the powdered sample. The amount of absorbed gas is calculated corresponding to a monolayer on the surface. Tests are conducted at the temperature of liquid nitrogen and BET theory is used for calculations [9].

BET measurements were performed by a Micromeritics ASAP 2020 – Physisorption Analyzer. Approximately 400 mg sample was used for each measurement and the sample was degassed under vacuum at 120 °C for 8h. The free space measurement was performed in He. The volumetric N_2 adsorption/desorption isotherm was measured between $P/P_0 = 0.01$-0.95 at cryogenic temperature. BET surface area was calculated between $P/P_0 = 0.05$-0.3 using liquid nitrogen (40 data points).

4.3.6 Scanning Electron Microscopy Coupled with Energy-Dispersive X-ray Spectroscopy (SEM/EDX)

Scanning electron microscopy is used for obtaining detailed information for the physical nature of a surface, providing external morphology information. In scanning-electron microscopy high energy accelerated electrons are finely focused on the surface of a sample which generates signals emerging from electron sample interactions. Electrons coming out of the gun are passing through lenses focusing the beam to the double deflection coil accelerating the electrons. When this beam hits the sample, signals produced by interaction include secondary electrons, back scattered electrons, diffracted backscattered electrons, photons and heat. However secondary electrons and back scattered electrons are the most used for obtaining SEM images. Besides these signal X-Ray generation is produced due to inelastic collisions between incoming electrons and the electrons in the shells of the atoms. Similar to other X-Ray spectroscopy techniques, the X-ray generated due to the return of the excited electron to a lower energy state, an X-Ray of unique wavelength for each element is produced. This technique is conducted by EDX systems attached to the SEM instrument. Besides the identification of elements, EDX analysis enables quantitative analysis [10-12].

A Zeiss Evo LS 15 scanning electron microscope was used for obtaining SEM images by analyzing the samples under ultra-high vacuum with an accelerating voltage of 3-10 kV and working distances of 6.0-8.5 mm. A secondary electron detector was used. Images were obtained at various magnifications ranging between 5000 × to 100 000×. EDX experiments were performed by using Rontec xflash 1106 EDX detector. A second instrument is used for some additional SEM images, especially those at magnifications higher than 50 000×. a Zeiss Ultra Plus emission scanning electron microscope to take these additional high magnification images. For images taken by Zeiss Ultra Plus Bruker, under ultra-vacuum, an accelerating voltage of 5 kV and working distance of 3.1 mm, a secondary electron detector was used for obtaining images. For EDX experiments a XFlash 5010 EDX detector with 123 eV resolution was used when using Zeiss Ultra Plus Bruker. Furthermore, STEM images were taken by Zeiss Ultra Plus instrument with a STEM detector.

4.3.7 Inductively Coupled Plasma – Mass Spectrometer (ICP-MS)

This analytical technique is used for elemental determination by combining a high temperature source (inductively coupled plasma) with a mass spectrometer. Atoms in the sample are converted to ions by ICP. These positive metal ions are collected through a differentially pumped interface which is linked to a mass analyzer. By this method a spectra consisting of various peaks referring to a series of isotopes is obtained. Each of these peaks are used to identify the elements present in the sample. To quantitatively analyze the sample, calibration curves where the ratio of the ion count for the analyte to the count for an internal standard is plot as a function of concentration are used. Further information on the working principle of mass spectrometer can be found in the following section [2,13].

For the determination of concentration an Agilent 7700x ICP-MS (Agilent Technologies Inc.,Tokyo,Japan) equipped with octopole reaction system and a helium collision cell for spectral interference removal was used. MicroMist glass concentric nebulizer, quartz Scott-type spray chamber (both from Agilent Technologies, Inc.) and Ni sampler/skimmer cones were employed for ICP-MS operation. 1 μg/L tuning solution was used for short term stability to perform daily instrumental optimization. External calibration solution were prepared by Agilent ICP-MS Multi-element calibration standard-2A (Agilent Technologies, USA). MassHunter softwere was used for the calculations of the analytical results. The instrument settings and parameters are summarized in Table 4.2.

Table 4.2. Operating parameters if ICP-MS.

Operating parameters	Value
# of points per peak	1
Replicates	5
Sweeps/replicate	100
Integration time per mass	0.09s
Plasma gas flow (Ar)	15 L/min
He gas flow (collision cell)	4.3 ml/min
Carrier gas flow (Ar):	1 L/min
Plasma Forward power	1550 W

4.3.8 Temperature Programmed Reduction (TPR)

Temperature programmed reduction (TPR) experiments are used to determine the reducible metals by flowing a carrier gas (such as hydrogen, nitrogen or argon) through the sample. As the gas flows temperature is increased linearly with time and the consumption of hydrogen can be either monitored by a TCD detector or by a connected mass spectrometer.

An MKS Cirrus 2 mass spectrometer connected to a Micrometrics AutoChem II 2920 instrument was employed for TPR analysis. Approximately 0.1 g sample was heated to 700 °C reached with a Temperature ramp of 5 °C/min under 10%H_2-90% Argon mixture. The sample was hold 2 h at 700 under the mentioned flow. The effluent gas stream was passed through a heated capillary (heated to 120 °C) to be analyzed by the mass spectrometer where it was ionized at 70 eV. Continuously, the mass spectra were recorded between 1-200 atomic mass units (amu). Each scan is taking 13 s from 1 to 200. For the TPR analysis the atomic mass unit 2 ($m/z = 2$) was considered to analyze hydrogen.

4.3.9 High-Pressure Volumetric Adsorption Analysis

By high-pressure volumetric adsorption, adsorption and desorption isotherms can be determined using gases such as nitrogen, hydrogen, methane and carbon dioxide etc. A known amount of adsorptive gas is introduced into a chamber containing the sample to be analyzed. When the sample is in equilibrium with the gas, the pressure is recorded and this process is repeated several times for increasing pressures values. Volume of the gas adsorbed by the sample can be calculated by using this data. Similarly, desorption isotherm can be obtained by decreasing the pressure [14].

Adsorption measurements were carried out by a Micromeritics High Pressure Volumetric Anaylzer (HPVA II). Approximately 0.4 g sample was used for measurements. For the outgassing process, samples were heated up to 100 °C and kept at 10^{-6} bar overnight. After N_2 adsorption measurements, samples were outgassed and dry masses were weighed for both RM and MRM. N_2 adsorption isotherms were obtained by considering the dry masses of the samples.

4.4 Catalytic Performance Measurements and Mass Spectrometer

A mass spectrometer is an instrument where ions are formed and they are separated according to their mass-to-charge ratio, *m/z*. A micro amount of sample is introduced to the system. The atoms or molecules in the introduced sample are ionized by knocking out one or two electrons by a heated filament giving off electrons colliding with the sample. Other possibilities to form ions can be the bombardment with photons, ions, or molecules, thermal or electrical energy. These ions are accelerated into a mass analyzer. Ions are deflected by a magnetic field and sorted. The amount of deflection depends on the mass of ion and the charge of the ion. These two factors are combined in a mass/charge (*m/z*) ratio. The ion detector (mostly electron multiplier) is used for electrically detecting the output. The relative current produced by ions of various mass/charge ratios are seen on a diagram. Mass spectrometers require very low working pressures, in other words, an elaborate vacuum system. Because low pressure hinders the frequent collisions in the mass spectrometer. As a result free ions and electrons can be maintained [2,15,16].

A once-through ½”-quartz tube reactor was placed in a Carbolite split-tube furnace for reduction and catalytic activity measurements. Quartz wool was used to fix the sample in the quarz reactor. Catalysts were reduced at 700 °C (reached with a ramp of 5 °C/min) in H_2 for 2h if not mentioned otherwise. After reduction He was used to purge the catalyst for 45 min at 700 °C. Under pure ammonia flow ammonia conversion was measured online by a Hiden QGA gas analyzer. Both the calibration for H_2, N_2, and NH_3 and the online measurements were performed at an ionization potential of 70 eV and at a sampling pressure of 3.4 10^{-6} Torr. For activation energy measurements, differential conversion conditions were established by keeping the ammonia conversion below 8%. For these activation energy measurement experiments 0.15 g sample was and temperature was varied in a range of 480-550 °C. For the determination of activity at high ammonia conversions at 700 °C, 25 mg of catalyst was mixed with fume silica at a ratio of 1:40. This prepared catalyst silica mixture was placed into the reactor. Blank experiments confirmed that there was no activity due to reactor, fumed silica and quartz wool at the same conditions.

References

[1] K.C. Pratt and V. Christoverson, Hydrogenation of a model hydrogen-donor system using activated red mud catalyst, Fuel. 61 (1982) 460-462.

[2] D.A. Skoog, F.J. Holler, and S.R. Crouch. *Principles of Instrumental Analysis*. Belmont: Thomson Higher Education, (2007).

[3] H. zur Loye, X-ray Diffraction. Retrieved from http://www.chem.sc.edu/faculty/zurloye/xrdtutorial_2013.pdf

[4] Basics of X-Ray Diffraction. Retrieved https://old.vscht.cz/clab/RTG/dokumenty/thermo/xrd/Introduction%20to%20powder%20diffraction.pdf

[5] Handheld XRF: How it works. https://www.bruker.com/products/x-ray-diffraction-and-elemental-analysis/handheld-xrf/how-xrf-works.html

[6] M. McKinnon, Thermogravimetric Analysis (TGA) & Differential Scanning Calorimetry (DSC). Retrieved from http://www.fpe.umd.edu/sites/default/files/documents/LMD-TGA-DSC.pdf

[7] Introduction to Fourier Transform Infrared Spectroscopy. Retrieved from http://mmrc.caltech.edu/FTIR/FTIRintro.pdf

[8] Infrared Spectroscopy. Retrieved from https://www2.chemistry.msu.edu/faculty/reusch/virttxtjml/Spectrpy/InfraRed/infrared.htm

[9] Brunauer, Emmet and Teller (BET) Theory. Retrieved from http://particle.dk/methods-analytical-laboratory/surface-area-bet/surface-area-bet-theory/

[10] S. Swapp, Scanning Electron Microscopy (SEM). Retrieved from http://serc.carleton.edu/research_education/geochemsheets/techniques/SEM.html

[11] Energy Dispersive X-Ray Analysis (EDX). Retrieved from http://www.intertek.com/analysis/microscopy/edx/

[12] KUYTAM Basic SEM Traning Notes of Koç University.

[13] What is ICP-MS and more importantly what can it do? Retireved from http://crustal.usgs.gov/laboratories/icpms/What_is_ICPMS.pdf

[14] HPVA II – High Pressure Volumetric Analyzer. Retrieved from http://particulatesystems.com/Products/HPVA-II-High-Pressure-Volumetric-Analyzer.aspx

[15] E. de Hoffmannand V. Stroobant. (2007 Mass Spectrometry. Chichester, West Sussex, England: John Wiley & Sons.

[16] J. Clark, The Mass Spectrometer. Retrieved from http://www.chemguide.co.uk/analysis/masspec/howitworks.html

Chapter 5

TUNING THE STRUCTURAL CHARACTERISTICS OF RED MUD BY SIMPLE TREATMENTS[1]

5.1 Introduction

Red mud (RM) is a by-product of alumina production process, called the Bayer process. It is known to be a hazardous material for the environment because of its high alkalinity with a pH ranging from 10 to 13 [1,2] and its toxic contents, such as heavy metals, soda, and trace amount of radioactive materials [3]. The water and soil ecosystem are mostly endangered because of this high level of alkalinity. Moreover, it can cause chemical burns when in contact with the skin. Furthermore, the particle size of the RM ranges from a few to hundred μm. The wind can transport these tiny dust particles long distances. Inhalation of the particles may severely affect the lungs. The amount of RM generated per ton of aluminum produced lies between 1.9 to 3.6 tons depending on the type of bauxite ore used [4]. Globally, nearly 120 million tons of RM per year is produced, the global inventory being approximately 3.5 billion tons in 2014 [5]. The storage of RM is, therefore, a serious problem for the aluminum production plants. Accumulation of such huge amounts of hazardous waste is becoming an environmental and health problem especially in areas where aluminum production plants are in operation. The recovery or utilization of RM is extremely crucial not only for the

[1] Contents presented in this chapter has been published in *Ceramics International* by authors, Kurtoğlu, S.F., Soyer-Uzun, S., and Uzun, A. The original manuscript has been reformatted to conform to the format requirements of this thesis.

environment but also for economic reasons, as it contains a large amount of various oxides of the metals; mainly Fe, Si, Al, and Ti [6]. The components and mentioned properties of RM make it an ideal candidate to use it in many areas, such as in ceramics [7-11], construction [12-15], and catalysis [16-20] and it can also be utilized as coagulants [21] or adsorbents [2].

Some treatments are proposed in the literature to enhance the properties of RM by changing its textural properties and chemical composition. These treatments involve i) washing RM with acids like hydrochloric acid (HCl) [22], orthophosphoric acid (H_3PO_4) [16], nitric acid (HNO_3) [23], and sulfuric acid (H_2SO_4) [21], ii) carrying out chemical vapor deposition reactions with ethanol and dried RM [24], iii) addition of polystyrene particles [25], and iv) controlled reduction [24, 26]. Among these treatment methods, acid treatment at mild conditions as proposed by Pratt and Christoverson [22] is the one which can alter the chemical composition of RM significantly. By means of these acid treatments followed by neutralization the pH is lowered as the components such as Na, K, and Ca, are removed. Such components are known as unwanted components for various applications, such as in catalysis [27], thus these acid treatments are crucial for the utilization of RM in various applications. Besides acid treatments, simple washing with water and/or calcinations treatments at high temperatures can also lead to the elimination of Cl containing impurities.

There are several characterization studies of RM and its treated counterparts (generally called activated or modified red mud, MRM) in the literature [26-36]. However, these reports are mostly related to specific applications and do not consider the consequences of systematic variations in treatment conditions on the textural and compositional properties including a variety of changing treatment parameters. Thus, one important obstacle in front of the utilization of RM is the lack of detailed investigations on the elucidation of the consequences of such simple treatments of RM at systematically varying conditions on its textural and compositional characteristics. Here, we focused on detailed characterization of RM by combining electron microscopy, diffraction, and spectroscopy complemented by thermal analysis and mass spectrometry to elucidate the changes in its morphology and chemical composition by simple treatments. We considered the type of acid, its concentration, digestion temperature and calcination temperature as the treatment parameters and varied them systematically. Data illustrate that both the morphology and the chemical composition of RM can be tuned by properly adjusting these treatment parameters, presenting a detailed guideline for modifying RM by simple treatments to tune its physical and chemical characteristics in a wide spectrum. These results offer opportunities to booster the effective utilization of such a key industrial hazardous waste in a variety of cost effective and environmentally friendly engineering applications. For instance, improved surface area can help to increase the dispersion of active metal nanoparticles in supported metal catalysts utilizing RM as support material. In such catalysts, modified chemical content, such as K, can also help to control the catalytic performance via promoter effect. Moreover, in synthesizing geopolymers as an alternative to Portland cement, modified chemical and physical properties of RM can enhance the polymerization reaction by offering better contact between the reactants leading to improvements in mechanical strength.

5.2 Results and Discussions

5.2.1 X-Ray Diffraction

Figure 5.1 shows the XRD pattern of the as-received RM. It displays a complex pattern indicating a mixture of metal oxides and complex minerals. The dominant phase in RM is hematite (Fe_2O_3) displaying features at 24.1, 33.2, 35.6, 40.9, 49.5, 54.1, 62.5, and 64.0° (labeled with 1 Figure 5.1). Besides hematite (Fe_2O_3), rutile (TiO_2), cristobalite (SiO_2), gibbsite ($Al(OH)_3$), calcite ($CaCO_3$), goethite ($FeO(OH)$), sodalite ($K_{1.4}Na_{5.3}Ca_{1.2}Al_6(SiO_4)_6(CO_3)_{0.3}(SO_4)_{0.8}Cl_{0.9}$), and cancrinite ($Na_6(Al_6Si_6O_{24})(CaCO_3)_2$) were also present in the as-received form of RM.

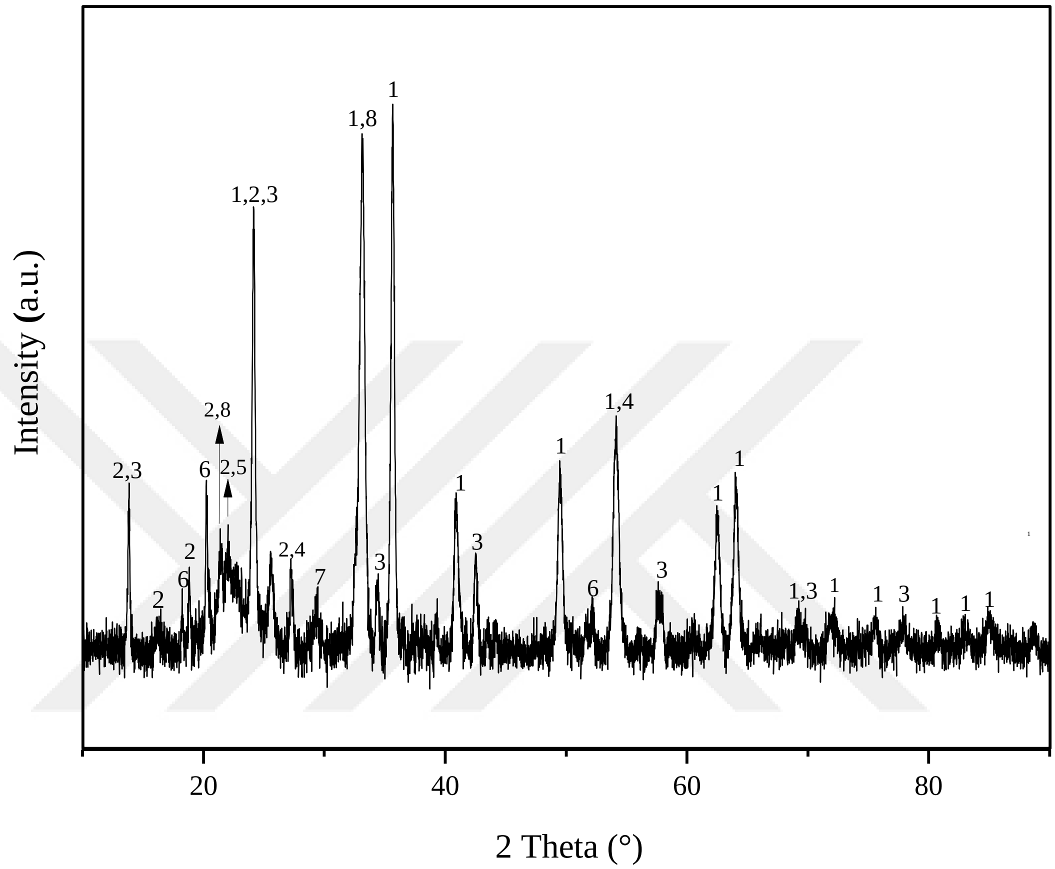

Figure 5.1. XRD pattern of RM: 1 – hematite (Fe_2O_3), 2 – cancrinite ($Na_6(Al_6Si_6O_{24}))(CaCO_3)_2$), 3 – sodalite ($K_{1.4}Na_{5.3}Ca_{1.2}Al_6(SiO_4)_6(CO_3)_{0.3}(SO_4)_{0.8}Cl_{0.9}$), 4 – rutile ($TiO_2$), 5 – cristobalite ($SiO_2$), 6 – gibbsite ($Al(OH)_3$), 7 – calcite ($CaCO_3$), 8 – goethite ($FeO(OH)$).

The XRD patterns of all samples listed in Table 4.1 are given in Figure 5.2. In all MRM samples, the peak at 13.9° (labeled as "2,3" in Figure 5.1), corresponding to the characteristic peak for both complex minerals sodalite and cancrinite, completely disappeared upon acid digestion indicating the dissolution of these phases. Peaks at 24.1° (labeled as "1,2,3" in Figure 5.1) corresponding to hematite (Fe_2O_3), sodalite, and cancrinite in RM became less intense, thus after acid digestion only hematite was left. Decomposition of complex minerals sodalite and cancrinite showed the effectiveness of acid treatment even at very low acid concentrations such as in 2M acid solutions. In all uncalcined MRM samples, the intensity of gibbsite ($Al(OH)_3$) at 18.3° increased (labeled as "6" in Figure 5.1). Besides gibbsite ($Al(OH)_3$), in some HCl treated samples (mainly in MRM-1, slightly in MRM-3 and MRM-4) a new feature at 18.8° was observed that was indicative of the formation of bayerite ($Al(OH)_3$). Furthermore, another peak at 28.4° appeared indicating the formation of diaspore ($AlO(OH)$) in MRM-1 prepared by digestion in 6M HCl at 85 °C. No bayerite or diaspore formation was observed in the H_2SO_4 treated MRM samples (MRM-5, MRM-6, and MRM-7). These findings showed that complex minerals, sodalite and cancrinite, reacted with HCl and formed aluminum hydroxides [35, 37]. In addition, previously it was also shown that Al, most probably coming from sodalite and cancrinite, was partially solubilized to form aluminum hydroxides during alkali precipitation [30]. In addition to aluminum hydroxides certain new peaks were also detected. These new peaks were inferred to be related with the dissolution products. The new feature positioned at 32.6° in the XRD patterns of both MRM-3 and MRM-1 was attributed to a chloride containing dissolution product namely potassium iron chloride ($KFeCl_2$). The new peak appearing at 31.5° in the XRD pattern of MRM-3 prepared by digestion in 4M HCl at 85 °C was thought to be another dissolution product, calcium chloride ($CaCl_2$). On the other hand, in the H_2SO_4 treated MRM samples (MRM-5, MRM-6, and MRM-7) sodium thiosulfate ($Na_2(S_2O_3)$) was detected as indicated by the features at 20.1°, 22.3°, and 29.7°. Furthermore, in H_2SO_4 treated MRM samples, the shoulders on the left and right sides of one the most intense hematite (Fe_2O_3) peaks at 33.2°, were attributed to sodium thiosulfate featured at 32.7°, 32.9°, and 33.5°. These dissolution products show that depending on the acid type used for digestion some residues remain in the samples. For all samples modified with acid, it was seen that cristobalite (SiO_2) was not extracted in the acid solution. However, the peak at 27.4° (labeled as "2, 4" in Figure 5.1.)

corresponding to rutile (TiO_2) and cancrinite lost its intensity in H_2SO_4 digested samples more when compared to those digested in HCl. This may be because of a phase change in rutile or a higher degree of decrease in cancrinite amount in H_2SO_4 treated samples. The peak at 29.4° (labeled with 7 in Figure 5.1) belonging to calcite ($CaCO_3$) was not detected in any type of MRM samples illustrating that it was washed out from the samples upon acid treatment.

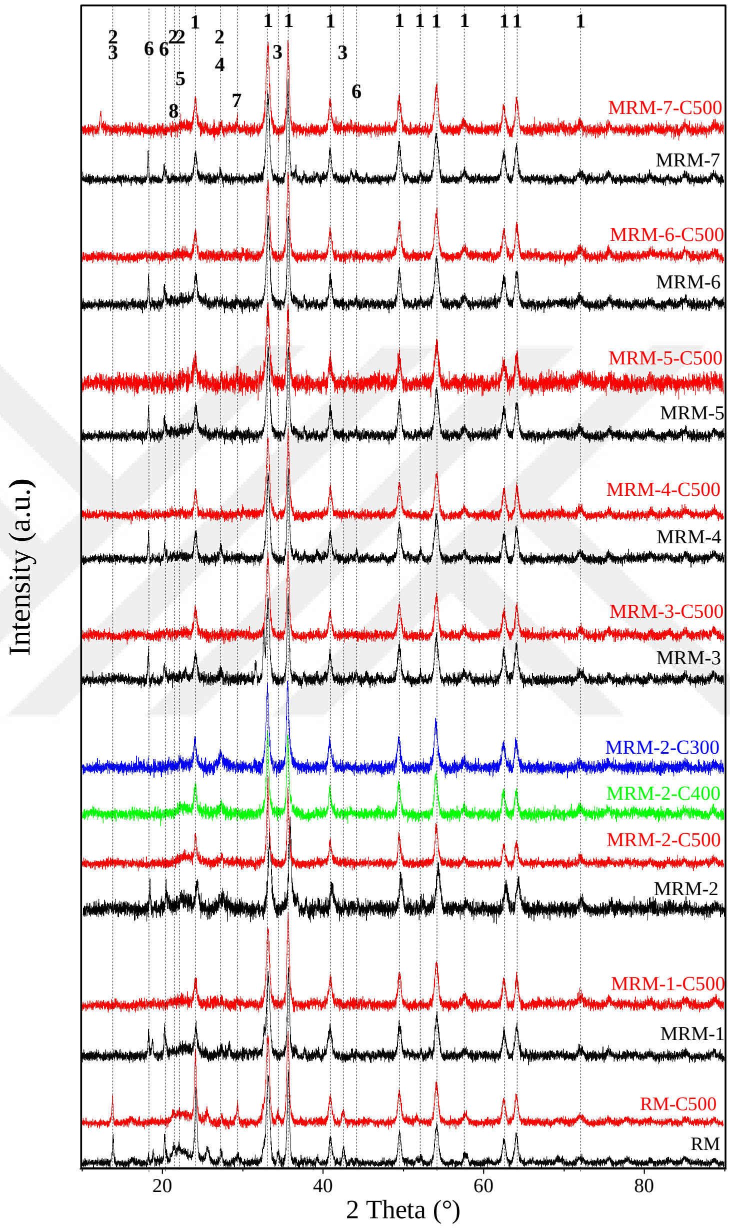

Figure 5.2. XRD patterns of RM, MRM, and calcined MRM samples. 1 – hematite (Fe_2O_3), 2 – cancrinite ($Na_6(Al_6Si_6O_{24}))(CaCO_3)_2)$, 3 – sodalite ($K_{1.4}Na_{5.3}Ca_{1.2}Al_6(SiO_4)_6(CO_3)_{0.3}(SO_4)_{0.8}Cl_{0.9}$), 4 – rutile ($TiO_2$), 5 – cristobalite ($SiO_2$), 6 – gibbsite ($Al(OH)_3$), 7 – calcite ($CaCO_3$), 8 – goethite ($FeO(OH)$) (for numbers refer to Figure 5.1).

XRD results showed that the peak corresponding to goethite ($FeO(OH)$) phase at 21.2° (labeled as “2, 8” in Figure 5.1) completely disappeared in all calcined MRM samples. This was consistent with the result of a previous study that reported the unstability of goethite ($FeO(OH)$) at high temperatures and its decomposition into hematite (Fe_2O_3) [38]. Moreover, XRD features at 20.2, 18.8, and 28.4° corresponding to gibbsite ($Al(OH)_3$), bayerite ($Al(OH)_3$), and diaspore ($AlO(OH)$) phases, respectively, also vanished upon calcination, and consequently, the decomposition into Al_2O_3 was observed [39]. When XRD patterns of the calcined samples inspected, the most intense feature seems to be the hematite (Fe_2O_3). Furthermore all peaks belonging to the dissolution products like $KFeCl_2$ or $CaCl_2$ disappeared in the calcined samples. Even hard to detect due to low crystallinity, there may be still some sodium thiosulfate ($Na_2(S_2O_3)$) contained in the calcined H_2SO_4 treated samples. The peaks characteristic for sodium thiosulfate ($Na_2(S_2O_3)$) appearing as the shoulders next to the hematite (Fe_2O_3) peak around 33° in MRM-5C-500 (digested in 6M H_2SO_4 at 85 °C followed by calcination at 500 °C) were still slightly present.

5.2.2 FTIR Spectroscopy

Figure 5.3 shows the FTIR absorption spectra of RM, MRM, and calcined MRM samples in a wavenumber range of 400-2000 cm^{-1}. The assignment of the individual features based on the conclusions by the XRD results are as follows: The bands located at 942 and 900 cm^{-1} in the FTIR spectrum of RM, were assigned to surface OH bending and inner OH bending vibrations, confirming the presence of Al–(OH) groups [40]. The low frequency bands positioned at 580 and 440 cm^{-1} were attributed to the stretching vibrations of Fe–O corresponding to hematite [41, 42]. The band located at 690 cm^{-1} was thought to be due to the asymmetric and symmetric stretching vibrations of Fe–O bonds in iron hydroxide [43]. In addition to that, another band appearing as a shoulder at 972 cm^{-1} also confirmed the presence of vibrations related to goethite [44]. The bands at 1006 and 618 cm^{-1} are due to the contribution of Si–O and Si–O–Al vibrations [30, 45, 46]. The bands in the region arpou 1100-1190 cm^{-1} were assigned to Ti–O–Ti bonds. The small shoulder at 1067 cm^{-1} was attributed to the asymmetric internal stretching vibrations of AlO_4 and SiO_4 tetrahedra [47]. The FTIR bands in the region between 1200 and 1700 cm^{-1} were assigned to extra framework carbonate groups and hydrous components mainly due to the contribution of cancrinite [48]. The peak at 1404 and 1473 cm^{-1} indicated the presence of stretching modes of the carbonate groups [49], which can be attributed to calcite [35], cancrinite [48], and sodalite [32]. The peak at 1640 cm^{-1} was correlated with OH vibrations in water [50].

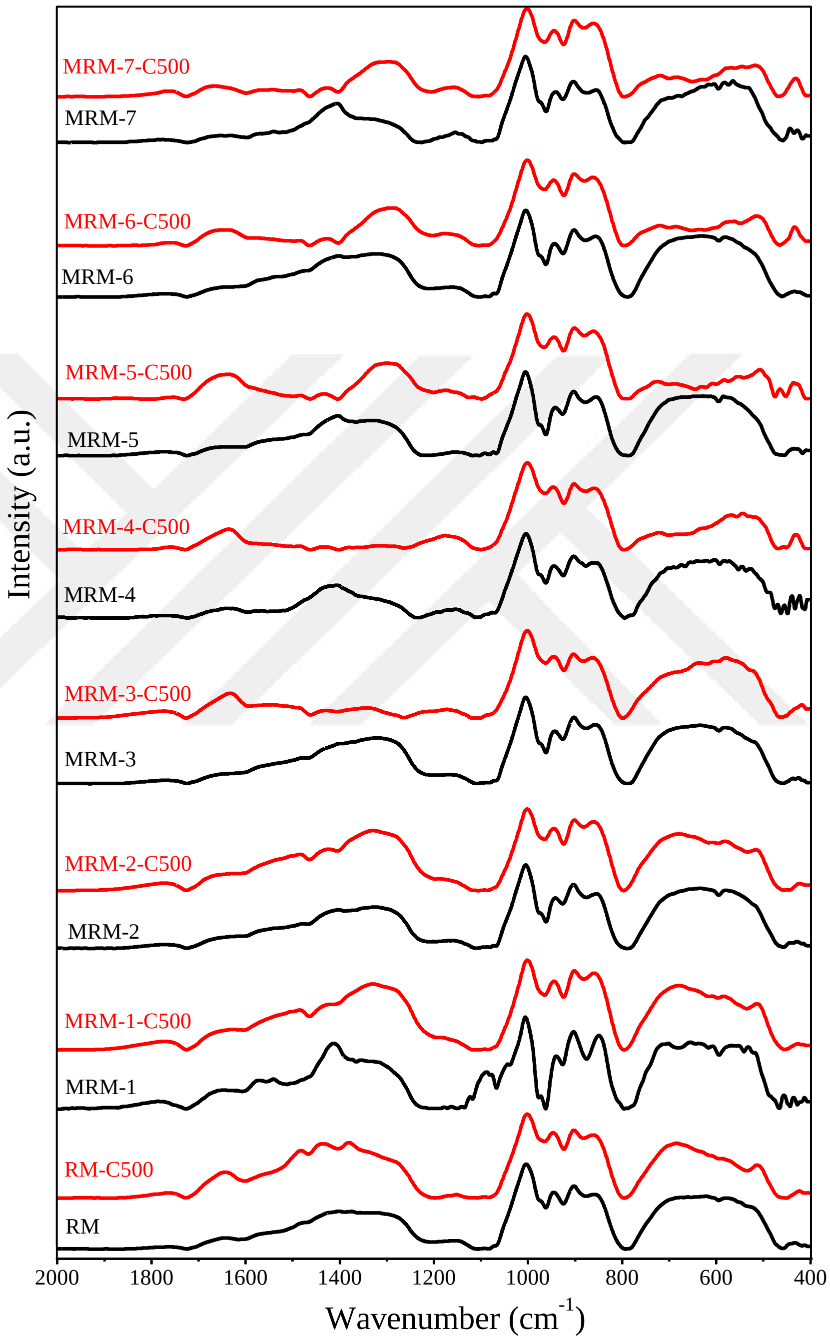

Figure 5.3. FTIR spectra RM and MRM samples together with their calcined (at 500 °C) counterparts.

It is evident from Figure 5.3 that the band located at 900 cm^{-1} designating Al–(OH) bonds in $Al(OH)_3$ slightly gained intensity with acid treatments in all samples. Concomitantly, the feature positioned at approximately 1470 cm^{-1} indicating the presence of carbonate groups of calcite and complex minerals (sodalite and cancrinite) lost intensity considerably. These changes show that complex minerals in RM decompose and some of these form aluminum hydroxides, as also supported by XRD results. The FTIR bands positioned at 1404 and 1473 cm^{-1} remaining after the acid treatments with reduced intensities could be mostly related to atmospheric carbonation [51].

Calcination of acid treated samples resulted in an increase in the intensity of low frequency feature at 580 cm^{-1} indicating vibrations of Fe–O bonds. This feature implies that the samples yielded even higher iron oxide amounts after calcination upon the removal of dissolution products containing Cl and hydroxides of mostly Al. This finding was also supported by XRD patterns of the calcined samples (Figure 5.2) showing that hematite phase became the dominant phase due to the decompositions of iron hydroxides to hematite and the decomposition of complex minerals. Calcination also resulted in the disappearance of a shoulder positioned at 972 cm^{-1} indicating the decomposition of goethite to hematite as indicated by XRD results.

Sharp feature positioned at 1410 cm^{-1} in the FTIR spectra of H_2SO_4 treated samples (MRM-5, MRM-6, and MRM-7) were attributed to SiO_2–SO_4^{2-} and TiO_2–SO_4^{2-} formations [52]. In addition, the band located at 1345 cm^{-1} in MRM-6 and MRM-5 was thought to be related to the stretching frequencies of S=O [53]. Calcination procedure applied on H_2SO_4 treated samples (MRM-5-C500, MRM-6-C500, and MRM-7-C500) resulted in a significant intensity loss of the characteristic peak at 1410 cm^{-1}, whereas the feature at 1300 cm^{-1} gained intensity with calcination. It is known that increasing the temperature in iron oxide-sulfur containing samples under air atmosphere changes the way how sulfur bonds to the oxygen in Fe_2O_3 [53], therefore this shift from 141m^{-1} to 1300 cm^{-1} could designate a modification in the interaction of sulfur with metal oxide. It was also previously reported that peaks at and above 1200 cm^{-1} indicate the formation of adsorbed sulfate or bisulfate-H_3O^+ structures supporting this finding [54]. The strong S=O bands in the H_2SO_4 treated and calcined samples showed that sulfur species were present possibly in a different bonding environment even after the calcination treatment. Therefore, this band shift from 1410 cm^{-1} to 1300 cm^{-1} possibly arose from the structural change of the sulfur species on the metal oxide surfaces. These results agreed with the presence of the peaks attributed to sodium thiosulfate in the XRD pattern of H_2SO_4 treated samples MRM-5, MRM-6, and MRM-7. Additionally, the doubt about the presence of sulfur which could not be clearly detected by XRD due to low crystallinity in the calcined H_2SO_4 samples (MRM-5-C500, MRM-6-C500 and MRM-7C-500) is proven to be present by a strong peak shifted to 1300 cm^{-1}.

5.2.3 X- Ray Fluorescence

The chemical compositions obtained by XRF spectroscopy measurements for all samples are given in Table 5.1. When compared to untreated RM, acid digestion increased Fe_2O_3 percentage from 37 wt.% (in RM) up to 46 wt.% in MRM-3-C500 (digested in 4M HCl at 85 °C followed by calcination at 500°C) while Na_2O, CaO, and K_2O amounts were decreased (Table 5.1). Specifically, Na_2O amount decreased from 9.3 wt.% to a minimum value of 0.2 wt.%, and that of CaO changed from 1.1 wt.% to approximately 0.1 wt.% (Table 5.1). The calcination process mostly led to higher Fe_2O_3 percentages compared to corresponding uncalcined acid digested samples because of the removal of Cl containing impurities by calcination.

Table 5.1. Chemical composition of all samples obtained by XRF analysis.

	Composition of chemicals (wt.%)								
Sample	Fe_2O_3	Al_2O_3	SiO_2	Na_2O	TiO_2	CaO	K_2O	SO_3	Cl
RM	37.2	14.0	11.3	9.3	5.9	1.1	0.30	0.2	0.02
MRM-1	41.7	16.9	11.8	0.3	6.3	0.4	0.04	0.2	4.6
MRM-2	39.8	12.9	10.2	0.2	6.2	0.2	0.02	0.2	5.5
MRM-3	41.6	13.5	9.26	0.5	6.3	0.7	0.05	0.1	5.6
MRM-4	40.9	15.7	11.9	0.9	6.3	0.9	0.06	0.1	3.2
MRM-5	37.7	12.9	10.3	0.3	5.1	0.4	0.03	8.7	0.02
MRM-6	44.5	15.0	11.1	0.2	6.1	0.4	0.03	3.3	-
MRM-7	39.8	14.1	10.7	0.5	6.2	0.6	0.05	5.7	-
RM-C	37.1	14.9	12.1	9.3	5.8	1.2	0.31	0.2	0.03
MRM-1-C500	45.6	18.2	12.5	0.5	7.0	0.5	0.04	0.2	0.4
MRM-2-C500	45.7	13.9	10.9	0.2	6.8	0.2	0.02	0.2	0.5
MRM-2-C-400	45.3	15.9	12.3	0.3	7.1	0.1	0.02	0.2	1.2
MRM-2-C-300	44.3	16.1	12.4	0.3	7.0	0.2	0.03	0.2	3.3
MRM-3-C500	46.3	16.2	10.8	0.9	7.1	0.8	0.06	0.1	0.5
MRM-4-C500	43.6	17.2	11.9	1.0	6.7	0.9	0.07	0.1	0.4
MRM-5-C500	38.0	13.4	10.4	0.3	5.1	0.4	0.11	9.0	-
MRM-6-C500	43.0	17.5	11.5	0.2	6.1	0.3	0.04	3.7	-
MRM-7-C500	40.8	16.2	11.3	0.7	6.2	0.6	0.1	6.2	-

MRM-6-C500 was an exception which showed a lower Fe_2O_3 percentage when compared to MRM-6. Furthermore, only for the sample MRM-5 and MRM-5-C500, Fe_2O_3 concentration of 37 wt.% remained nearly constant with respect to RM. The significant decrease in Na, Ca, and K upon acid treatment and calcination confirmed the findings obtained by XRD and FTIR such that calcite, complex minerals, namely sodalite and cancrinite, which are the main reason for the high alkalinity of RM, decomposed upon acid treatment, causing a drastic decrease in these caustic components. SiO_2 and TiO_2 compositions, on the other hand, did not seem to change significantly after any type of treatment. The loss of Cl containing impurities and both chemically (lost during decomposition of hydroxides to oxides) and physically bound water is thought to be the reason for the increase in Fe_2O_3 wt.% upon calcination. For HCl digested samples (MRM-1, MRM-2, MRM-3, and MRM-4) the presence of relatively high Cl amount due to HCl treatment was lowered from approximately 5 to 0.5 wt.% by calcination at a temperature of 500 °C (Table 5.1). However, the high S amount (up to approximately 9 wt.%) in the H_2SO_4 digested MRM samples (MRM-5, MRM-6, and MRM-7) could not be eliminated by calcination at the same temperature (500 °C). This behavior was also confirmed by the presence of strong bands assigned to S=O bonds in the FTIR spectra of MRM-5-C500, MRM-6-C500, and MRM-7-C500 (Figure 5.3). It was thought that this could be one of the main reasons for observing a much higher Fe_2O_3 content in HCl treated and calcined samples compared to their H_2SO_4 treated counterparts. The loss of Cl and S in these samples is as important as reducing Na and Ca content as all of these components are known to promote sintering and redispersion especially in the field of catalysis [6, 55] leading to deactivation of the active sites.

Furthermore, for MRM-2 samples (prepared by digestion in 6M HCl at 220 °C) calcined at various temperatures (MRM-2-C500, MRM-2-C400, and MRM-2-C300) it was observed that decreasing calcination temperature from 500 to 300 °C caused a slight decrease in Fe_2O_3 amount from 45.7 to 44.3 wt.% with an increase in Cl amount from 0.5 to 3.3 wt.%. The amount of S and Cl in these samples play an important role in terms of determining the Fe_2O_3

wt.% for both HCl and H_2SO_4 treated samples. As expected, it is possible to modify Cl amount by changing calcination temperature for HCl digested samples.

5.2.4 Thermogravimetric Analysis (TGA)

Thermogravimetric analysis curve (TG) and its differential counterpart (DTG) of RM and MRM samples are given in Figure 5.4 a and b, respectively. Similarly, TG and DTG of the calcined samples are given in Figure 5.4 c and d. The results of the thermal analysis of RM (black line in Figure 5.4 a.) showed a continuous weight loss of 7.7 % from 20 to 800 °C. The weight loss of RM with increasing temperature takes place in three main steps. The first step includes the evaporation of physically contained water in RM [1, 17]. This step can be shown as a broad peak in the DTG curve in Figure 5.4 b beginning at 40 °C and ending at 190 °C. This region can also be seen in the TG curve of RM in Figure 5.4 a up to 190 °C just before a steep decrease. The second step comprises of the loss of chemically bond water due to decomposition of some hydroxides [30]. The beginning of a sharp drop of the TG curve exists at 190 °C which can be assumed as the beginning of the second step. The peaks of the DTG curve of RM centered at 225 and 265 °C are combined peaks of the second region showing water formation due to several decomposition reactions, namely, the decomposition of goethite (FeO(OH)) to hematite (Fe_2O_3), gibbsite ($Al(OH)_3$) to diaspore (AlO(OH)), and diaspore (AlO(OH)) to alumina (Al_2O_3) [33,56]. These results are also consistent with the XRD results showing the decomposition of hydroxides with calcination (treatment at elevated temperatures under oxygen atmosphere) in RM and MRM samples. The third weight loss step starting after 560 °C and ending at 720 °C is inferred to be mainly due to CO_2 formation released during the calcite decomposition [1,17,34]. While calcite decomposition occurs at these high temperatures exceeding 560 °C under nitrogen atmosphere during thermogravimetric analysis, decomposition of calcite takes place during calcination under air atmosphere at temperatures lower than 500 °C according to XRD results. The main mass loss observed in the TG curve is from 190 to 500 °C, mainly corresponding to the continuing water formation during the conversion of hydrates to oxides. Independent of the acid type, each modified sample undergoes similar conversion of hydroxides to oxides in the region of 200-300 °C indicated by a steep drop in the TGA curve (Figure 5.4 a) accompanied by sharp peaks in the DTG curve (Figure 5.4 b) of MRM samples. Furthermore, the weight loss of the modified samples is higher compared to that of RM, because of the additional residues and components left from the acids used, as indicated by the XRF and XRD results. In general, the HCl digested samples (MRM-1, MRM-2, MRM-3, and MRM-4) show a similar decomposition pattern compared to each other; however, they differ in the total amounts of component decomposed. This similar pattern may be due to the release of Cl at high temperatures. According to XRF results, the two high Cl containing samples MRM-2 (digested at 220 °C in 6M HCl) and MRM-3 (digested at 85 °C in 4M HCl) exhibit the highest weight lost followed by MRM-1 and MRM-4. H_2SO_4 digested MRM samples (MRM-5, MRM-6, and MRM-7) show a similar decomposition pattern among each other. This pattern is different than the one observed for HCl digested samples. MRM-5 has a higher weight loss amount and also exhibits a broad peak located at 623 °C in the DTG curve (Figure 5.4 b) showing evidence of a different type of decomposition than calcite decomposition in this region. With the beginning of the mass loss period around 623 °C a sharp decrease in the TGA curve (Figure 5.4 a) was observed, causing MRM-5 (digested in 6M H_2SO_4 at 85 °C) to be the sample with the highest weight loss value among all MRM samples. According to XRF results MRM-5 contains the highest amount of S which cannot be eliminated by calcination at 500 °C. Therefore, this second drop in the TGA is most probably due to the lost of S requiring high temperatures for removal. This idea can also be supported by the fact that MRM-5 displaying the highest S amount exhibits the highest weight loss, while MRM-6 with the lowest S content exhibiting the least weight loss at temperatures exceeding 600 °C.

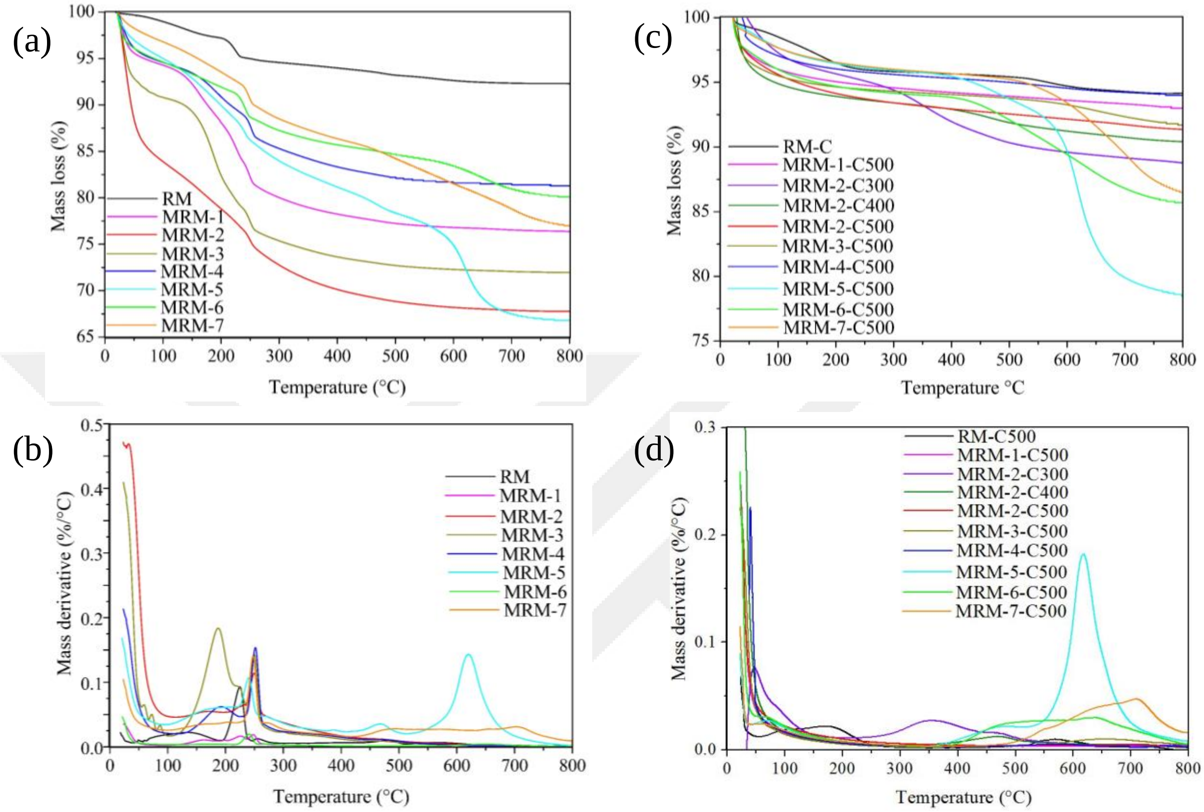

Figure 5.4. (a) TG and (b) DTG curves of RM and MRM samples; (c) TG and (d) DTG curves of RM-C and MRM-C samples.

After calcination, the TGA patterns show similarities for the samples digested in the same type of acid as shown in Figure 5.4 c. HCl treated calcined MRM samples and RM-C also exhibit a very similar weight loss pattern displaying low weight losses when compared to their uncalcined counterparts in Figure 5.4 a. This is an expected result because after calcination, Cl containing impurities, and chemically and physically bond water were released from the samples, therefore a low weight loss in the TGA pattern is observed for calcined HCl treated and RM samples. As mentioned, even calcined, the H_2SO_4 treated samples show a high amount of weight loss shown in Figure 5.4 c especially for MRM-5-C500 (21.5 wt.%). After calcination of this sample the intense peak at 623 °C is still present in the DTG curve (Figure 5.4 d). This behavior was evaluated based on the XRF results indicating that higher calcination temperatures (above 600 °C) are required to get rid of S containing impurities left from the digestion procedure in H_2SO_4 then those digested in HCl. However, it should be kept in mind that these high temperatures may lead to sintering and decrease in surface area.

It should also be noted that a broad peak centered at 350 °C is observed in the DTG curve of MRM-2-C-300 (digested in 6M HCl at 220 °C followed by calcination at 300 °C) showing that calcination at 300 °C is not enough for removing Cl containing impurities and for the completion of hydroxide decompositions (Figure 5.4 d).

5.2.5 Scanning Electron Microscopy (SEM)

Figure 5.5 shows the SEM images of as-received RM and its modified counterparts. RM has a relatively porous structure and it is a complex mixture of various components. Therefore, it is not easy to differentiate between the SEM images of modified samples to analyze the morphology differences.

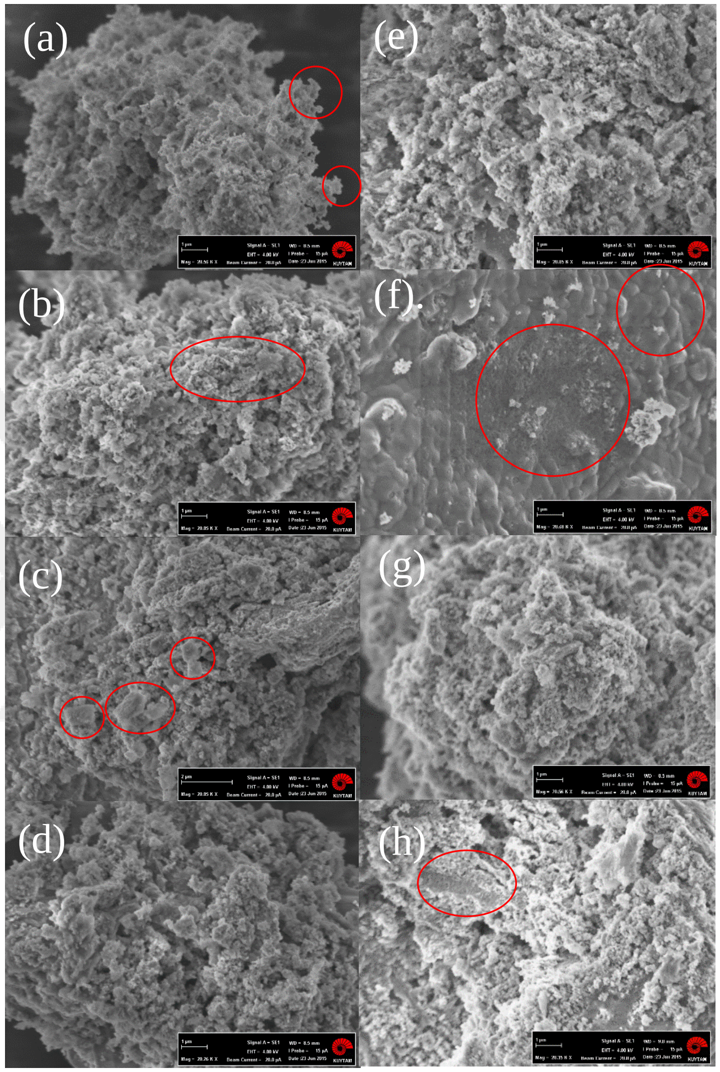

Figure 5.5. Representative SEM images of (a) RM. The regions marked with red circle shows branch looking structure divaricating from the surface, (b) MRM-1. Red oval encloses smaller and more dispersed particles, (c) MRM-2. Rectangular shaped structures are shown by red enclosures, (d) MRM-3, (e) MRM-4, (f) MRM-5. Red circles point out smooth morphologies and bubble like formation, (g) MRM-6, and (h) MRM-7. Red oval shows a smooth region on the surface.

SEM image of RM (Figure 5.5 a) displayed small round and irregularly sized and shaped aggregates as marked with red circles, suggesting a poor crystalline structure [45, 57]. These irregularly sized and shaped grains of RM are very similar to hematite ore morphology, signifying that hematite is the dominant component of RM [58] as shown above by the XRD, XRF, and FTIR results. In addition, it is seen that branched looking structures are divaricating from the granulated surface. Besides these most commonly encountered aggregates mainly attributed to hematite, there are some different morphologies spread in the structure of RM. The SEM images of two of these different structures contained in RM and the corresponding EDX spectra are given in Figure 5.6. According to the EDX results, the rod shaped rectangular structure is aluminum oxide. The hexagonal crystalline particle is covered with the typical granules contained in RM and therefore shows an EDX pattern including various elements contained in RM.

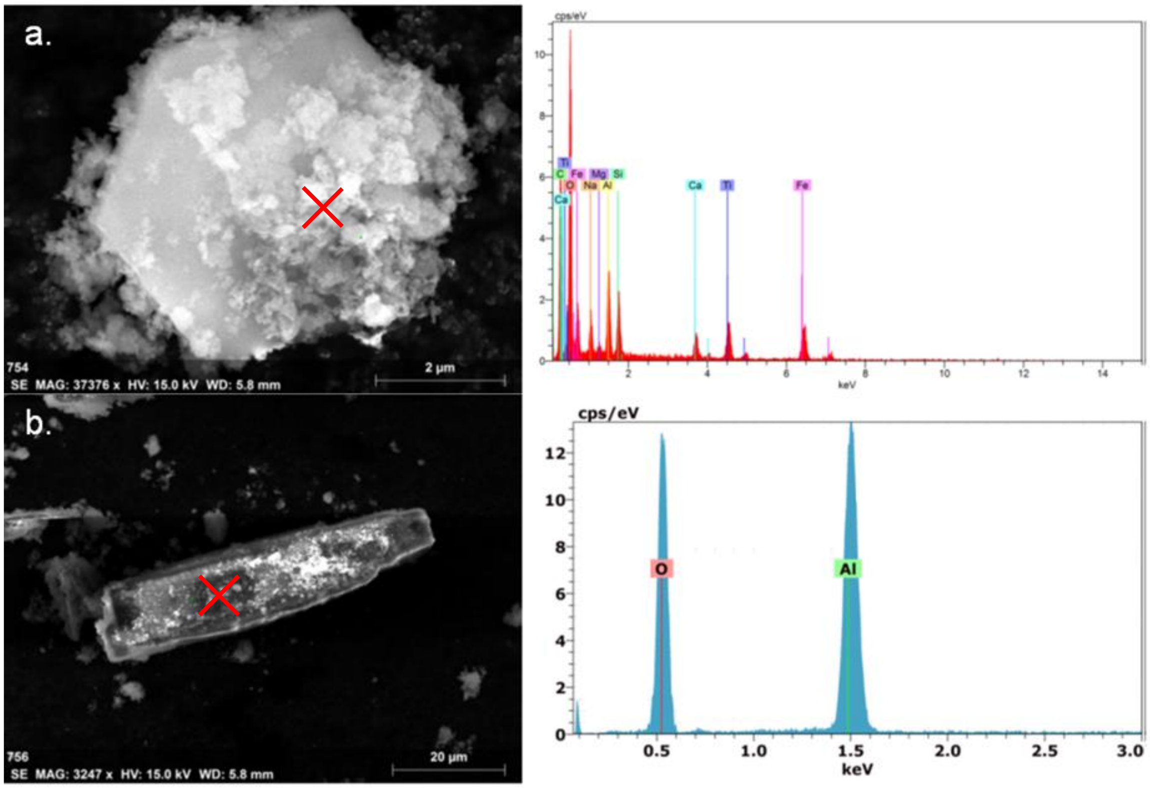

Figure 5.6. (a) A hexagonal and (b) a rod shaped structure in RM and the corresponding EDX spectra.

The branched morphology seen on the surface of RM disappeared after acid digestion. After acid treatment in 6M HCl at 85 °C some smaller particles were detected on the surface of MRM-1 compared to RM. The smaller particles detected on the surface of MRM-1 may be due to the decomposition of complex minerals into smaller particles after acid digestion. Similarly, the newly appearing rectangular shaped structures on the surface of MRM-2 (digested in 6M HCl at 220 °C) are inferred to be related to the dissolution of metal oxides on the surface of RM by the exposure to acid [29, 44]. Consistently, the dissolution of complex minerals was observed by mainly XRD and FT-IR spectroscopy as discussed above.

The acid digestion in HCl and H_2SO_4 results in morphology changes. While HCl causes newly formed particles or smaller particles with smaller pores, H_2SO_4 seems to have a smoothing effect. In the H_2SO_4 digested samples a totally different structure than RM was observed specifically for MRM-5 digested in 6M H_2SO_4 at 85 °C. The surface of MRM-5 became nearly smooth with a bubble-like formation. This was the sample where acid digestion had the most intense alteration in the morphology. Smooth surface morphology was also seen on the surface of MRM-7 prepared at the same temperature but with a lower H_2SO_4 concentration. (Figure 5.5 h).

SEM images of the modified samples after calcination treatments are given in Figure 5.7. After calcination process, several changes in the morphology were observed. For instance, RM-C500 and MRM-4-C500 became slightly more porous exhibiting larger pores upon calcination compared to RM. On the other hand, the surface of MRM-1-C500 became more flat. The particles that appeared on the surface of MRM-2-C500 (digested in 6M HCl at 220 °C followed by calcination at 500 °C) became more distinct and their shapes changed to elliptic and deltoid formations spread on the porous surface. The heat treatment resulted in cracks in MRM-5-C500 and a flat surface appeared for MRM-6-C500 similar to MRM-5-C500. SEM images of MRM-2 samples calcined at varying temperatures of 500, 400, and 300 °C are shown in Figure 5.7 c, i, and j, respectively. Here it is seen that MRM-2-C500 has a more dispersive appearance with more deltoid shaped formations when compared to MRM-2-C400 and MRM-2-C300. However these characteristic deltoid shaped formations related to MRM-2 are also onserved in its calcined versions. The more dispersive structure was previously observed also for hematite phase calcined at high temperature [59].

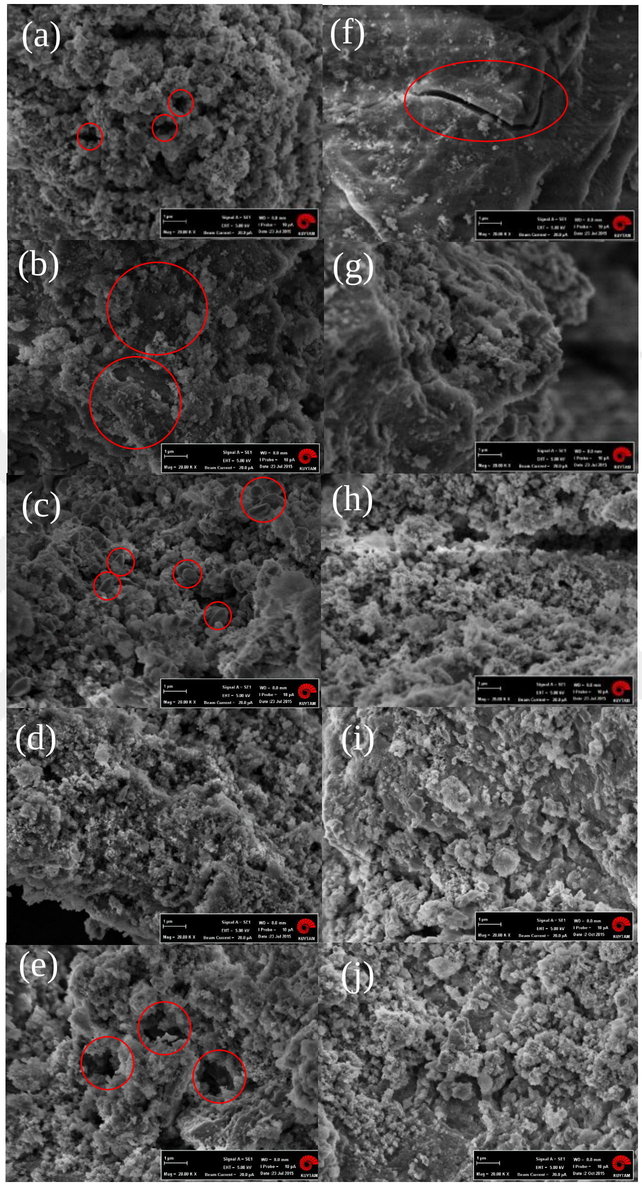

Figure 5.7. SEM images of (a) RM-C500. Red circles show large pores, (b) MRM-1-C500. Flat regions are enclosed by red circles, (c) MRM-2-C500. Red circles show elliptic and deltoid like formations, (d) MRM-3-C500, (e) MRM-4-C500. Large pores are shown by red circles (f) MRM-5-C500. Red oval shows a crack on the flat surface, (g) MRM-6-C500, (h) MRM-7-C500, (i) MRM-2-C-400, and (j) MRM-2-C-300.

5.2.6 BET Analysis

The surface area, pore volume, pore size, and average nanoparticle sizes of the samples prepared are summarized in Table 5.2. It was found that all modifications led to an increase in the surface area compared to that of RM, from 17 m^2/g to values exceeding 200 m^2/g. Among the samples prepared, MRM-2, prepared by digesting at 220 °C in 6M HCl, presented an exceptionally high surface area (232 m^2/g).

Table 5.2. Textural properties of RM.

Sample	Surface area (m^2/g)	Pore volume (cm^3/g)	Pore size (nm)	Average nanoparticle size (nm)
RM	17.9	0.035	11.1	335.6
MRM-1	113.0	0.19	7.0	53.1
MRM-2	232.4	0.17	5.3	25.8
MRM-3	99.8	0.14	6.4	60.0
MRM-4	126.0	0.14	6.1	47.6
MRM-5	55.6	0.06	5.9	107.9
MRM-6	107.8	0.14	6.5	55.6
MRM-7	55.0	0.080	7.2	109.1
RM-C500	23.3	0.034	11.4	257.2
MRM-1-C500	155.6	0.28	7.9	38.5
MRM-2-C500	170.2	0.31	6.9	35.2
MRM-2-C400	204.8	0.31	6.0	29.3
MRM-2-C300	221.0	0.28	5.4	27.1
MRM-3-C500	151.7	0.23	6.5	39.5
MRM-4-C500	133.3	0.18	6.3	45.0
MRM-5-C500	46.8	0.071	6.8	128.2
MRM-6-C500	108.4	0.16	6.8	55.4
MRM-7-C500	53.0	0.080	7.6	113.2

XRD and FT-IR spectroscopy results showed that complex minerals and some meta oxides dissipated by the acid treatments. This decomposition or leaching of these minerals must have caused smaller particles to appear accompanied by an increase in surface area and formation of smaller sized pores. However, there is an obvious difference between the HCl and H_2SO_4 digested MRM samples in terms of their surface areas. In general, data showed that surface areas of the MRM samples digested in HCl were higher (100 m^2/g or higher) than that of samples digested in H_2SO_4 (100 m^2/g or lower). HCl treated MRM-2 displayed the highest (232.4 m^2/g), and H_2SO_4 treated MRM-5 (55.6 m^2/g) and MRM-7 (55.0 m^2/g) samples exhibited the lowest surface areas among the uncalcined MRMs. This phenomenon was also observed in the morphology differences of HCl treated and H_2SO_4 treated MRM samples. For instance, SEM images showed that MRM-2 (Figure 5.5 c) and MRM-2-C500 (Figure 5.7 c) contained newly formed particles or smaller particles on the surface, whereas H_2SO_4 digestion seemed to have a smoothing effect as observed on MRM-5 (Figure 5.5 f) and slightly on MRM-7 (Figure 5.5 h). Since no granule like structure is left especially on MRM-5 that can cause a porous structure or high surface area, these morphological characteristics are in accordance with BET results. The aforementioned smoothing effect of H_2SO_4 treatment was also observed by a previous study [31]. However, MRM-7 prepared by digestion in 2M H_2SO_4 at 85 °C had relatively larger pores than MRM-5 prepared by digestion in 6M H_2SO_4 at 85 °C did. Having nearly similar surface area, pore volume, and nanoparticle size values, this difference caused by a change in H_2SO_4 concentration was the main difference between the textural properties of MRM-5 and MRM-7. The tiny dot looking pores distributed on some regions of the surface of MRM-5 (Figure 5.5 f) explains also the low pore volume and low surface area. MRM-6, digested in 4M H_2SO_4, displayed a higher surface area when compared to the other H_2SO_4 digested MRM samples. Similarly, among the calcined H_2SO_4 treated samples, MRM-6-C500 prepared by the calcination of MRM-6 at

500°C maintains its surface area value and displays the highest surface area among calcined H_2SO_4 treated samples.

Another interesting effect on the textural properties was that increasing acid molarity caused a linear increase in pore size for HCl treated samples prepared by acid digestion at 85 °C (MRM-1, MRM-3, and MRM-4) whereas a similar increase in the acid molarity resulted in a constant decrease in pore size in H_2SO_4 digested samples as it is given in Figure 5.8. Achieving this kind of controllable systematical changes in pore sizes with respect to acid molarity can offer opportunities for effective utilization of RM for desired applications.

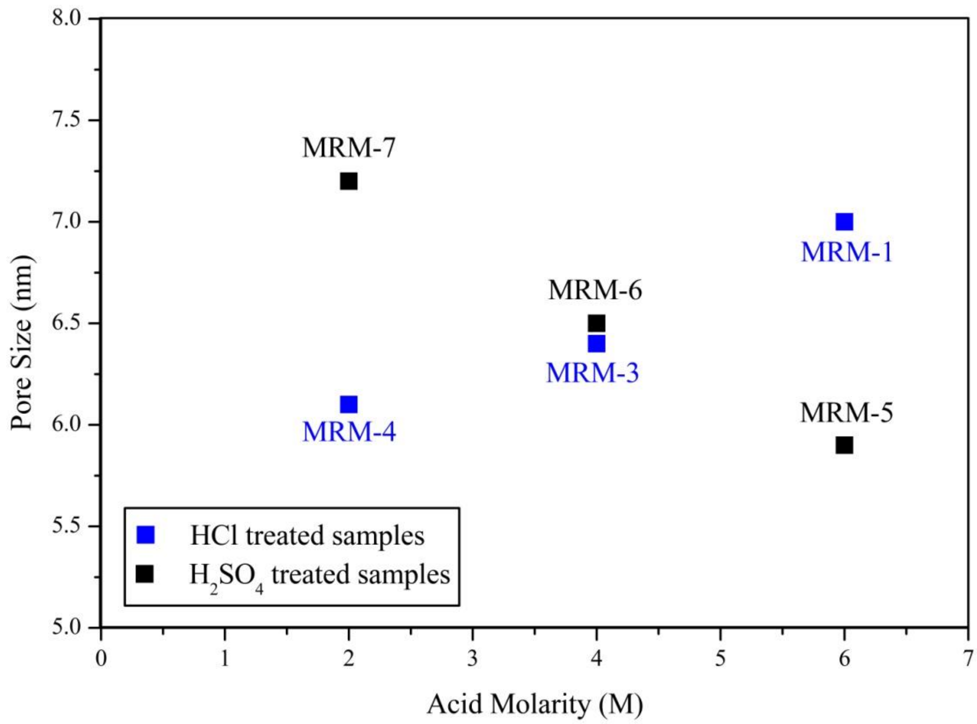

Figure 5.8. Pore size values (nm) of MRM samples digested at 85 °C as a function of the acid molarity; HCl (blue) and H_2SO_4 (black).

Changes in the surface area introduced by calcination may be mainly due to the dehydration of physically and chemically bonded water. For HCl treated samples, calcination at 500 °C caused an increase in the surface area of MRM-1-C500, MRM-3-C500, and MRM-4-C500, while calcination resulted in a decrease in the surface area for MRM-2-C500. Such changes in the surface area induced with calcination can be explained as follows: Initially, pores could be opened due to the release of physically adsorbed water on surface, then the decomposition of components (for instance, the decomposition of $Al(OH)_3$ and FeO(OH) as mentioned earlier) further leads to water release which may form and open pores [34] at higher temperatures. These changes could result in increasing surface areas. On the other hand, calcination at high temperatures could also lead to sintering in some cases, which would affect surface area in a decreasing fashion [27]. H_2SO_4 treated calcined samples MRM-5-C500, MRM-6-C500 and MRM-7-C500 exhibited nearly no change in surface area after calcination. This behavior was possibly related to the remaining S species which was not recovered by calcination at a temperature of 500 °C. It was also observed that pore size and average particle size of MRM-2-C500, MRM-2-C-400, and MRM-2-C-300 systematically decreased with decreasing calcination temperatures (Table 5.2). According to the BET analysis it was observed that treating RM with more concentrated acids did not necessarily result in higher surface areas (Table 5.2). The dissolution of metal oxides and complex mineral molecules was the governing factor as mentioned before. However, complete dissolution of some small particles had a surface area decreasing effect [35] by closing the pores as it is observed in the SEM image of MRM-5 (Figure 5.5 f), and by the textural properties of MRM-5 (Table 5.2) . As it was seen in Figure 5.8, the pore size of 4M HCl and H_2SO_4 treated samples (MRM-3 and MRM-6) were very close, at about 6.5 nm. However, the nature of the acid being used resulted in completely opposite trends in the variation of pore sizes (Figure 5.8). Additionally, the surface areas of MRM-3 and MRM-6 treated with 4M HCl and H_2SO_4 were found to be close to each other. It was inferred that the treatment with 4M acid resulted in nearly the same textural properties independent of the nature of the acid used. However, variations in surface areas do not follow monotonous trends with acid molarity.

Digestion temperature was found to be a critical factor controlling the textural properties of the samples being investigated. MRM-2 that was prepared by digestion in 6M HCl at 220 °C exhibits a twice higher surface area (232.4 m^2/g) than that of MRM-1 produced according to the classical method that involved 6M HCl digestion at 85 °C. To search for the reason of this huge surface area difference, the rod like structures associated to aluminum oxide (Figure 5.6 b) were analyzed further for MRM-1 and MRM-2 by employing SEM as given in Figure 5.9.

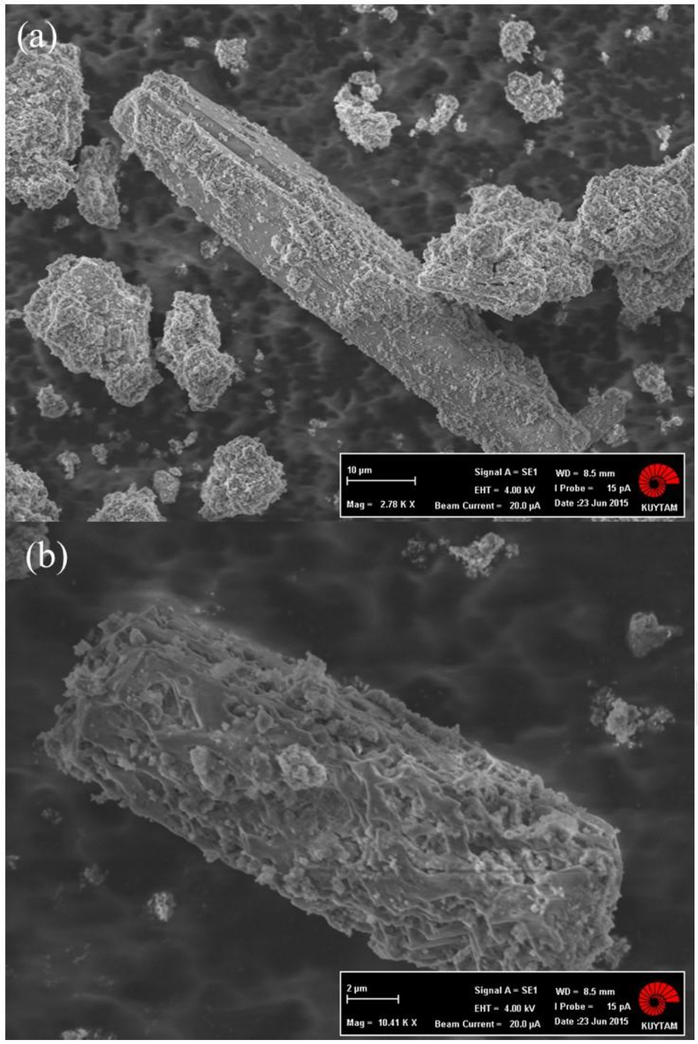

Figure 5.9. SEM images displaying the aluminum oxide structures found in (a) MRM-1 (digested at 85 °C in 6M HCl) and (b) MRM-2 (digested at 220 °C in 6M HCl).

As it is seen in Figure 5.9, the surface of this rod shaped feature exhibited a porous morphology in MRM-2 (Figure 5.9 b), while it preserved its flat and edged surface in MRM-1 (Figure 5.9 a). Higher digestion temperature of 220 °C possibly affected the dissolution of these aluminum oxide particles to a greater extent resulting in higher surface area values which cannot be reached by a lower digestion temperature of 85 °C.

5.2.7 ICP-MS

In the centrifugation step of RM modification, the precipitate should be centrifuged to get rid of the added aqueous ammonia to obtain MRM samples. Na, Mg, Al, K, Ca, Fe, and Ni amounts remained in this collected liquid were determined by ICP-MS is given in Table 5.3. Except for MRM-2 there was no significant iron loss to the liquid during the acid digestion. The reason for slight iron oxide loss in MRM-2 could be due to the high dissolution of iron oxide in acid at 220 °C and possible incomplete recovery of iron oxide during the precipitation with liquid ammonia. As expected, Na, K, and Ca amounts in the extracts increased significantly consistent with the XRF measurements showing the reduction of these contents in the samples.

Table 5.3. Composition of liquid obtained above RM.

	Composition of extracts (g/L)							
Sample name	Na	Mg	Al	K	Ca(43)	Ca(44)	Fe	Ni
Extract of MRM-1	5.63	0.07	0.0001	0.19	0.11	0.18	0.0001	0.0072
Extract of MRM-2	6.08	0.15	0.0003	0.22	0.18	0.28	0.0266	0.0054
Extract of MRM-3	6.43	0.07	0.0007	0.22	0.13	0.20	0.0003	0.0007
Extract of MRM-4	7.90	0.06	0.0000	0.26	0.13	0.20	0.0000	0.0002
Extract of MRM-5	5.05	0.08	0.0001	0.17	0.11	0.17	0.0001	0.0074
Extract of MRM-6	5.79	0.10	0.0001	0.19	0.14	0.22	0.0001	0.0031
Extract of MRM-7	7.57	0.12	0.0001	0.26	0.16	0.26	0.0001	0.0002

5.3 Conclusions

RM obtained from the Eti Seydişehir Aluminum Factory (Konya), was modified by simple acid treatments followed by calcination. The modification parameters investigated were the type of acid used for digestion (HCl and H_2SO_4), molarity of the acid (2M-6M), digestion temperature (85 and 220 °C), and calcination temperature (300 - 500 °C). The samples were characterized by a combination of XRD, XRF, and FTIR spectroscopy, SEM, TGA, and ICP-MS before and after modification treatments to elucidate the effect of treatment conditions on the physical and chemical characteristics of the samples. Results mainly indicated that acid digestions employing HCl and H_2SO_4 cause a significant increase in surface area, a decrease in average particle size, and an enhancement in hematite (Fe_2O_3) percentage due to the loss of K, Ca, and Na components in the system. Increasing temperature of the acid digestion for HCl treated samples from 85 to 220 °C resulted in an exceptional increase in surface area. It was observed that HCl is more appropriate for acid digestion than H_2SO_4, as remnant Cl in the system for HCl treated samples could easily be removed by calcination performed at 500 °C while H_2SO_4 digested samples display high sulfur contents even after calcination at 500 °C. According to TG/DTG results a much higher calcination temperature is required (higher than 600 °C) for the removal of sulfur related components, in the expense of a negative effect on the surface area as it was shown that higher calcination temperature gives lower surface area values. MRM-2 that was digested at 220 °C in 6M HCl is the sample with the highest surface area (232 m^2/g) in the expense of a relatively high Cl percentage of 5.45 wt.%. All calcined samples possess a higher percentage of hematite (Fe_2O_3) compared to RM. The sample with the highest hematite (Fe_2O_3) percentage of 46.3 wt.% (MRM-3-C500) is obtained by digesting RM at 85 °C in 4M HCl. This sample has a nearly 25 % higher hematite content compared to as-received RM. Results presented here clearly illustrate that the physical and chemical properties of RM can be modified in a wide spectrum by relatively cheap and simple treatments. Thus, it is possible to tune the parameters such as surface area, pore volume, pore size, average nanoparticle size, and chemical composition in order to employ RM in various applications such as ceramics, construction and catalysis. This way it can be possible to offer environmentally friendly solutions to various applications by the utilization of this hazardous waste produced in vast amounts.

References

[1] Y. Liu, C. Lin, Y. Wu, Characterization of red mud derived from a combined Bayer Process and bauxite calcination method, Journal of Hazardous Materials, 146 (2007) 255-261.

[2] C.j. Liu, Y.z. Li, Z.k. Luan, Z.y. Chen, Z.g. Zhang, Z.p. Jia, Adsorption removal of phosphate from aqueous solution by active red mud, Journal of Environmental Sciences, 19 (2007) 1166-1170.

[3] C. Klauber, M. Gräfe, G. Power, Bauxite residue issues: II. options for residue utilization, Hydrometallurgy, 108 (2011) 11-32.

[4] A.R. Hind, S.K. Bhargava, S.C. Grocott, The surface chemistry of Bayer process solids: A review, Colloids and Surfaces A: Physicochemical and Engineering Aspects, 146 (1999) 359-374.

[5] S. Xue, F. Zhu, X. Kong, C. Wu, L. Huang, N. Huang, W. Hartley, A review of the characterization and revegetation of bauxite residues (Red mud), Environmental Science and Pollution Research, (2015).

[6] S. Sushil, V.S. Batra, Catalytic applications of red mud, an aluminium industry waste: A review, Applied Catalysis B: Environmental, 81 (2008) 64-77.

[7] Y. Guo, Y. Zhang, H. Huang, K. Meng, K. Hu, P. Hu, X. Wang, Z. Zhang, X. Meng, Novel glass ceramic foams materials based on red mud, Ceram. Int., 40 (2014) 6677-6683.

[8] J. Yang, D. Zhang, J. Hou, B. He, B. Xiao, Preparation of glass-ceramics from red mud in the aluminium industries, Ceram. Int., 34 (2008) 125-130.

[9] X. Chen, A. Lu, G. Qu, Preparation and characterization of foam ceramics from red mud and fly ash using sodium silicate as foaming agent, Ceram. Int., 39 (2013) 1923-1929.

[10] T. Liu, X. Li, L. Guan, P. Liu, T. Wu, Z. Li, A. Lu, Low-cost and environment-friendly ceramic foams made from lead-zinc mine tailings and red mud: Foaming mechanism, physical, mechanical and chemical properties, Ceram. Int., 42 (2016) 1733-1739.

[11] K. Kaya, S. Soyer-Uzun, Evolution of structural characteristics and compressive strength in red mud–metakaolin based geopolymer systems, Ceramics International.

[12] A.I. Bədənoiu, T.H. Abood Al-Saadi, G. Voicu, Synthesis and properties of new materials produced by alkaline activation of glass cullet and red mud, Int. J. Miner. Process., 135 (2015) 1-10.

[13] A.I. Badanoiu, T.H.A. Al Saadi, S. Stoleriu, G. Voicu, Preparation and characterization of foamed geopolymers from waste glass and red mud, Construction and Building Materials, 84 (2015) 284-293.

[14] X. Nie, X. Li, S. Shuai, Research on the property improvement of PVC using red mud in industrial waste residue, IOP Conference Series: Materials Science and Engineering, 2015.

[15] N. Ye, J. Yang, X. Ke, J. Zhu, Y. Li, C. Xiang, H. Wang, L. Li, B. Xiao, Synthesis and characterization of geopolymer from bayer red mud with thermal pretreatment, J. Am. Ceram. Soc., 97 (2014) 1652-1660.

[16] J. Álvarez, S. Ordóñez, R. Rosal, H. Sastre, F.V. Díez, A new method for enhancing the performance of red mud as a hydrogenation catalyst, Applied Catalysis A: General, 180 (1999) 399-409.

[17] S. Sushil, P. Scholz, K. Pollok, B. Ondruschka, V.S. Batra, Application of industrial waste based catalysts for total oxidation of propane, Chem. Eng. J., 166 (2011) 568-578.

[18] J.R. Paredes, S. Ordóñez, A. Vega, F.V. Díez, Catalytic combustion of methane over red mud-based catalysts, Applied Catalysis B: Environmental, 47 (2004) 37-45.

[19] E. Saputra, S. Muhammad, H. Sun, H.M. Ang, M.O. Tadé, S. Wang, Red mud and fly ash supported Co catalysts for phenol oxidation, Catal. Today, 190 (2012) 68-72.

[20] B. Xu, F. Qi, J. Zhang, H. Li, D. Sun, D. Robert, Z. Chen, Cobalt modified red mud catalytic ozonation for the degradation of bezafibrate in water: Catalyst surface properties characterization and reaction mechanism, Chem. Eng. J., 284 (2016) 942-952.

[21] É. Poulin, J.F. Blais, G. Mercier, Transformation of red mud from aluminium industry into a coagulant for wastewater treatment, Hydrometallurgy, 92 (2008) 16-25.

[22] K.C. Pratt, V. Christoverson, Hydrogenation of a model hydrogen-donor system using activated red mud catalyst, Fuel, 61 (1982) 460-462.

[23] F.N. Pei, L. Li, S. Wang, Z. Zhu, G. Lu, Z. Yan, Catalytic ammonia decomposition over industrial-waste-supported Ru catalysts, Environ. Sci. Technol., 41 (2007) 3758-3762.

[24] A.A.S. Oliveira, D.A.S. Costa, I.F. Teixeira, F.C.C. Moura, Gold nanoparticles supported on modified red mud for biphasic oxidation of sulfur compounds: A synergistic effect, Applied Catalysis B: Environmental, 162 (2015) 475-482.

[25] J. Cao, Y. Wang, Z. Yan, G. Li, Polystyrene microspheres-templated preparation of hierarchical porous modified red mud with high rhodamine B dye adsorption performance, Micro and Nano Letters, 9 (2014) 229-231.

[26] R.C.C. Costa, F.C.C. Moura, P.E.F. Oliveira, F. Magalhães, J.D. Ardisson, R.M. Lago, Controlled reduction of red mud waste to produce active systems for

environmental applications: Heterogeneous Fenton reaction and reduction of Cr(VI), Chemosphere, 78 (2010) 1116-1120.

[27] S.C. Kim, S.W. Nahm, Y.K. Park, Property and performance of red mud-based catalysts for the complete oxidation of volatile organic compounds, J. Hazard. Mater., 300 (2015) 104-113.

[28] S. Sushil, V.S. Batra, Characterization of Indian red mud for catalytic applications, Journal of Solid Waste Technology and Management, 37 (2011) 188-196.

[29] M. Ma, G. Wang, Z. Yang, S. Huang, W. Guo, Y. Shen, Preparation, characterization, and photocatalytic properties of modified red mud, Advances in Materials Science and Engineering, 2015 (2015).

[30] J.L. Cao, Z.L. Yan, Q.F. Deng, Y. Wang, Z.Y. Yuan, G. Sun, T.K. Jia, X.D. Wang, H. Bala, Z.Y. Zhang, Mesoporous modified-red-mud supported Ni catalysts for ammonia decomposition to hydrogen, Int. J. Hydrogen Energy, 39 (2014) 5747-5755.

[31] J. Alvarez, R. Rosal, H. Sastre, F.V. Díez, Characterization and deactivation studies of an activated sulfided red mud used as hydrogenation catalyst, Applied Catalysis A: General, 167 (1998) 215-223.

[32] W. Liang, S.J. Couperthwaite, G. Kaur, C. Yan, D.W. Johnstone, G.J. Millar, Effect of strong acids on red mud structural and fluoride adsorption properties, J. Colloid Interface Sci., 423 (2014) 158-165.

[33] M.L.P. Antunes, S.J. Couperthwaite, F.T. Da Conceição, C.P.C. De Jesus, P.K. Kiyohara, A.C.V. Coelho, R.L. Frost, Red mud from Brazil: Thermal behavior and physical properties, Ind. Eng. Chem. Res., 51 (2012) 775-779.

[34] H. Nath, P. Sahoo, A. Sahoo, Characterization of Red Mud treated under high temperature fluidization, Powder Technol., 269 (2015) 233-239.

[35] I. Smičiklas, S. Smiljanić, A. Perić-Grujić, M. Šljivić-Ivanović, M. Mitrić, D. Antonović, Effect of acid treatment on red mud properties with implications on Ni(II) sorption and stability, Chem. Eng. J., 242 (2014) 27-35.

[36] J. Pascual, F.A. Corpas, J. López-Beceiro, M. Benítez-Guerrero, R. Artiaga, Thermal characterization of a Spanish red mud, J. Therm. Anal. Calorim., 96 (2009) 407-412.

[37] S. Norouzi, K. Badii, F.D. Ardejani, Activated bauxite waste as an adsorbent for removal of Acid Blue 92 from aqueous solutions, Water Sci. Technol., 62 (2010) 2491-2500.

[38] F. Jia, K. Ramirez-Muñiz, S. Song, Mechanism of the formation of micropores in the thermal decomposition of goethite to hematite, Surf. Interface Anal., 47 (2015) 535-539.

[39] A.D.V. Souza, C.C. Arruda, L. Fernandes, M.L.P. Antunes, P.K. Kiyohara, R. Salomão, Characterization of aluminum hydroxide ($Al(OH)_3$) for use as a porogenic agent in castable ceramics, J. Eur. Ceram. Soc., 35 (2015) 803-812.

[40] C.A.R. Reyes, C. Williams, O.M.C. Alarcón, Nucleation and growth process of sodalite and cancrinite from kaolinite-rich clay under low-temperature hydrothermal conditions, Materials Research, 16 (2013) 424-438.

[41] B. Janković, I. Smičiklas, J. Stajić-Trošić, D. Antonović, Thermal characterization and kinetic analysis of non-isothermal decomposition process of Bauxite red mud. Estimation of density distribution function of the apparent activation energy, Int. J. Miner. Process., 123 (2013) 46-59.

[42] H. Namduri, S. Nasrazadani, Quantitative analysis of iron oxides using Fourier transform infrared spectrophotometry, Corros. Sci., 50 (2008) 2493-2497.

[43] Y.X. Yang, M.L. Liu, H. Zhu, Y.R. Chen, G.J. Mu, X.N. Liu, Y.Q. Jia, Preparation, characterization, magnetic property, and Mössbauer spectra of the β-FeOOH

nanoparticles modified by nonionic surfactant, J. Magn. Magn. Mater., 320 (2008) L132-L136.

[44] S. Sushil, V.S. Batra, Modification of red mud by acid treatment and its application for CO removal, J. Hazard. Mater., 203-204 (2012) 264-273.

[45] E. Cristina De Resende, I.D.R.G. Carvalho, M. Schlaf, M.C. Guerreiro, Red Mud waste from the Bayer process as a catalyst for the desulfurization of hydrocarbon fuels, RSC Advances, 4 (2014) 47287-47296.

[46] M.K. Sahu, S. Mandal, S.S. Dash, P. Badhai, R.K. Patel, Removal of Pb(II) from aqueous solution by acid activated red mud, Journal of Environmental Chemical Engineering, 1 (2013) 1315-1324.

[47] A. Dziedzicka, B. Sulikowski, M. Ruggiero-Mikołajczyk, Catalytic and physicochemical properties of modified natural clinoptilolite, Catal. Today, 259, Part 1 (2016) 50-58.

[48] G. Della Ventura, G.D. Gatta, G.J. Redhammer, F. Bellatreccia, A. Loose, G.C. Parodi, Single-crystal polarized FTIR spectroscopy and neutron diffraction refinement of cancrinite, Phys. Chem. Miner., 36 (2009) 193-206.

[49] I. Ozer, S. Soyer-Uzun, Relations between the structural characteristics and compressive strength in metakaolin based geopolymers with different molar Si/Al ratios, Ceram. Int., 41 (2015) 10192-10198.

[50] I. Akin, G. Arslan, A. Tor, M. Ersoz, Y. Cengeloglu, Arsenic(V) removal from underground water by magnetic nanoparticles synthesized from waste red mud, J. Hazard. Mater., 235-236 (2012) 62-68.

[51] R.C. Sahu, R.K. Patel, B.C. Ray, Neutralization of red mud using CO_2 sequestration cycle, J. Hazard. Mater., 179 (2010) 28-34.

[52] S.M. Jung, O. Dupont, P. Grange, TiO_2–SiO_2 mixed oxide modified with H_2SO_4: I. Characterization of the microstructure of metal oxide and sulfate, Applied Catalysis A: General, 208 (2001) 393-401.

[53] T. Yamaguchi, T. Jin, K. Tanabe, Structure of acid sites on sulfur-promoted iron oxide, J. Phys. Chem., 90 (1986) 3148-3152.

[54] C.M. Eggleston, S. Hug, W. Stumm, B. Sulzberger, M.D.S. Afonso, Surface complexation of sulfate by hematite surfaces: FTIR and STM observations, Geochim. Cosmochim. Acta, 62 (1998) 585-593.

[55] M.D. Argyle, C.H. Bartholomew, Heterogeneous catalyst deactivation and regeneration: A review, Catalysts, 5 (2015) 145-269.

[56] J.L. Cao, Z.L. Yan, Q.F. Deng, Z.Y. Yuan, Y. Wang, G. Sun, X.D. Wang, B. Hari, Z.Y. Zhang, Homogeneous precipitation method preparation of modified red mud supported Ni mesoporous catalysts for ammonia decomposition, Catalysis Science and Technology, 4 (2014) 361-368.

[57] S. Agatzini-Leonardou, P. Oustadakis, P.E. Tsakiridis, C. Markopoulos, Titanium leaching from red mud by diluted sulfuric acid at atmospheric pressure, J. Hazard. Mater., 157 (2008) 579-586.

[58] E.M. El Afifi, M.F. Attallah, E.H. Borai, Utilization of natural hematite as reactive barrier for immobilization of radionuclides from radioactive liquid waste, Journal of Environmental Radioactivity, 151, Part 1 (2016) 156-165.

[59] C. Zhang, Z. Yu, G. Zeng, B. Huang, H. Dong, J. Huang, Z. Yang, J. Wei, L. Hu, Q. Zhang, Phase transformation of crystalline iron oxides and their adsorption abilities for Pb and Cd, Chem. Eng. J., 284 (2016) 247-259.

Chapter 6

CATALYTIC PERFORMANCE OF RED MUD AND ITS MODIFIED COUNTERPARTS: HYDROGEN PRODUCTION FROM AMMONIA

6.1 Performance of Red Mud and Modified Red Mud-based Catalysts Activated for one hour under NH_3 flow

As received red mud (RM) and modified red mud (MRM) catalysts which were prepared according to the systematic methods explained in Section 4.2 and characterized extensively which was covered in Chapter 5 were tested for ammonia decomposition. It should be noted that in Chapter 5, only calcination temperatures up to 500 °C were investigated. Additionally in this chapter, catalysts were treated under varying calcination temperatures (500-1000 °C) followed by reduction (600-800 °C). Information on treatment temperatures of these catalyst, their activation energy values obtained under differential conversion conditions and H_2 production rates at 500 °C are given in Table 6.1. Apparent activation energy values were obtained by Arrhenius plots given in Figure 6.1. Each catalyst was activated for one hour under NH_3 flow at 600°C.

Table 6.1. Conversion, H_2 production rate and activation energy data of RM and MRM-based catalysts at 500 °C which were activated for one hour under NH_3 flow.

Catalyst	Calcination Temperature / °C	Reduction Temperatur e / °C	Conversion / %	Hydrogen production rate @500 °C /mmol min^{-1} g_{cat}^{-1}	Activation energy / kJ/mol
RM-600R	-	600	3.58	1.51	117.9
RM-700R	-	700	5.1	2.32	139.5
RM-800R	-	800	0.31	0.16	191.0
RM-500C-700R	500	700	4.93	2.16	130.2
RM-700C-700R	700	700	3.90	1.71	123.7
RM-900C-700R	900	700	3.60	1.55	130.4
RM-1000C-700R	1000	700	4.43	1.87	123.1
MRM-1-700R	-	700	0.88	0.47	150.6
MRM-1-500C-700R	500	700	0.96	0.47	154.8
MRM-2-700R	-	700	0.09	0.05	288.7
MRM-2-800R	-	800	0.07	0.02	177.2
MRM-2-500C-700R	500	700	0.32	0.17	180.8
MRM-2-700C-700R	700	700	0.60	0.26	146.2
MRM-2-900C-700R	900	700	2.03	0.93	167.5
MRM-2-1000C-700R	1000	700	2.16	0.88	169.2
MRM-4-500C-700R	500	700	1.48	0.70	153.0
MRM-4-900C-700R	900	700	2.87	1.04	136.2

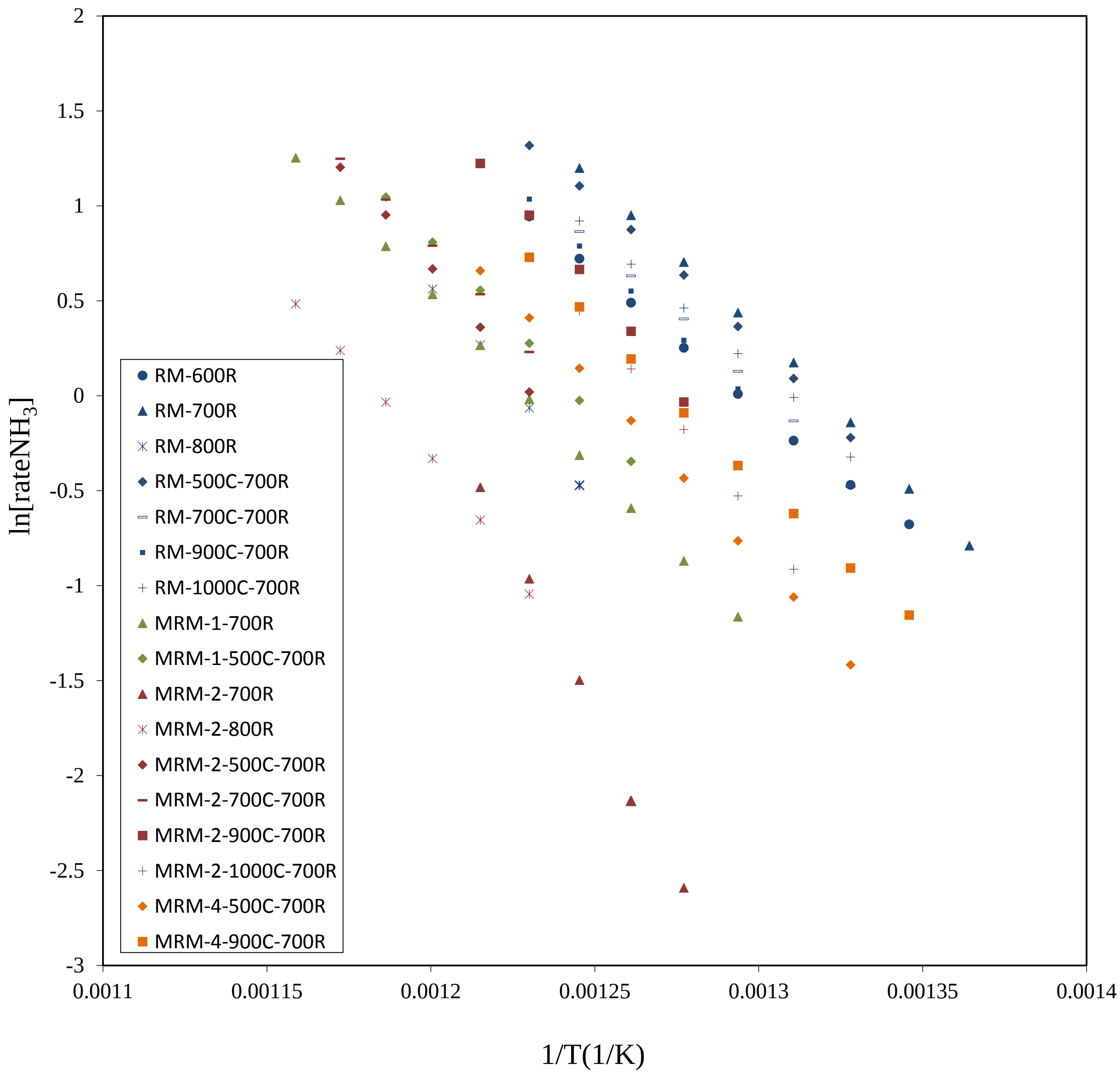

Figure 6.1. Arrhenius plots obtained under differential conversion conditions for RM and MRM-based catalysts.

As Table 6.1 suggests, RM-based catalysts reach higher conversions and higher H_2 production rates at a temperature of 500 °C. However, when interpreting Figure 6.1, one can see that each catalyst has its unique Arrhenius plot suggesting varying apparent activation energies tabulated in Table 6.1. MRM-2-700R which provides one of the lowest H_2 production rates at 500 °C, shows an exceptionally high activation energy when compared to the other catalysts. The high activation energy suggests that if the Arrhenius plot is extrapolated to high temperatures, MRM-2-700R (red triangle in Figure 6.1) shows the highest H_2 production rate at 700°C due to its high slope. Since it is known that Fe-based catalysts perform the best at high temperatures such as 700 °C or higher as mentioned in Chapter 2, MRM-2 was selected among all the given catalysts above, for further investigation at high temperatures. It should be noted that MRM-2 was the sample with the highest surface area as characterized in Chapter 5.

6.2 Performances of Modified Red Mud based Catalyst Activated 10 hours under NH_3 flow

Several additional experiments were performed to elucidate the effect of activation period under NH_3 flow, on the activation energy and performance. The activation energy and H_2 production rate data of catalyst treated 10 hours at 600°C under NH_3 flow are given in Table 6.2.

Table 6.2. Conversion, H_2 production rate and activation energy data of RM and MRM-based catalysts at 500 °C which were activated for 10 hours under NH_3 flow.

Catalyst	Conversion / %	Hydrogen production rate @500 °C /mmol min^{-1} g_{cat}^{-1}	Activation energy / kJ/mol
MRM-1-500C-700R-10h	1.47	1.47	168.5
MRM-2-700C-700R-10h	3.11	3.11	132.1
MRM-2-1000C-700R-10h	4.52	4.52	115.8
MRM-4-900C-700R-10h	3.56	3.56	128.3

From the table it is inferred that the time period for activation has a substantial effect on the catalyst. It increases activation energy of MRM-2-700C-700R, MRM-2-1000C-700R and MRM-4-900C-700R, whereas it decreases for MRM-1-500C-700R-10h. As seen for all four catalysts the H_2 production rate increases at 500 °C. That is why in the following chapter MRM-2-700R having the highest activation energy is investigated deeply to identify the active species formed after varying activation conditions and reaction. Details are given in Chapter 7.

Chapter 7

RED MUD AS AN EFFICIENT, STABLE, AND COST-FREE CATALYST FOR CO_x-FREE HYDROGEN PRODUCTION FROM AMMONIA[2]

7.1 Introduction

Concerns related to safe storage of hydrogen have triggered extensive research on developing novel technologies [1,2]. Some approaches focus on adsorbing hydrogen on porous materials. These approaches have their own limitations [3]. Others consider storing hydrogen chemically in molecules, such as in CH_4. However, in most of these storage molecules there is also carbon present, producing unwanted CO_x upon decomposition. Ammonia, on the other hand, does not include any carbon, thus it offers opportunities for CO_x-free hydrogen storage with a high storage density (17.7 wt.%).

Several Ru-[4-9], Ni-[10-12], and Fe-based [13-16] catalysts are proposed for the decomposition of ammonia into hydrogen and nitrogen. Among these catalysts, Ru-based catalysts are known as the most active ones [17]. However, they suffer deeply from limited availability and high cost of ruthenium. Ni- and Fe-based counterparts can be alternative to the noble metal catalysts, as they can produce relatively high hydrogen production rates. For instance, an Fe-based catalyst spatially confined within the tubes of a mesoporous carbon support was shown to provide over 90 % initial NH_3 conversion at a space velocity of 120

[2] Contents presented in this chapter has been published in *Scientific Reports* (currently in press) by authors, Kurtoğlu, S.F. and Uzun, A. The original manuscript has been reformatted to conform to the format requirements of this thesis.

000 cm^3 NH_3 h^{-1} g_{cat}^{-1} at 700 °C [13]. However, such non-noble metal catalysts require elevated temperatures to be able to reach high hydrogen production rates and at these high temperatures they tend to sinter and deactivate quickly, as in the case of this mesoporous carbon supported iron catalyst [13]. Thus, there is a big need for a cheap catalyst with high and stable performance for producing hydrogen from ammonia. Here, the focus is on an industrial waste, RM, as an environmentally friendly and almost cost-free catalyst.

RM, a by-product of aluminum production process, is formed between 1.9 to 3.6 tons [18] per each ton of aluminum manufactured. This amount adds up to an inventory of annually 120 million tons globally [19]. Such high rate of accumulation has been a serious environmental problem, as RM is known to be hazardous for the environment because of its high alkalinity [20]. Obviously, recovery of RM is of great importance not only for hindering such environment effects but also for economic reasons, as it contains a large amount of metal oxides, such as Fe_2O_3, SiO_2, Al_2O_3, and TiO_2. For this reason, RM was considered to be utilized in various fields including ceramics [21], construction [22], and catalysis [23]. In catalysis, it has been mostly used as supports. For instance, RM-supported nickel [24, 25] and ruthenium [26] catalysts were shown to be active for hydrogen production from ammonia decomposition. However, in general, these catalysts either did not provide high hydrogen production rates or contained expensive noble metals to reach high production rates. Actually, RM contains high amount of iron, an active metal for ammonia decomposition [13]. Thus, it can be utilized directly as catalyst for this reaction; this is the objective of this study. Here, the structure of RM was modified by a simple acid treatment to achieve a significantly high surface area with improved iron content and reduced alkali amount. After reduction at 700 °C, the resulting sample provided exceptionally high and stable hydrogen production rate for ammonia decomposition. Detailed characterization of the used catalyst unveiled that all metallic Fe species formed after the reduction step were converted into ε-Fe_2N readily available on the surface during the reaction, suggesting that these newly formed iron nitride sites are responsible for this high and stable performance. Results presented here offer opportunities to utilize one of the key hazardous industrial wastes as an environmentally friendly, efficient, and almost cost-free catalyst for CO_x-free hydrogen production from ammonia decomposition.

7.2 Results and Discussions

Temperature programmed reduction (TPR) of as-received RM (Eti Seydişehir Aluminum Factory, Konya-Turkey, Contents are listed in Table 7.1 in section 7.4) indicates that the conversion of iron oxide into bulk Fe is completed upon reduction in hydrogen at temperatures exceeding 650 °C (Figure 7.6 in section 7.4) consistent with the results of Costa *et al*. [27] and with the TPR of Fe_2O_3 as shown in Figure 7.7, in section 7.4. X-Ray diffraction (XRD) of RM reduced at 700 °C for 2h in flowing hydrogen (RM-700R) confirms the conversion of iron oxides into metallic iron as indicated by the intense peak at 44.7° (Figure 7.1 b). RM-700R was then tested for ammonia decomposition reaction in a once-through ½”-quartz tube reactor in pure ammonia flow at atmospheric pressure and 500 °C. Data illustrated that RM-700R converts ammonia into hydrogen and nitrogen at a conversion of 5.1% for a space velocity of 42 000 NH_3 cm^3 h^{-1} g_{cat}^{-1} at 500 °C after activation in NH_3 flow for 1 h at 600 °C (this activated RM-700R sample is denoted as RM-700R@600). Figure 7.2 presents the Arrhenius plot obtained on RM-700R@600 in a temperature range from 480 to 550 °C measured under differential conversion conditions (at NH_3 conversions below 10%). The apparent activation energy (E_{app}) was measured as 134.7 kJ/mol. This value is consistent with the literature data reported for other iron-based catalysts [28]. XRD of the used RM-700R@600 catalyst given in Figure 7.1 c shows that the metallic iron was still present together with some newly-formed iron nitride species (Fe_3N_y) indicated by 2θ peaks at 38.7°, 41.4°, and 44.0° (XRD results for a complete 2θ range of 10-90° are provided in Figure 7.8, in section 7.4). These results indicate that activation at 600 °C for 1 h was not sufficient to convert all metallic iron into iron nitride. Thus, on a different run a fresh RM-700R sample was activated at 700 °C in 100 ml/min NH_3 flow for 10 h (named as RM-700R@700). NH_3 conversion on RM-700R@700 increased to 6.8 % under the same conditions. The apparent activation energy measured for RM-700R@700 in a temperature range of 480 to 550 °C was 118.6 kJ/mol, slightly lower than that of RM-700R@600. Scanning electron microscopy (SEM) images, however, do not show any change in the morphology of RM-700R@600 or RM-700R@700 (Figure 7.3 c,d). On the other hand, XRD of RM-700R@700 show that iron is only present in Fe_3N_y form. The absence of metallic iron indicates that its conversion into iron nitride was complete during the activation at 700 °C. It is also noted that the value of *y* in Fe_3N_y nanoparticles increases from 0.94 to 1.39 (as evidenced by a decrease in the peak positions in XRD [29]) upon increasing the activation temperature from 600 to 700 °C accompanied by an increase in activation time from 1 to 10 h. This increase in *y* in Fe_3N_y also indicates a higher degree of nitriding in RM-700R@700 than in the case of RM-700R@600 [29].

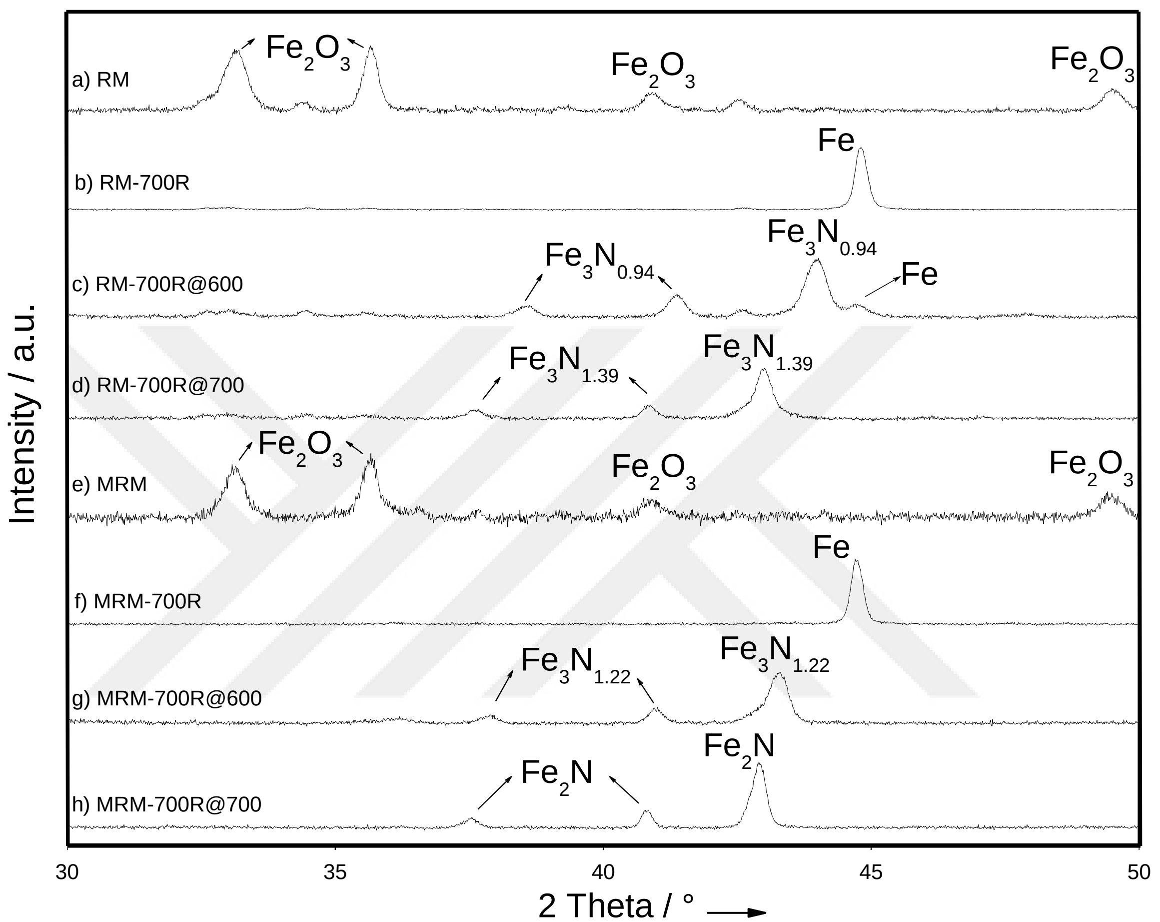

Figure 7.1. XRD pattern of a) RM, b) RM-700R, c) RM-700R@600, d) RM-700R@700, e)MRM, f) MRM-700R, g) MRM-700R@600, and h) MRM-700R@700 between 30-50°. Data for the complete range is provided in section 7.4.

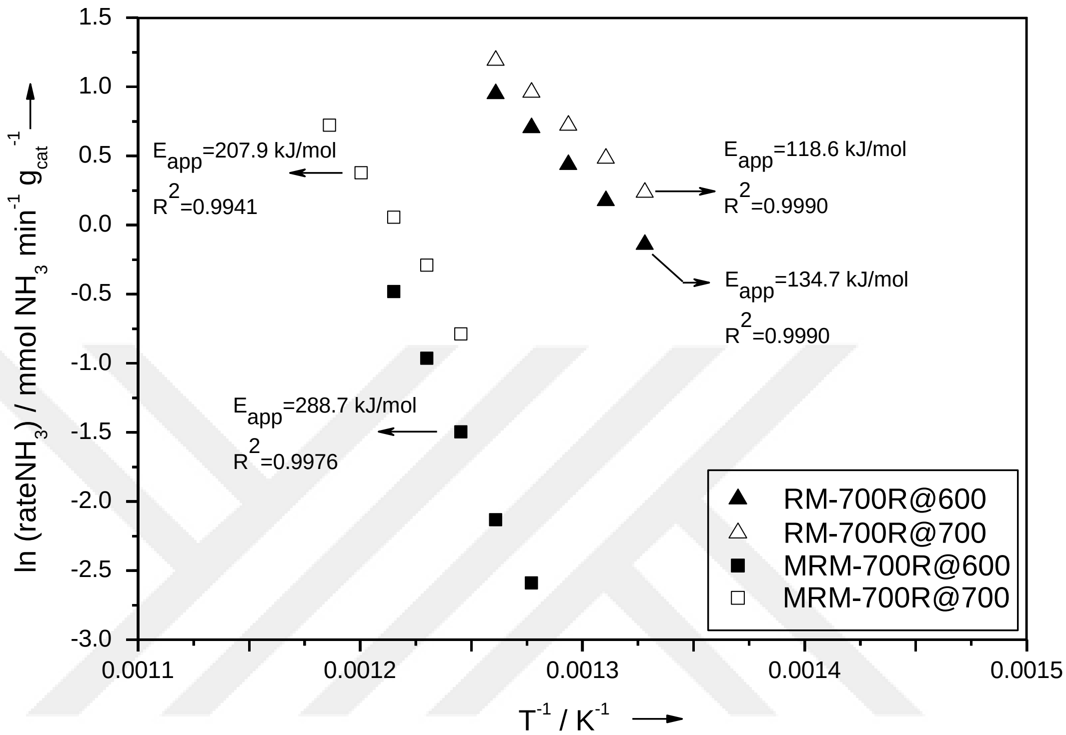

Figure 7.2. Arrhenius plots for RM-700R@600, RM-700R@700, MRM-700R@600, and MRM-700R@700 measured under differential conversions.

In a recent study, we illustrated that the morphology and chemical composition of RM can be tuned by simple acid treatments [30]. For instance, upon 6M HCl digestion at 220 °C (modified RM, MRM), surface area of RM increased from 18 to 232 m^2/g, while Fe_2O_3 content was increasing from 37.2 to 39.8 wt.%. These results were further confirmed by N_2-sorption measurements indicating an at least an order of magnitude higher N_2-sorption capacity on MRM as compared to RM at all pressures (Figure 7.9 and Table 7.2, in section 7.4). For instance, N_2 adsorption capacity of MRM becomes approximately 18 times higher than that of RM at a pressure of 35 bar. SEM images illustrate that MRM still shows the characteristic morphology of RM with much smaller granules present (Figure 7.3 e) and several rigid looking pieces are dispersed in the bulk of MRM not contained in RM (Figure

7.10 a, in section 7.4). These are believed to be the cracked pieces of complex minerals and aluminum oxide particles in RM [31] resulting in a higher surface area. Additional images for comparison of the morphology of RM and MRM are provided in Figure 7.11, in section 7.4. On the other hand, bright field FE-SEM images taken with an STEM detector show that the MRM has a highly porous structure, whereas RM presents large bulky particles (Figure 7.4 and additional images in Figure 7.12, in section 7.4). Other details on chemical composition and textural properties of MRM in comparison with RM are given in supplementary tables, Table 7.1 and 7.2, in in section 7.4.

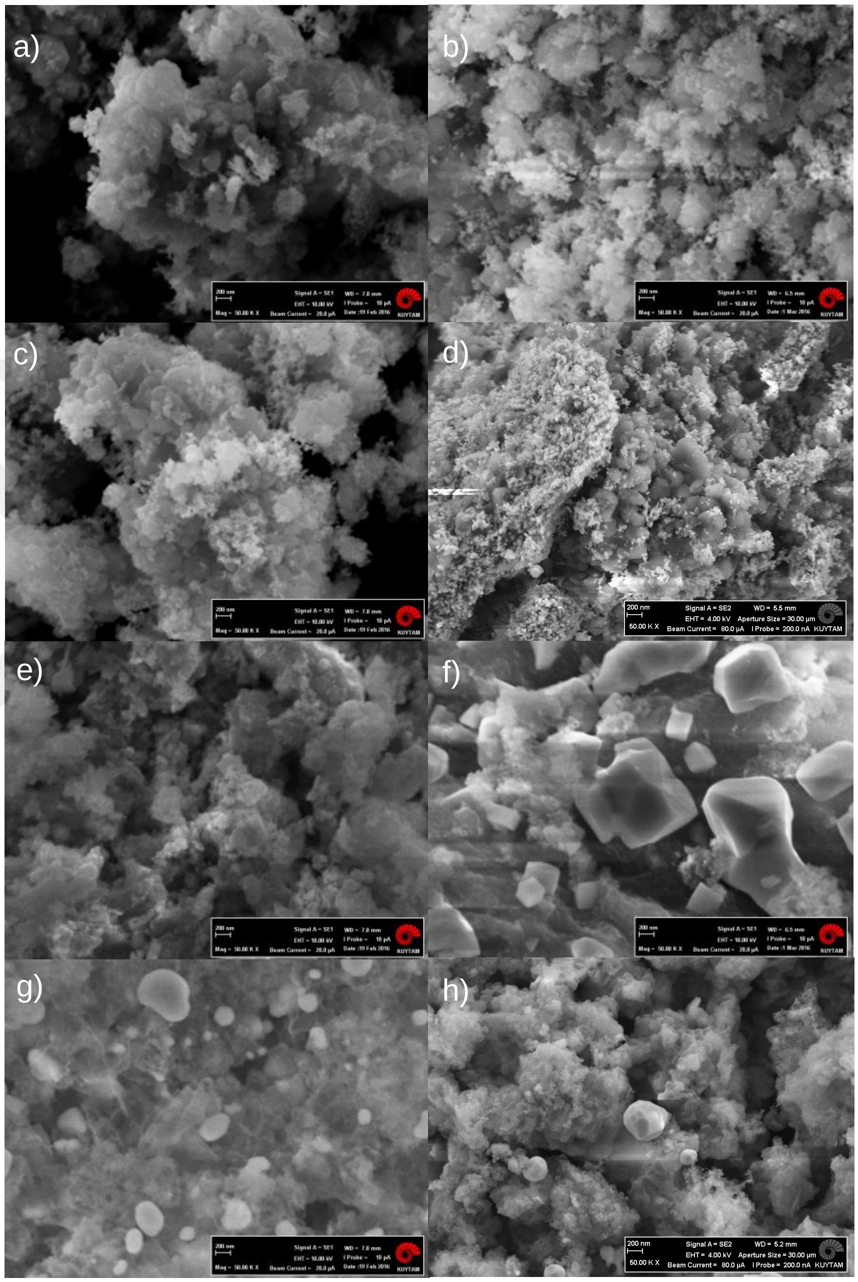

Figure 7.3. SEM images of a) RM, b) RM-700R, c) RM-700R@600, d) RM-700R@700, e) MRM, f) MRM-700R, g) MRM-700R@600, and h) MRM-700R@700.

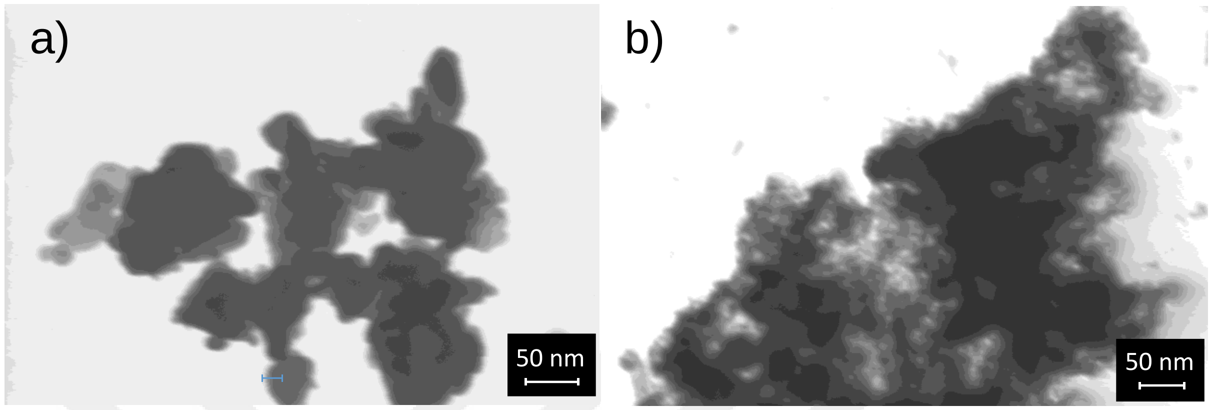

Figure 7.4. Bright field FE-SEM image of a) RM and b) MRM taken with an STEM detector on a FE-SEM.

XRD (Figure 7.1 f) and energy-dispersive X-ray spectroscopy (EDX) results of MRM reduced at 700 °C (MRM-700R, Figure 7.18, in section 7.4) confirm that iron oxide species were converted into metallic iron upon reduction. Although, SEM images indicate that RM-700R appears as similar to RM, MRM-700R shows substantial differences in morphology than MRM with mostly cubical structures present (Figure 7.3 b,f). These structures are well-dispersed with different sizes on the surface of MRM-700R. This substantial difference in the morphologies of the reduced samples suggests a difference in catalytic performance as iron species seem more accessible in the MRM-700R than in the case of RM-700R. Catalytic activity testing of MRM-700R at 500 °C after activating in NH_3 flow at 600 °C for 1 h (MRM-700R@600) indicates that hydrogen production rate on this catalyst was lower than that on RM-700R. The Arrhenius plot (Figure 7.2) obtained under differential conversions indicates an E_{app} of 288.7 kJ/mol. XRD of MRM-700R@600 given in Figure 7.1 g indicates the conversion of metallic iron into Fe_3N_y species (peaks at 37.9, 41.0, and 43.3° indicate a *y* value of 1.22). After activated in NH_3 flow at 700 °C for 10 h (MRM-700R@700), the corresponding E_{app} was measured as 207.9 kJ/mol. This decrease in E_{app} was accompanied by a shift in the XRD peak positions of Fe_3N_y species to 37.5, 40.8, and 42.9°. These peaks at lower 2θ angles correspond to a *y* value of 1.5 in Fe_3N_y (ε-Fe_2N) (Figure 7.1 h). Formation of saturated ε-Fe_2N species indicates that the nitriding process was more complete when the MRM-700R was activated at a higher temperature for a longer time period. The exceptionally high E_{app} values measured on these catalysts suggest that the performance of MRM-700R samples are extremely sensitive to temperature.

As discussed before, non-noble metal catalysts require high temperatures due to the slow recombinative desorption of adsorbed nitrogen atoms, which cannot take place at temperatures lower than 550 °C [32]. Thus, RM-700R and MRM-700R were activated and tested for ammonia decomposition at 700 °C (as RM-700R@700 and MRM-700R@700, respectively). Data given in Figure 7.5 illustrate that ammonia conversion decreased gradually on RM-700R@700 from an initial value of 86.2 to 73.3% within 72 h at a significantly high space velocity of 240 000 cm^3 NH_3 h^{-1} g_{cat}^{-1}. However, under the same conditions, MRM-700R@700 did not show any deactivation and the conversion was remained constant at 80 ± 0.5 % for more than 45 h. Thus, it is inferred that MRM-700R@700 provides a superior performance over RM-700R@700 in terms of stability, although RM-700R@700 can convert slightly higher amount of NH_3 for short time periods as illustrated in Figure 7.5. The corresponding change in H_2 production with space velocity is provided in supplementary Figure 7.21, in section 7.4. To the best of our knowledge, these results presented for MRM-700R@700 in Figure 7.5 and Figure 7.21 are the highest ever reported for a non-noble metal catalyst for stable ammonia decomposition. For instance, Comotti *et al.* [16] reported an iron phthalocyanine-based catalyst providing a constant conversion at approximately 75 % at a space velocity of 60 000 cm^3 NH_3 h^{-1} g_{cat}^{-1}. On MRM-700R@700, a similar conversion can be achieved at almost 5-times of that space velocity, 284 000 cm^3 NH_3 h^{-1} g_{cat}^{-1}. The performance of MRM-700R@700 is even higher than an iron-based core-shell catalysts [33] reported to be stable at 750 °C with a space velocity of 120 000 cm^3 NH_3 h^{-1} g_{cat}^{-1} maintaining a stable ammonia conversion of 80 %. As illustrated in Figure 7.5, MRM-700R@700 provides the same ammonia conversion at a temperature 50 °C lower and at a space velocity twice higher than the corresponding reported values. Furthermore, MRM-700R@700 outperforms Fe_2O_3/CMK-5 known as an iron-based catalyst with the record high performance as well. While Fe_2O_3/CMK-5 [13] was deactivating quickly from an initial conversion of 90 % to less than 60 % within approximately 16 h at a space velocity of 120 000 cm^3 NH_3 h^{-1} g_{cat}^{-1}, MRM-700R@700 maintains 93 ± 0.5 % conversion at the same space velocity. The performance of MRM-700R@700 remains stable for more than 72 h at even a higher conversion of 97 ± 0.5 % for a space velocity of 72 000 cm^3 NH_3 h^{-1} g_{cat}^{-1} (Figure 7.5) at the same temperature. Moreover, even though it is not a proper comparison, the performance of MRM-700R@700 was also compared with the best performing Ru catalysts [6] by extrapolating its temperature dependent performance data to 700 °C. This estimation illustrates that MRM-700R@700 can even provide on par performance with Ru-based catalysts at this high temperature (Figure 7.22, in section 7.4). Although, we note that Ru-based catalyst provides advantages of low temperature operation. Further comparison with literature is provided in Table 7.3, in section 7.4.

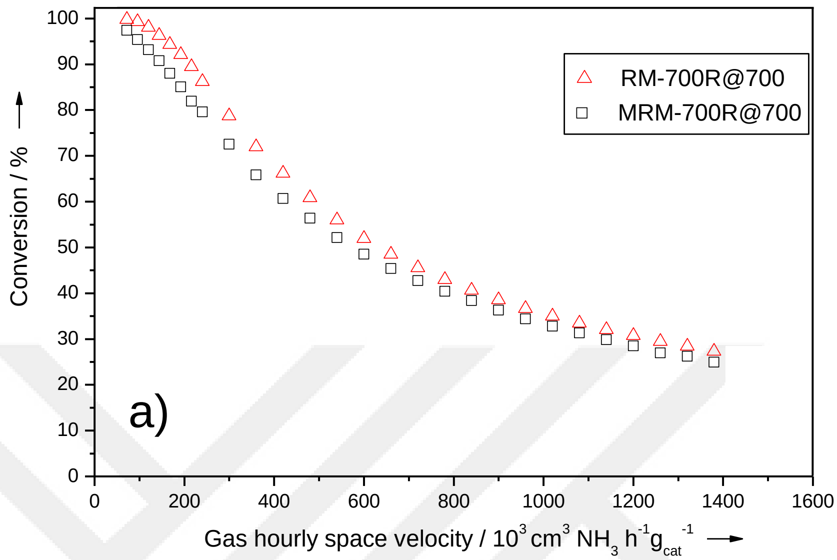

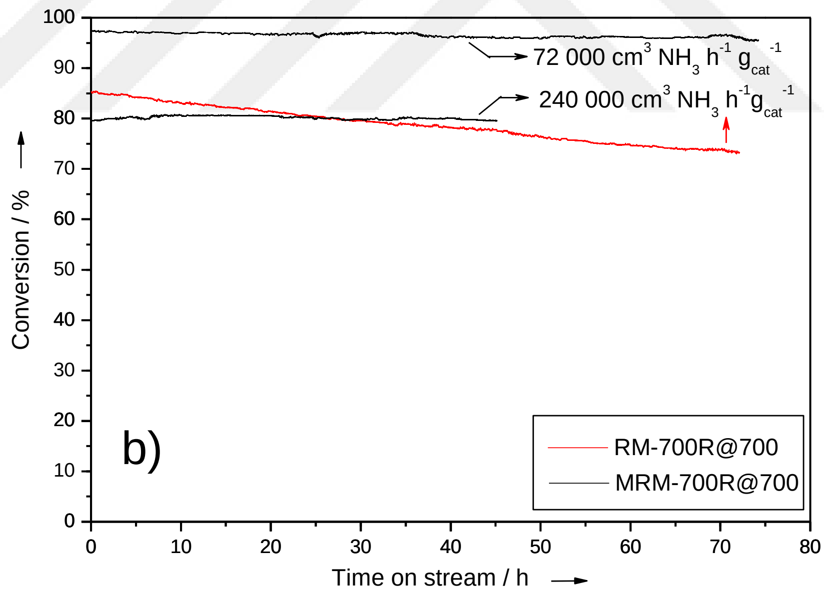

Figure 7.5. a) Catalytic activity of RM-700R@700 and MRM-700R@700 at 700 °C at different space velocities, b) Catalyst stability measurements at high conversions at indicated space velocities for RM-700R@700 (in red) and MRM-700R@700 (in black). Data exclude the induction period of approximately 10 hours (it is given in section 7.4).

Elucidation of the reasons for such high performance is challenging due to the complex nature of RM and MRM. However, as discussed above, XRD of MRM-700R@700 given in Figure 7.1 h show that there is no metallic iron left after the reaction; instead all iron was present in ε-Fe_2N form. Consistent with these results, SEM image given in Figure 7.3 h shows that round-shaped species with varying diameters were newly formed on the surface after reaction. The EDX analysis (Figure 7.20, in section 7.4) performed on these round-shaped species confirms the XRD results and indicates that these round-shaped species are nitrided iron (detailed images are provided in Figure 7.23, in section 7.4). Consistent with this observation Rohith Vinod *et al.* illustrated that nanosized iron clusters can be converted into iron nitride upon ammonia treatment at high temperatures. They also presented similar round-shaped structures by SEM imaging [34]. These results also confirm why the apparent activation energy on MRM-700R was higher than that on RM-700R. Because, as illustrated before [35], totally nitrided iron particles (ε-Fe_2N) require a higher activation energy than a mixture of iron with partially nitrided iron does. Thus, it is inferred that the reduced iron species observed as well-dispersed cubical structures in Figure 7.3 f were converted into ε-Fe_2N during the induction period of 10 h in NH_3 flow at 700 °C (Figure 7.24, in section 7.4). The evidence for this conclusion was the presence of isolated round-shaped particles in the SEM of MRM-700R after reaction (MRM-700R@700 in Figure 7.3 h), also confirmed by EDX and XRD results. It is noted that such ball-like iron nitride species were not observed on the SEM images of RM-700R@700 (Figure 7.3 d) even though its XRD results indicate the presence of $Fe_3N_{1.39}$ in the absence of any metallic iron. These results suggest that iron nitride species formed under the activation conditions are trapped inside the bulk of RM in RM-700R@700. Apparently, a significant increase in surface area caused by the acid digestion makes iron species readily available. Upon activation at 700 °C, they can be converted into ε-Fe_2N in MRM-700R@700. ε-Fe_2N has hexagonal close-packed (hcp) structure with much larger lattice constants than other iron nitrides. Thus, trapped iron species in RM-700R@700 can not be converted into ε-Fe_2N because of space limitations, instead they were partially saturated to form $Fe_3N_{1.39}$. Based on these differences between RM-700R@700 and MRM-700R@700, it is concluded that the readily available ε-Fe_2N species in MRM-700R@700 are directly responsible for stable hydrogen production at such a high rate. It is also noted that metallic iron content of MRM reaches to 35.4 wt.% after reduction at 700 °C. Such high and stable catalytic performance can also be due to the synergistic effect of this high Fe content with the presence of alkali elements, such as Na and K, in trace amounts remained after acid digestion (Table 7.1, in section 7.4). These alkali elements are known for promoting the performance of a non-noble metal catalyst [36]. Their presence in higher amounts in RM-700R@700 might be the reason for higher initial activity on RM-700R@700 as compared to MRM-700R@700. Sintering of these and/or other components present in RM might be blocking the pores under the reaction conditions, making the trapped iron nitride species unavailable for the reaction. This blocking of the pores can be the reason for deactivation observed on RM-700R@700. Whereas MRM-700R@700 does not suffer from this problem as saturated ε-Fe_2N species are readily available on the surface as demonstrated by the SEM images.

7.3 Conclusions

In summary, we show that RM can be simply converted into an exceptionally active and stable catalyst for hydrogen production from ammonia. Results illustrate that MRM converts ammonia into hydrogen and nitrogen at constant conversion for more than 72 h at 700 °C. For instance, stable hydrogen production rates were measured as 72 and 196 mmol H_2 min^{-1} g_{cat}^{-1} for the corresponding space velocities of 72 000 and 240 000 cm^3 NH_3 h^{-1} g_{cat}^{-1}, respectively, at that temperature. These values are significantly higher than the data reported on any other non-noble metal catalysts and on par with the estimated performance of Ru-based catalysts at 700 °C. Characterization of the used MRM catalyst indicated the presence of ε-Fe_2N moieties readily available on the surfaces as the active species for the reaction. Considering that we are utilizing a hazardous industrial waste, being produced in vast amounts, these results provide opportunities towards an eco-friendly, efficient, stable, and almost cost-free catalyst for CO_x-free hydrogen production from ammonia.

References

[1] S.E. Hosseini and M.A. Wahid, Hydrogen production from renewable and sustainable energy resources: Promising green energy carrier for clean development, Renewable and Sustainable Energy Reviews. 57 (2016) 850-866.

[2] W.I.F. David, Effective hydrogen storage: A strategic chemistry challenge, Faraday Discuss. 151 (2011) 399-414.

[3] P. Jena, Materials for hydrogen storage: Past, present, and future, Journal of Physical Chemistry Letters. 2 (2011) 206-211.

[4] W. Zheng, J. Zhang, B. Zhu, R. Blume, Y. Zhang, K. Schlichte, R. Schlögl, F. Schüth, and D.S. Su, Structure–Function Correlations for Ru/CNT in the Catalytic Decomposition of Ammonia, ChemSusChem. 3 (2010) 226-230.

[5] R.Z. Sørensen, A. Klerke, U. Quaade, S. Jensen, O. Hansen, and C.H. Christensen, Promoted Ru on high-surface area graphite for efficient miniaturized production of hydrogen from ammonia, Catal. Lett. 112 (2006) 77-81.

[6] S.J. Wang, S.F. Yin, L. Li, B.Q. Xu, C.F. Ng, and C.T. Au, Investigation on modification of Ru/CNTs catalyst for the generation of COx-free hydrogen from ammonia, Applied Catalysis B: Environmental. 52 (2004) 287-299.

[7] L. Li, Y. Wang, Z.P. Xu, and Z. Zhu, Catalytic ammonia decomposition for CO-free hydrogen generation over Ru/Cr_2O_3 catalysts, Applied Catalysis A: General. 467 (2013) 246-252.

[8] S.-F. Yin, Q.-H. Zhang, B.-Q. Xu, W.-X. Zhu, C.-F. Ng, and C.-T. Au, Investigation on the catalysis of COx-free hydrogen generation from ammonia, J. Catal. 224 (2004) 384-396.

[9] A.K. Hill and L. Torrente-Murciano, Low temperature H_2 production from ammonia using ruthenium-based catalysts: Synergetic effect of promoter and support, Applied Catalysis B: Environmental. 172–173 (2015) 129-135.

[10] L.-F. Zhang, M. Li, T.-Z. Ren, X. Liu, and Z.-Y. Yuan, Ce-modified Ni nanoparticles encapsulated in SiO_2 for CO_x-free hydrogen production via ammonia decomposition, Int. J. Hydrogen Energy. 40 (2015) 2648-2656.

[11] H. Inokawa, T. Ichikawa, and H. Miyaoka, Catalysis of nickel nanoparticles with high thermal stability for ammonia decomposition, Applied Catalysis A: General. 491 (2015) 184-188.

[12] H. Liu, H. Wang, J. Shen, Y. Sun, and Z. Liu, Preparation, characterization and activities of the nano-sized Ni/SBA-15 catalyst for producing COx-free hydrogen from ammonia, Applied Catalysis A: General. 337 (2008) 138-147.

[13] A.H. Lu, J.J. Nitz, M. Comotti, C. Weidenthaler, K. Schlichte, C.W. Lehmann, O. Terasaki, and F. Schüth, Spatially and size selective synthesis of Fe-based nanoparticles on ordered mesoporous supports as highly active and stable catalysts for ammonia decomposition, J. Am. Chem. Soc. 132 (2010) 14152-14162.

[14] Y. Li, L. Yao, S. Liu, J. Zhao, W. Ji, and C.T. Au, Cs-modified iron nanoparticles encapsulated in microporous and mesoporous SiO_2 for COx-free H_2 production via ammonia decomposition, Catal. Today. 160 (2011) 79-86.

[15] X. Duan, G. Qian, X. Zhou, Z. Sui, D. Chen, and W. Yuan, Tuning the size and shape of Fe nanoparticles on carbon nanofibers for catalytic ammonia decomposition, Applied Catalysis B: Environmental. 101 (2011) 189-196.

[16] H. Tüysüz, F. Schüth, L. Zhi, K. Müllen, and M. Comotti, Ammonia decomposition over iron phthalocyanine-based materials, ChemCatChem. 7 (2015) 1453-1459.

[17] F. Schüth, R. Palkovits, R. Schlögl, and D.S. Su, Ammonia as a possible element in an energy infrastructure: Catalysts for ammonia decomposition, Energy and Environmental Science. 5 (2012) 6278-6289.

[18] A.R. Hind, S.K. Bhargava, and S.C. Grocott, The surface chemistry of Bayer process solids: A review, Colloids and Surfaces A: Physicochemical and Engineering Aspects. 146 (1999) 359-374.

[19] S. Xue, F. Zhu, X. Kong, C. Wu, L. Huang, N. Huang, and W. Hartley, A review of the characterization and revegetation of bauxite residues (Red mud), Environmental Science and Pollution Research (2015).

[20] Y. Liu, C. Lin, and Y. Wu, Characterization of red mud derived from a combined Bayer Process and bauxite calcination method, J. Hazard. Mater. 146 (2007) 255-261.

[21] Y. Guo, Y. Zhang, H. Huang, K. Meng, K. Hu, P. Hu, X. Wang, Z. Zhang, and X. Meng, Novel glass ceramic foams materials based on red mud, Ceram. Int. 40 (2014) 6677-6683.

[22] I. Ozer and S. Soyer-Uzun, Relations between the structural characteristics and compressive strength in metakaolin based geopolymers with different molar Si/Al ratios, Ceram. Int. 41 (2015) 10192-10198.

[23] S. Sushil, P. Scholz, K. Pollok, B. Ondruschka, and V.S. Batra, Application of industrial waste based catalysts for total oxidation of propane, Chem. Eng. J. 166 (2011) 568-578.

[24] J.L. Cao, Z.L. Yan, Q.F. Deng, Y. Wang, Z.Y. Yuan, G. Sun, T.K. Jia, X.D. Wang, H. Bala, and Z.Y. Zhang, Mesoporous modified-red-mud supported Ni catalysts for ammonia decomposition to hydrogen, Int. J. Hydrogen Energy. 39 (2014) 5747-5755.

[25] J.L. Cao, Z.L. Yan, Q.F. Deng, Z.Y. Yuan, Y. Wang, G. Sun, X.D. Wang, B. Hari, and Z.Y. Zhang, Homogeneous precipitation method preparation of modified red mud supported Ni mesoporous catalysts for ammonia decomposition, Catalysis Science and Technology. 4 (2014) 361-368.

[26] F.N. Pei, L. Li, S. Wang, Z. Zhu, G. Lu, and Z. Yan, Catalytic ammonia decomposition over industrial-waste-supported Ru catalysts, Environ. Sci. Technol. 41 (2007) 3758-3762.

[27] R.C.C. Costa, F.C.C. Moura, P.E.F. Oliveira, F. Magalhães, J.D. Ardisson, and R.M. Lago, Controlled reduction of red mud waste to produce active systems for environmental applications: Heterogeneous Fenton reaction and reduction of Cr(VI), Chemosphere. 78 (2010) 1116-1120.

[28] Y.Q. Gu, Z. Jin, H. Zhang, R.J. Xu, M.J. Zheng, Y.M. Guo, Q.S. Song, and C.J. Jia, Transition metal nanoparticles dispersed in an alumina matrix as active and stable catalysts for CO_x-free hydrogen production from ammonia, Journal of Materials Chemistry A. 3 (2015) 17172-17180.

[29] W. Arabczyk, J. Zamłynny, and D. Moszyński, Kinetics of nanocrystalline iron nitriding, Polish Journal of Chemical Technology. 12 (2010) 38-43.

[30] Kurtoglu, S.F., Soyer-Uzun, S. & Uzun, A. Tuning Structural Characteristics of Red Mud by Simple Treatments. Under review in *Ceramics International.*

[31] S. Sushil and V.S. Batra, Modification of red mud by acid treatment and its application for CO removal, J. Hazard. Mater. 203-204 (2012) 264-273.

[32] L. Wang, Y. Zhao, C. Liu, W. Gong, and H. Guo, Plasma driven ammonia decomposition on a Fe-catalyst: Eliminating surface nitrogen poisoning, Chem. Commun. 49 (2013) 3787-3789.

[33] M. Feyen, C. Weidenthaler, R. Güttel, K. Schlichte, U. Holle, A.H. Lu, and F. Schüth, High-temperature stable, iron-based core-shell catalysts for ammonia decomposition, Chemistry - A European Journal. 17 (2011) 598-605.

[34] K. Rohith Vinod, P. Saravanan, M. Sakar, V.T.P. Vinod, M. Cernik, and S. Balakumar, Large scale synthesis and formation mechanism of highly magnetic and stable iron nitride (ε-Fe_3N) nanoparticles, RSC Advances. 5 (2015) 56045-56048.

[35] R. Pelka, I. Moszyńska, and W. Arabczyk, Catalytic ammonia decomposition over Fe/Fe4N, Catal. Lett. 128 (2009) 72-76.

[36] K.S. Love and S. Brunauer, The effect of alkali promoter concentration on the decomposition of ammonia over doubly promoted iron catalysts, J. Am. Chem. Soc. 64 (1942) 745-751.

7.4 Additional Characterization Data

7.4.1 TPR Curve of RM

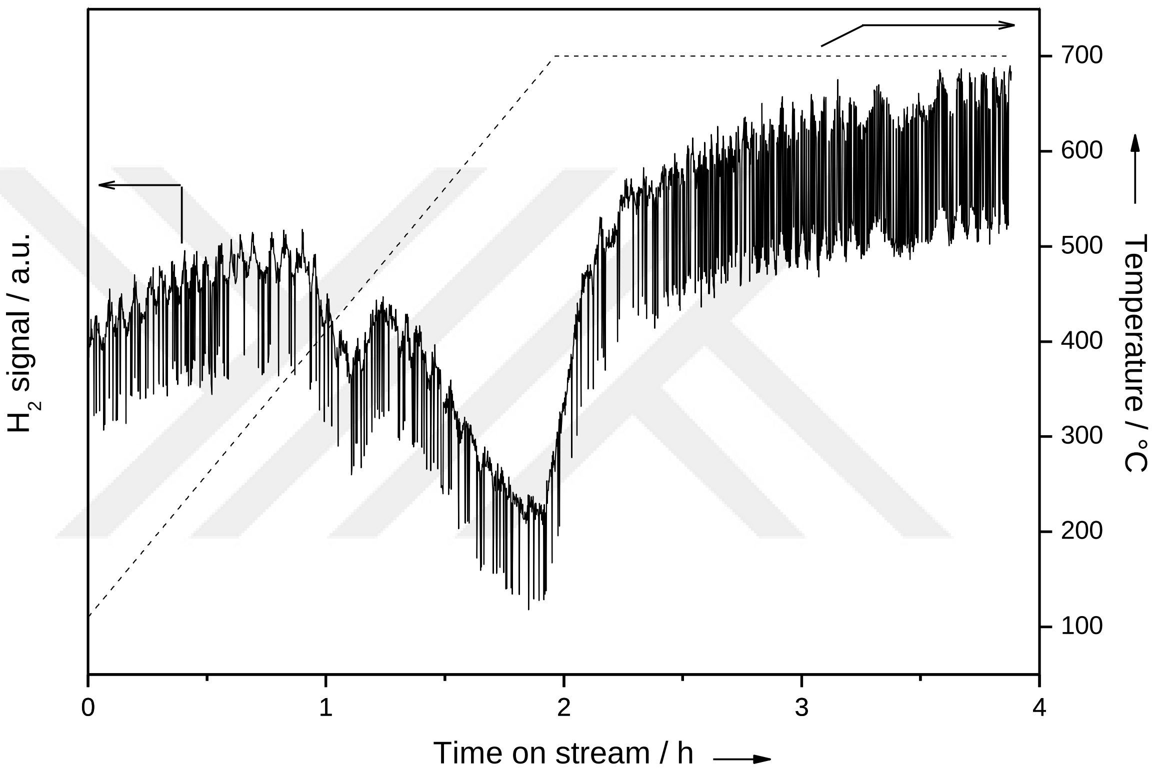

Figure 7. 6. TPR curve of RM.

According to Figure 7.6, there are two main reduction steps. The first one at 442 °C signifies the Fe_3O_4 formation from Fe_2O_3. The second broad peak appearing after 500 °C is related to the FeO formation from Fe_3O_4 and further reduction of FeO to Fe [1] . After 700 °C H_2 signal becomes stable and reduction is completed with the product of metallic iron.

7.4.2 TPR Curve of Fe_2O_3

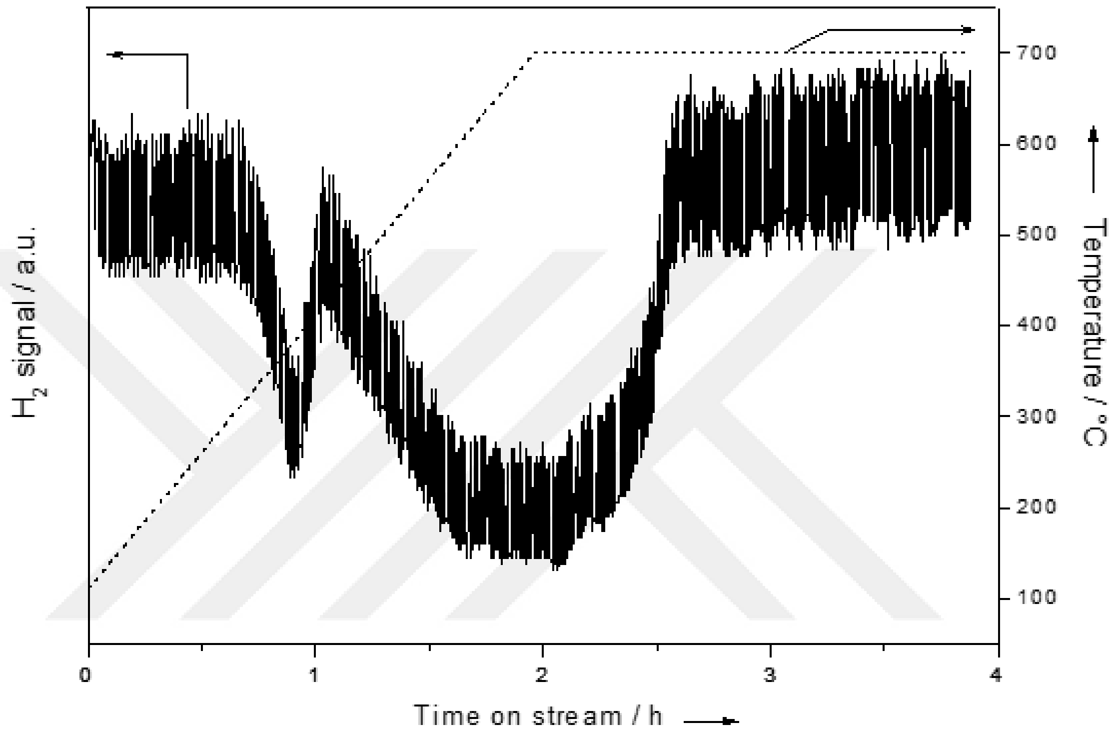

Figure 7.7. TPR curve of pure Fe_2O_3.

According to Figure 7.7, similar to RM, the first peak starting at 388 °C signifies the phase change from Fe_2O_3 to Fe_3O_4 [2]. The second broad peak shows the second reduction step of Fe_3O_4 to Fe, by two different steps as discussed for RM in Figure 7.6.

7.4.3 XRD Pattern for the 2Ө Range 10-90°

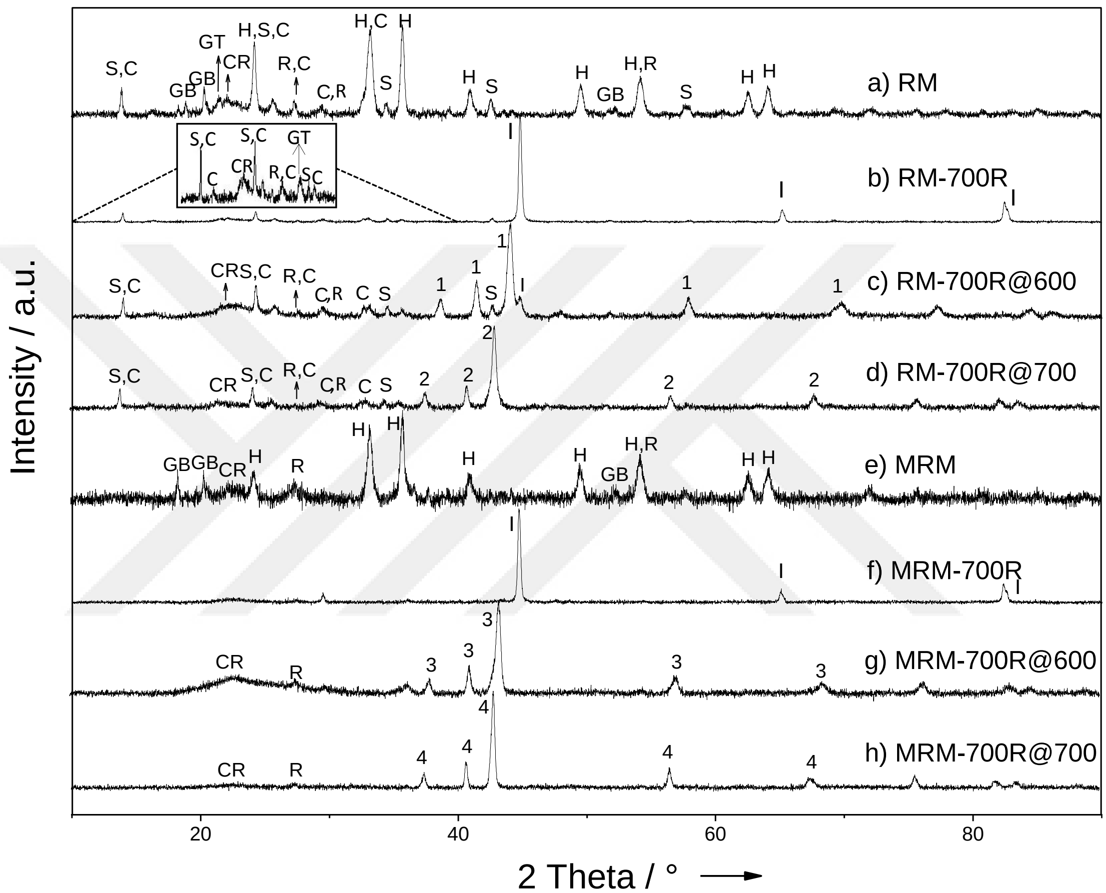

Figure 7.8. XRD pattern of a) RM, b) RM-700R, c) RM-700R@600, d) RM-700R@700, e)MRM, f) MRM-700R, g) MRM-700R@600 and f) MRM-700R@700 H–Hematite (Fe_2O_3), S–Sodalite ($K_{1.4}Na_{5.3}Ca_{1.2}Al_6(SiO_4)_6(CO_3)_{0.3}(SO_4)_{0.8}Cl_{0.9}$), C–Cancrinite ($Na_6(Al_6Si_6O_{24}))(CaCO_3)_2)$, GB–Gibbsite ($Al(OH)_3$), GT–Goethite ($FeO(OH)$), R–Rutile ($TiO_2$), CR–Cristobalite ($SiO_2$), IN–Iron Nitride ($Fe_3N$), I–Iron (Fe), iron nitrides; 1–$Fe_3N_{0.94}$, 2–$Fe_3N_{1.39}$, 3–$Fe_3N_{1.22}$, 4–Fe_2N.

Figure 7.8 a shows the XRD pattern of RM. Several species also confirmed by XRF (Table 7.1) are introduced. In Figure 7.8 e the pattern of MRM does not show the characteristic peak at 13.9° only designating the complex minerals sodalite (PDF 04-011-7226) and cancrinite (PDF 01-074-7052) (labelled by S and C on the figure). After the modifications mainly the following phases left: hematite, rutile, cristobalite, and gibbsite. Due to the decomposition of Na, K, and Ca containing minerals upon acid treatment, the peaks belonging to calcite, cancrinite, and sodalite can not be detected in XRD. The peak of gibbsite is seen clearly at 18.2 and 20.2°. It is inferred that the aluminum phases which were present in sodalite and cancrinite precipitated as aluminum hydroxides during the addition of ammonia to the acid treated slurry. Cristobalite is a phase which does not undergo any phase change during acid treatment. Moreover, the XRF results presented in Table 7.1 further supports this interpretation. Since RM becomes amorphous after modification it is expected that some peaks become less visible than those of hematite because of the presence of intense features of Fe_2O_3. The strong peak at 44.7° (PDF 00-006-0690) of the patterns of RM-700R and MRM-700R given in Figure 7.8 c and f, respectively, shows the conversion of hematite to metallic iron. After reduction of RM-700R, it is possible to detect the phases also present in RM as, sodalite, cancrinite, cristobalite, rutile, and goethite. Because complex minerals like sodalite and cancrinite are decomposed and metallic iron species provide strong features, only metallic iron peak could be detected in MRM-700R (Figure 7.3,f). However, as shown by XRF (Table 7.1) some other species (for example, rutile, cristobalite) are still left after modification.

RM-700R@600 (Figure 7.8 c) shows metallic iron peak at 44.7° together with peaks 38.7, 41.4, and 44.0° corresponding to $Fe_3N_{0.94}$ (PDF-01-077-9851). The iron nitride phase in RM-700R@700 (Figure 7.8 d) is $Fe_3N_{1.39}$ indicated by the main peaks at 37.6, 40.8, and 43.0° (PDF 01-070-7409). $Fe_3N_{1.22}$ in MRM-700R@600C (Figure 7.8, g) is shown by the features at 37.9, 41.0, and 43.3° (PDF 04-011-6419). A further shift of the peak of iron nitride species towards left appears in the sample MRM-700R@700 (Figure 7.8, h) and ε-Fe_2N formation in MRM-700R@700 is indicated by the peaks at 37.5, 40.8, and 42.9° (PDF 04-007-1467).

7.4.4 High Pressure Adsorption Isotherms of RM and MRM

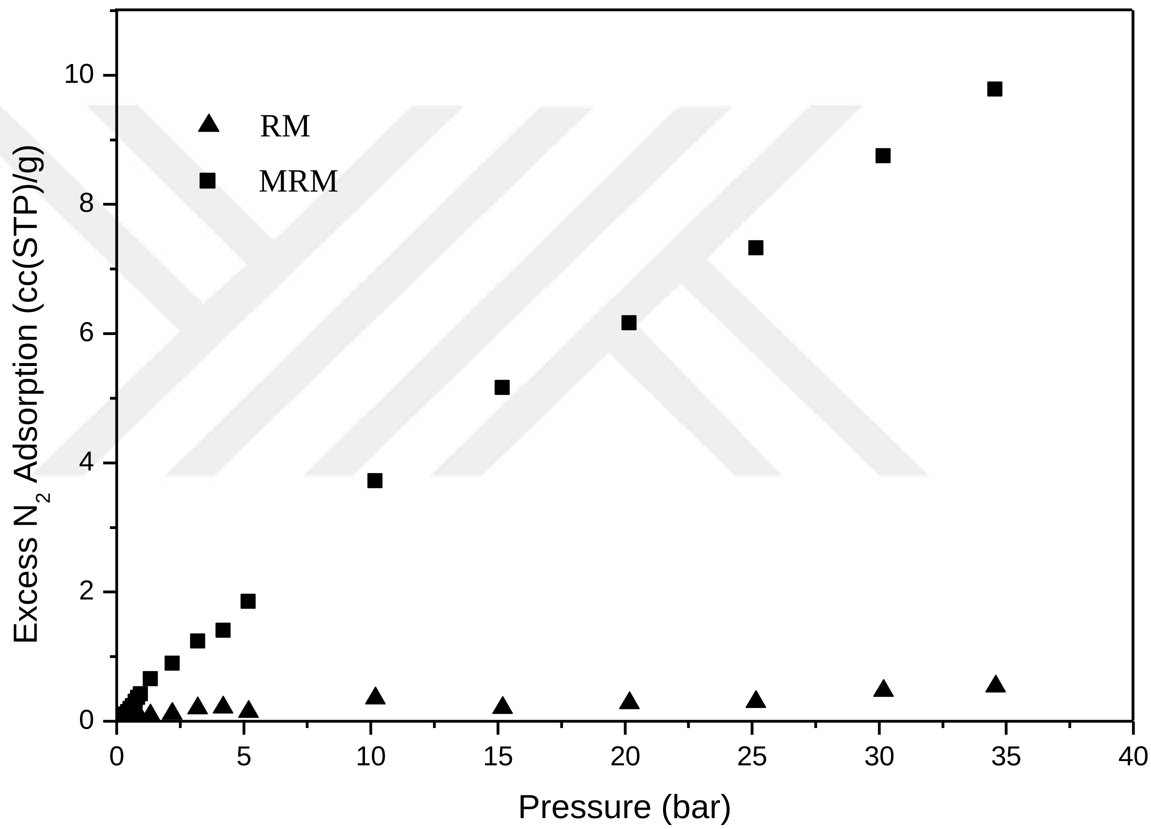

Figure 7.9. N_2 adsorption isotherms for RM and MRM.

Figure 7.9 shows the N_2 sorption analysis of RM and MRM. Further numerical data can be found in Table 7.2.

7.4.5 Additional SEM images of MRM

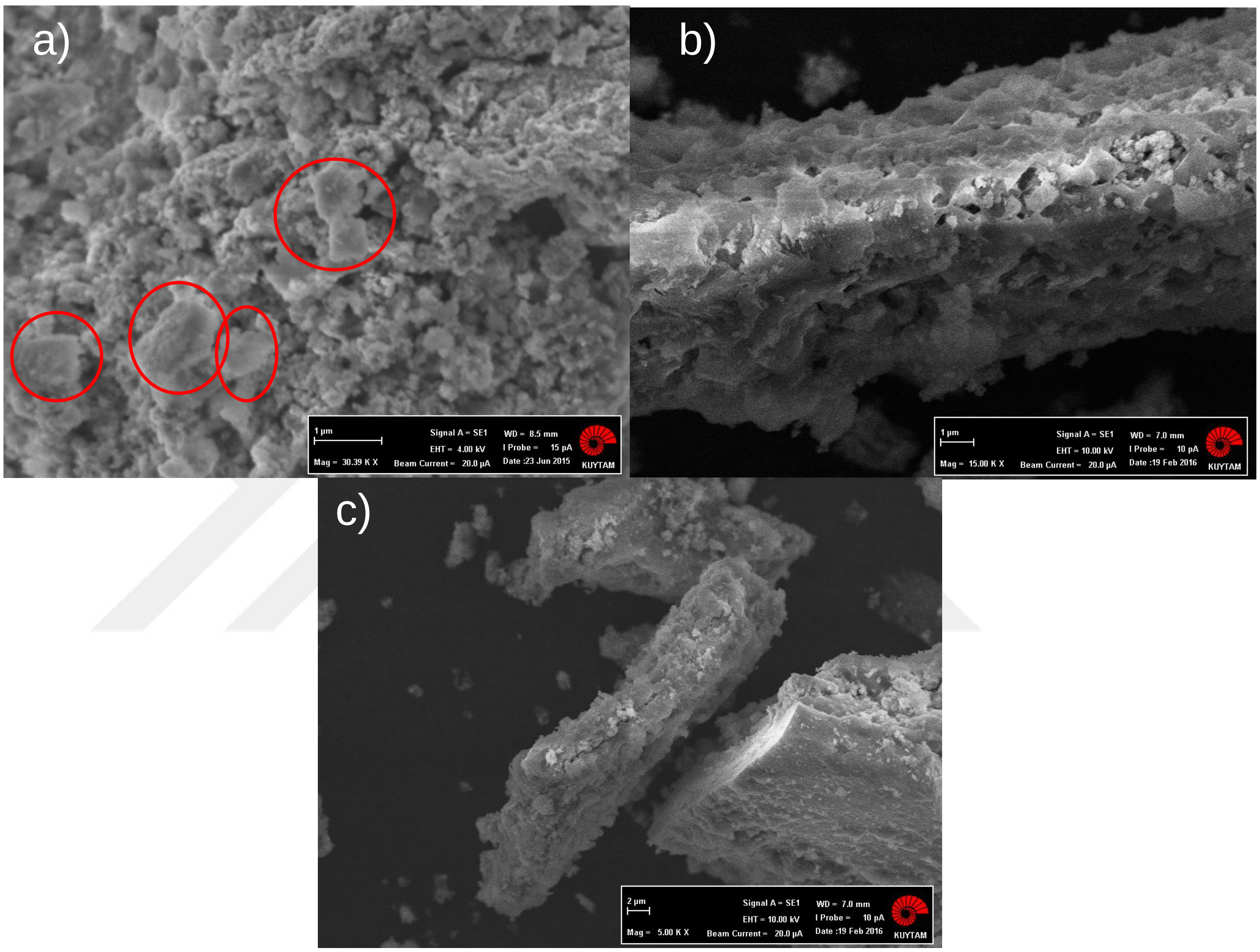

Figure 7.10. Additional SEM image of MRM a) some newly formed particles believed to be dissolution products of decomposed minerals, b) porous structures not present in RM, c) some particles having sharper edges not observed in RM.

Additional SEM images showing different structures upon modification is given in Figure 7.10.

7.4.6 Comparison of RM and MRM in Terms of SEM Images

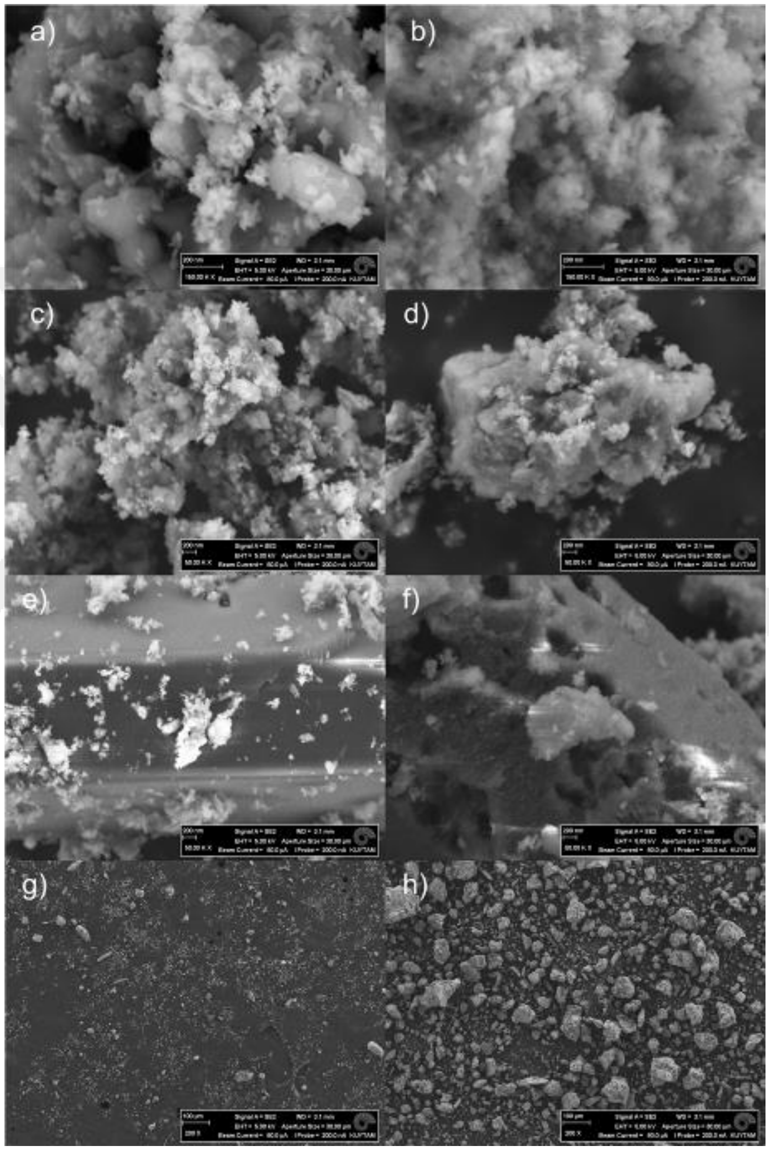

Figure 7. 11. SEM images of a) RM at 150 000× magnification, b) MRM at 150 000× magnification, c) RM at 50 00×, d) MRM at 50 000×, e) RM at 50 000×, f) MRM at 50 000×, g) RM at 200×, and h) MRM at 200×.

As Figure 7.11 a and b suggest, untreated RM has a clear image at 150,000× magnification where the small particle sizes are hardly detected in MRM at the same magnification. These images show that after modification, MRM consists of smaller particles then RM which results in a higher surface area. Several additional images at various magnifications are given in Figure 7.11. When comparing Figure 7.11 e and f one can see that this specie becomes porous after modification. Also it can be noted that, the very low magnification images (Figure 7.11 g an h) shows a very different view between RM and MRM's bulk. MRM consists of more sharp edged rock looking particles.

7.4.7 Comparison of RM and MRM in terms Bright Field FE-SEM Images Taken with STEM Detector

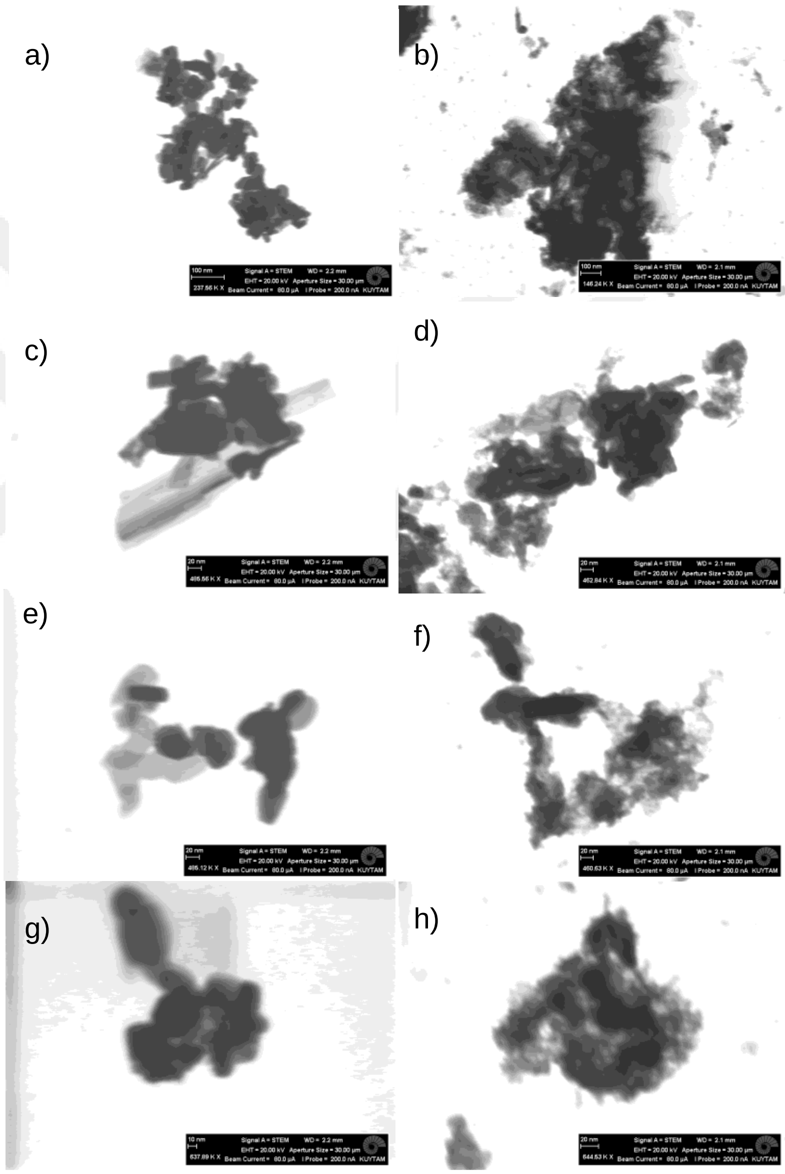

Figure 7.12. Bright field FE-SEM images of RM (a,c,e,g) and MRM (b,d,f,h).

Figure 7.12 supports the findings of SEM images in Figure 7.11, N_2 sorption analysis in Figure 7.9 and BET measurements given in Table 7.2 such that MRM shows a highly porous structure whereas RM appears as bulky particles.

7.4.8 SEM Images and corresponding EDX Spectra

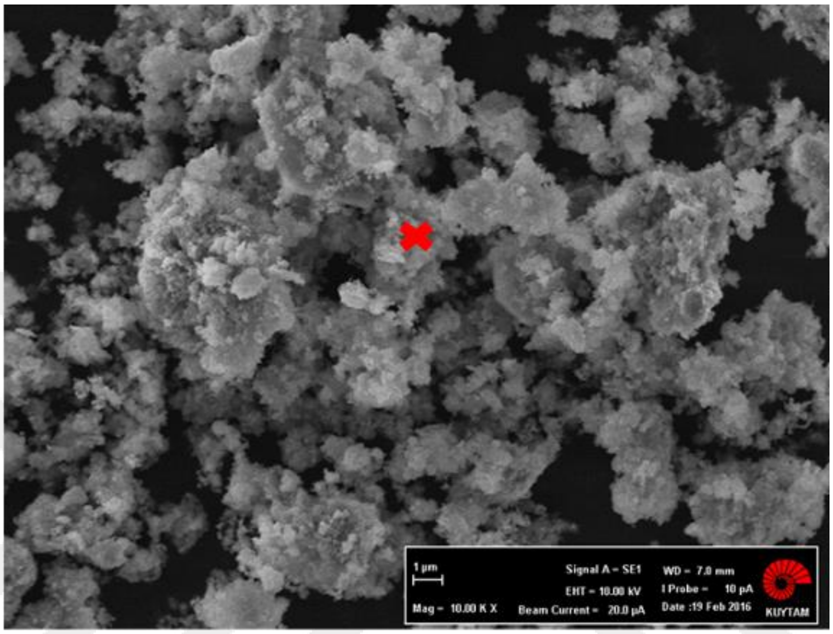

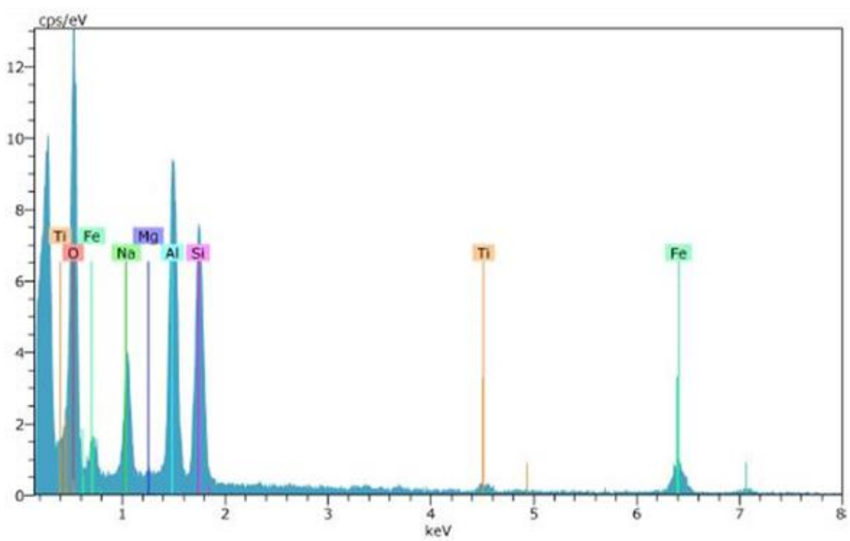

Figure 7.13. SEM image and corresponding EDX spectrum of RM.

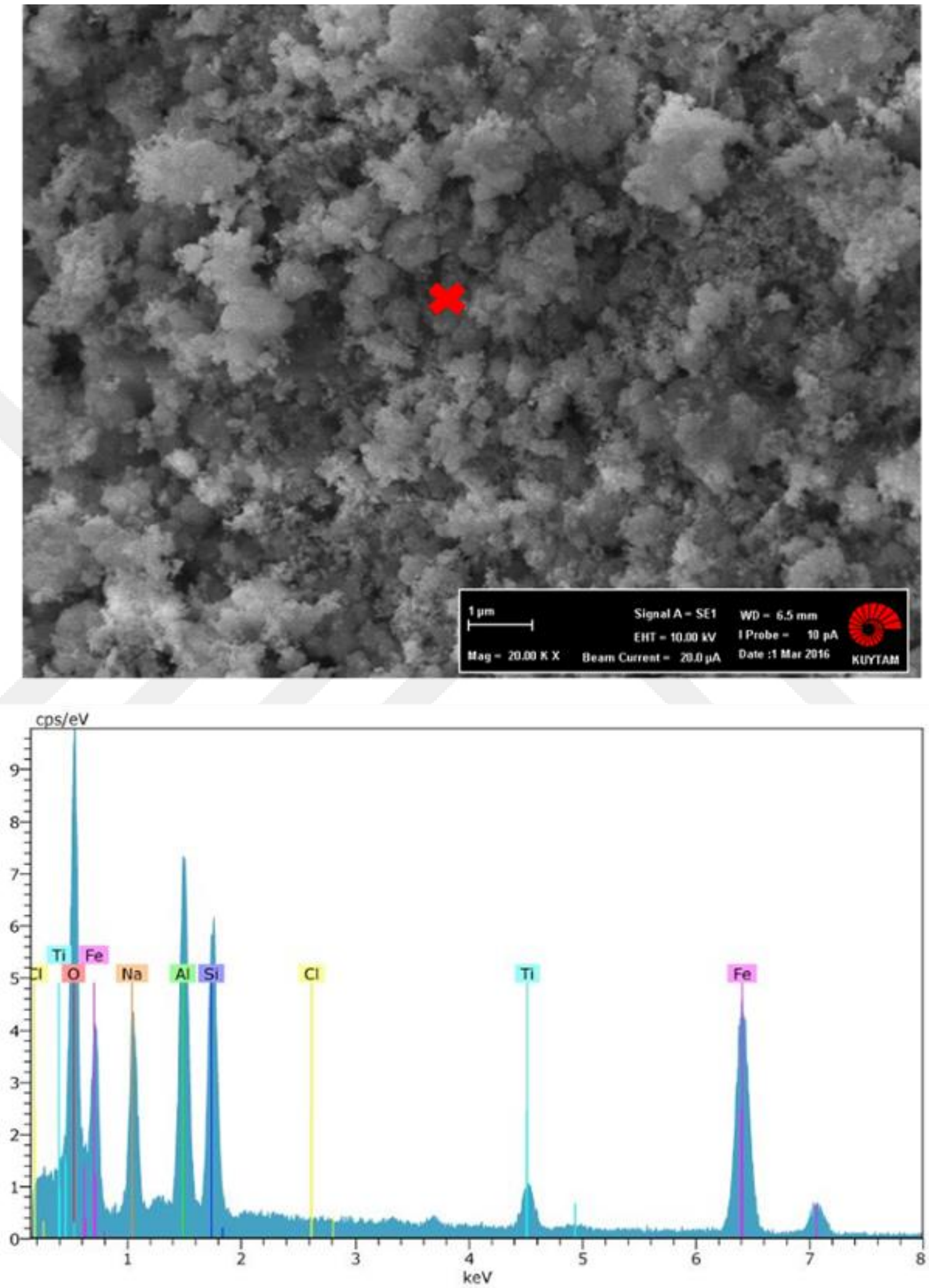

Figure 7.14. SEM image and corresponding EDX spectrum of RM-700R.

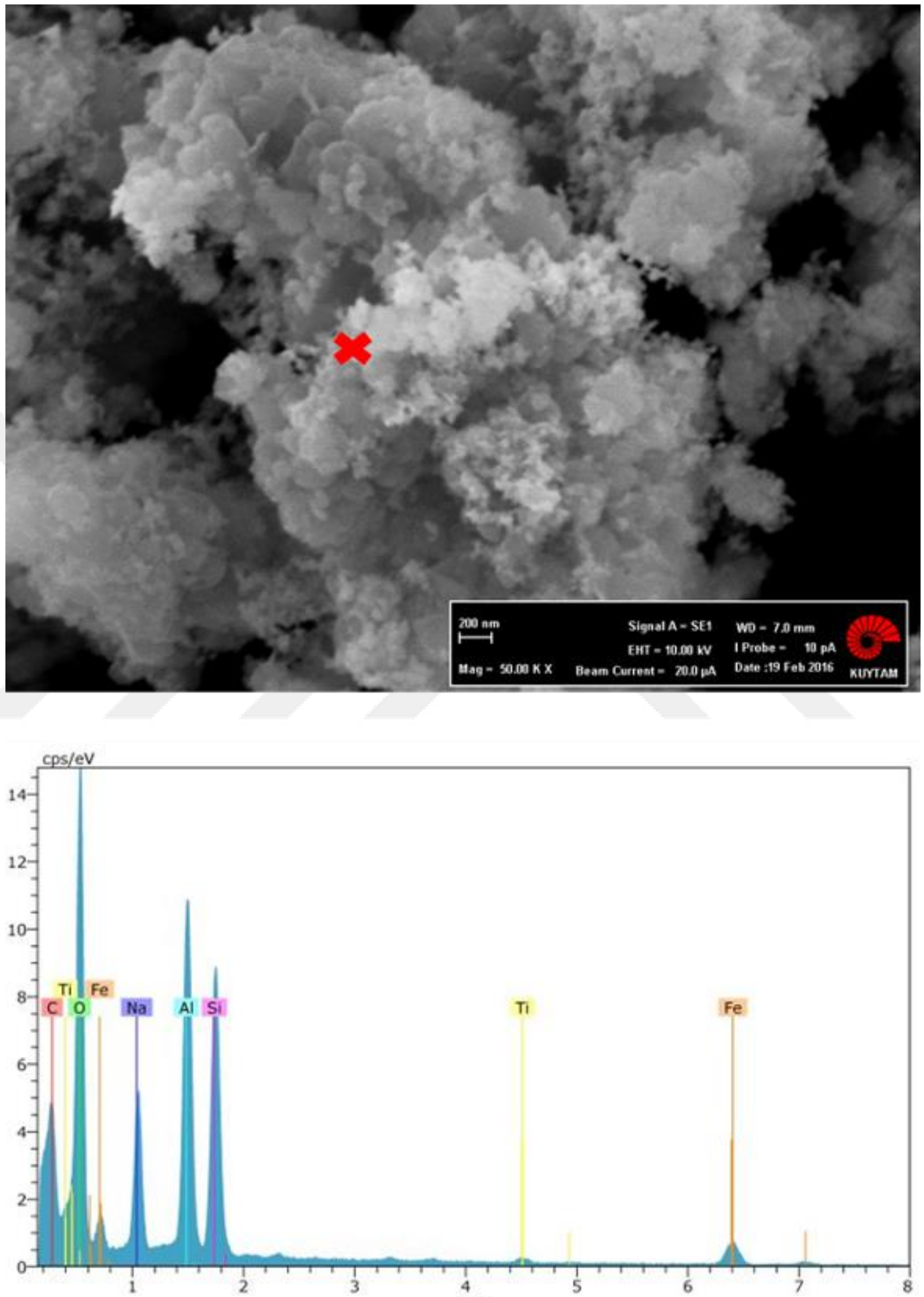

Figure 7.15. SEM image and corresponding EDX spectrum of RM-700R@600.

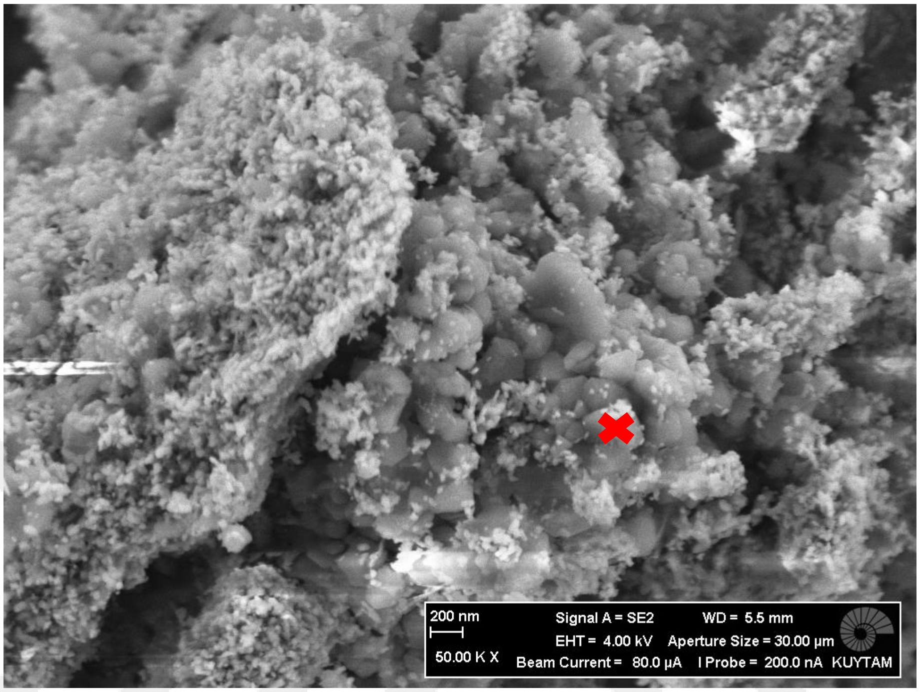

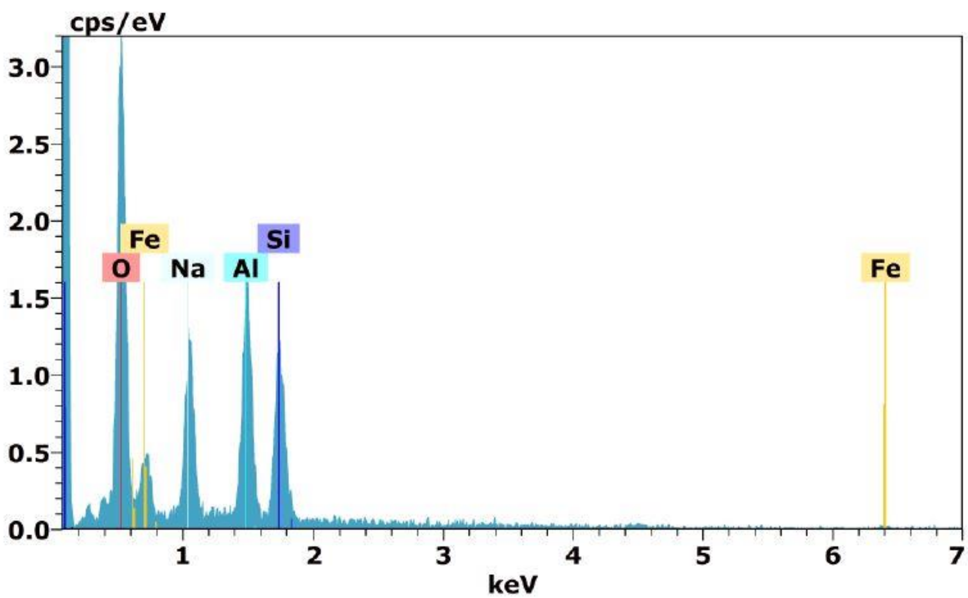

Figure 7.16. SEM image and corresponding EDX spectrum of RM-700R@700.

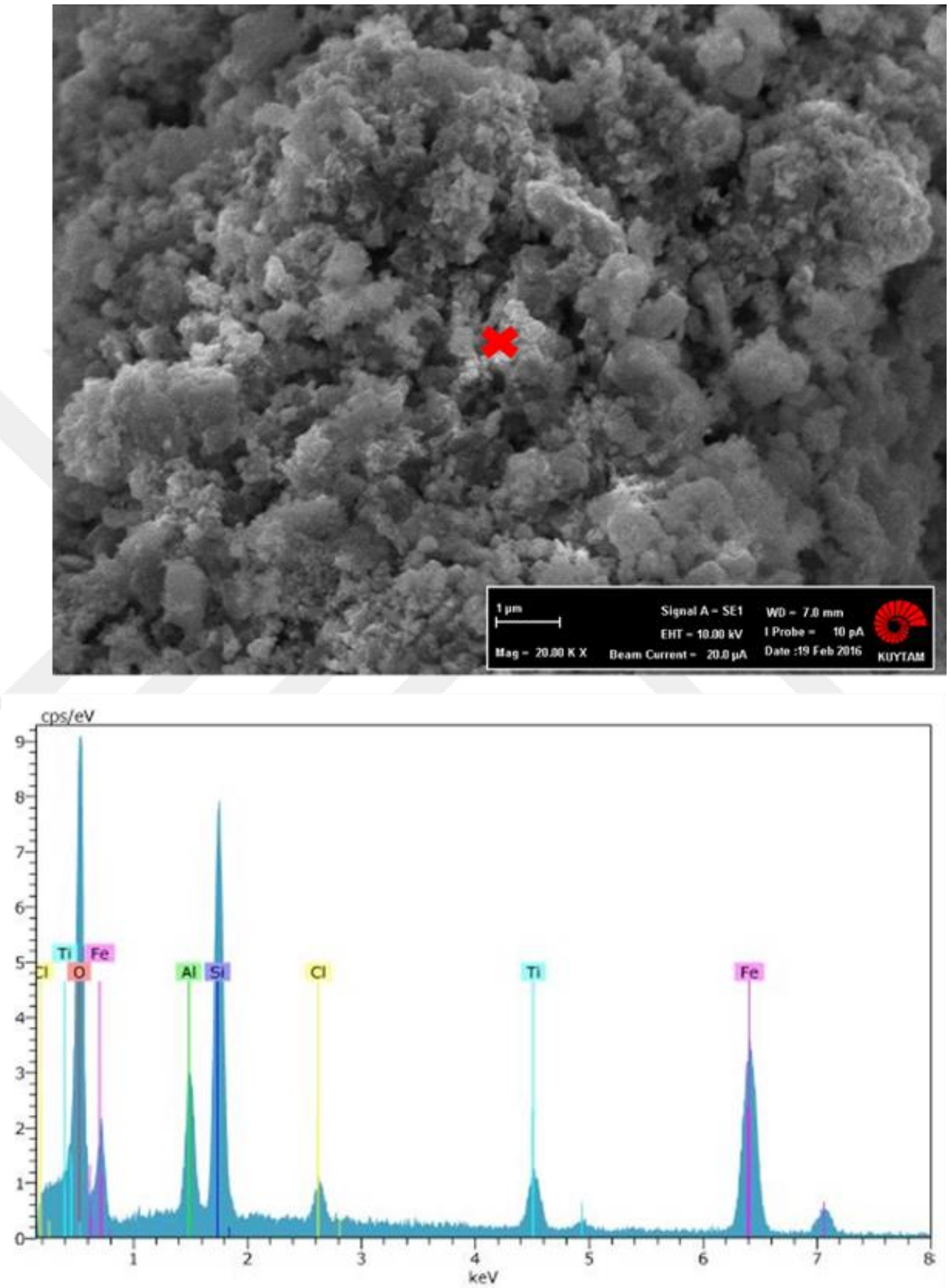

Figure 7.17. SEM image and corresponding EDX spectrum of MRM.

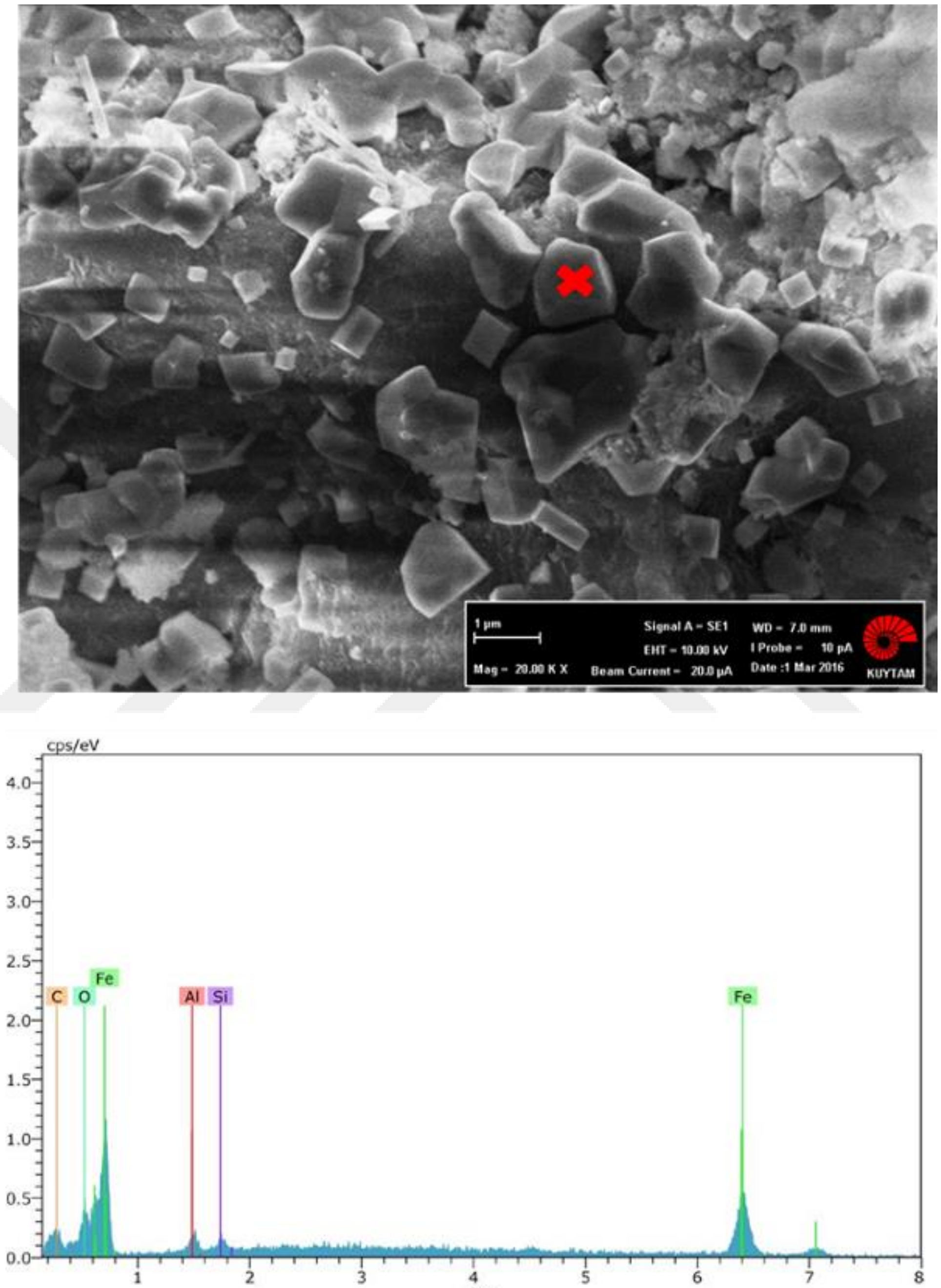

Figure 7.18. SEM image and corresponding EDX spectrum of MRM-700R.

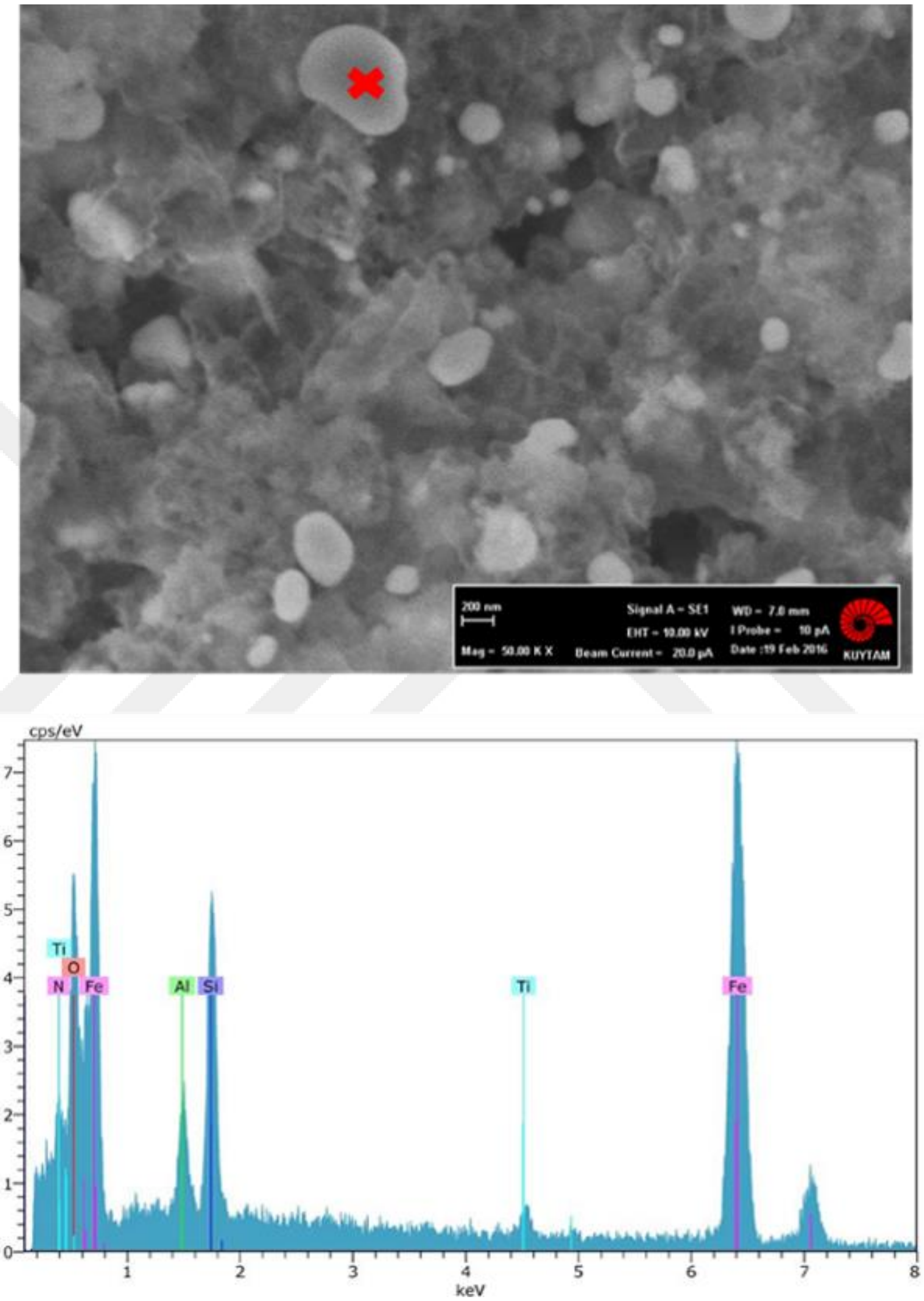

Figure 7.19. SEM image and corresponding EDX spectrum of MRM-700R@600.

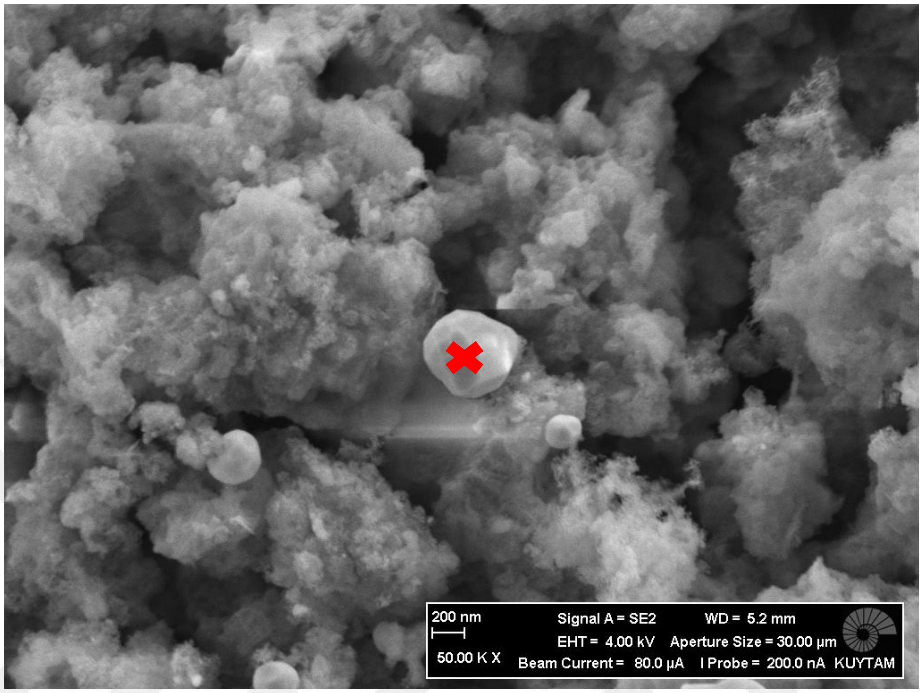

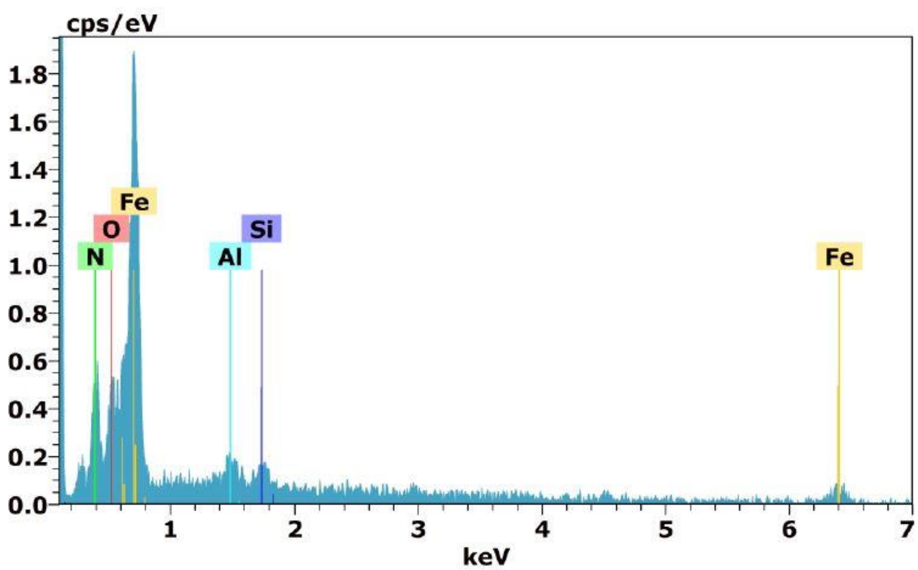

Figure 7.20. SEM image and corresponding EDX spectrum of MRM-700R@700.

In Figure 7.13, the spectrum of RM indicates nearly all components contained in RM which are also detected by XRF shown in Table 7.1. These main elements contained in RM are Fe, Ti, Al, Si, Na, Mg, and O, showing that the oxides of the previous elements are the main phases (also detected by XRD, Figure 7.8 and by XRF, Table 7.1). Figure 7.14, Figure 7.15, and Figure 7.16 are showing the EDX spectrum of RM-700R and RM-700R@600 and RM-700R@700, respectively. These three samples exhibit similar EDX spectra and similar morphology. Even though XRD indicates a complete reduction of iron species in the RM-700R, the cubical species seen in MRM-700R (Figure 7.14) were not observed in SEM images, most probably due to the low surface area of RM-700R. The acid treated RM (MRM) in Figure 7.17 shows a very similar spectrum to RM, however with a more intense peak of Cl which is increasing due to the HCl treatment. We see that in the reduced MRM sample, MRM-700R, no Cl is left when investigating the cubical structure given by a very intense peak of Fe (Figure 7.18). The remaining oxygen peak (very low when compared to the bulk of RM) is due to the oxides of Ti, Al, or Si remaining in MRM-700R. In Figure 7.19, when investigating the spherical structure we see a very intense N peak not present in any other sample proving the presence of N together with the very intense peak of Fe in MRM-700R@600. Similar to MRM-700R-600C, in Figure 7.20, the spherical structure is indicated as iron nitride shown by the very intense N peak in MRM-700R@700.

7.4.9 Activity of MRM-700R given in terms of H_2 Production

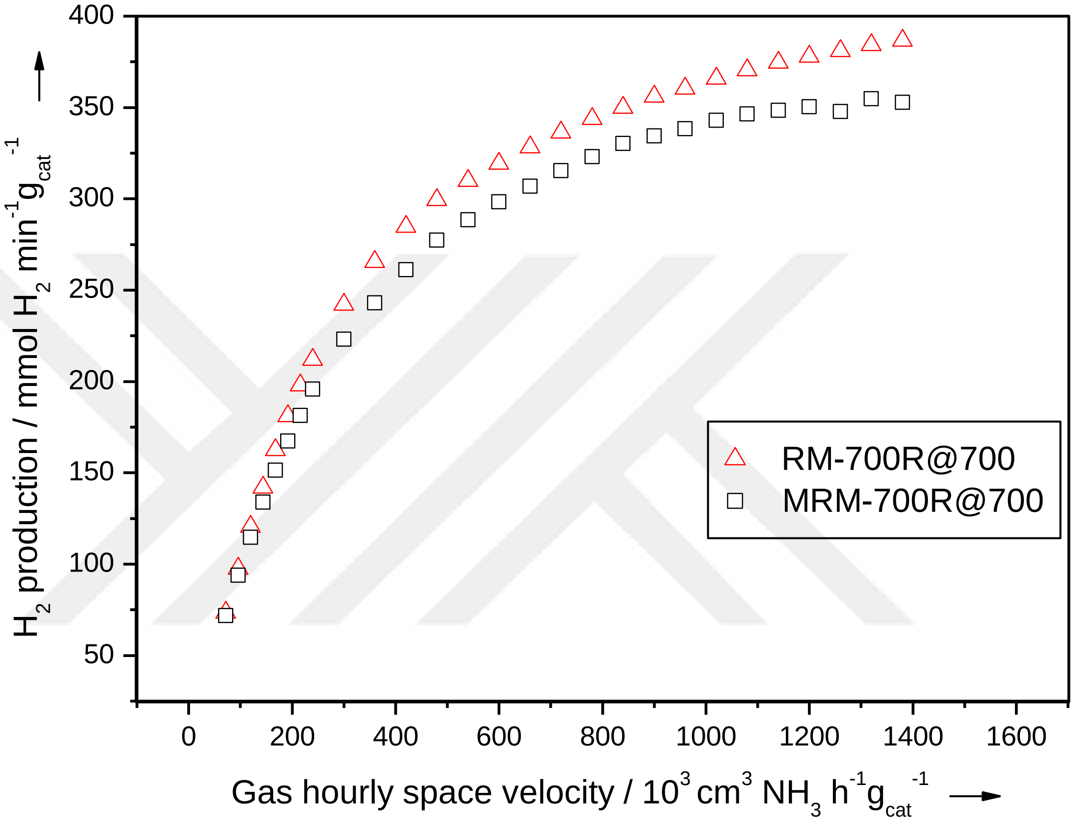

Figure 7.21. Variation of H_2 production rate with space velocity on RM-700R@700 and MRM-700R@700 at 700 °C.

Performance of RM-700R@700 and MRM-700R@700 is illustrated in Figure 7.21 in terms of H_2 production with varying gas hourly space velocity.

7.4.10 Comparison of Ru-based Catalysts with MRM at 700 °C

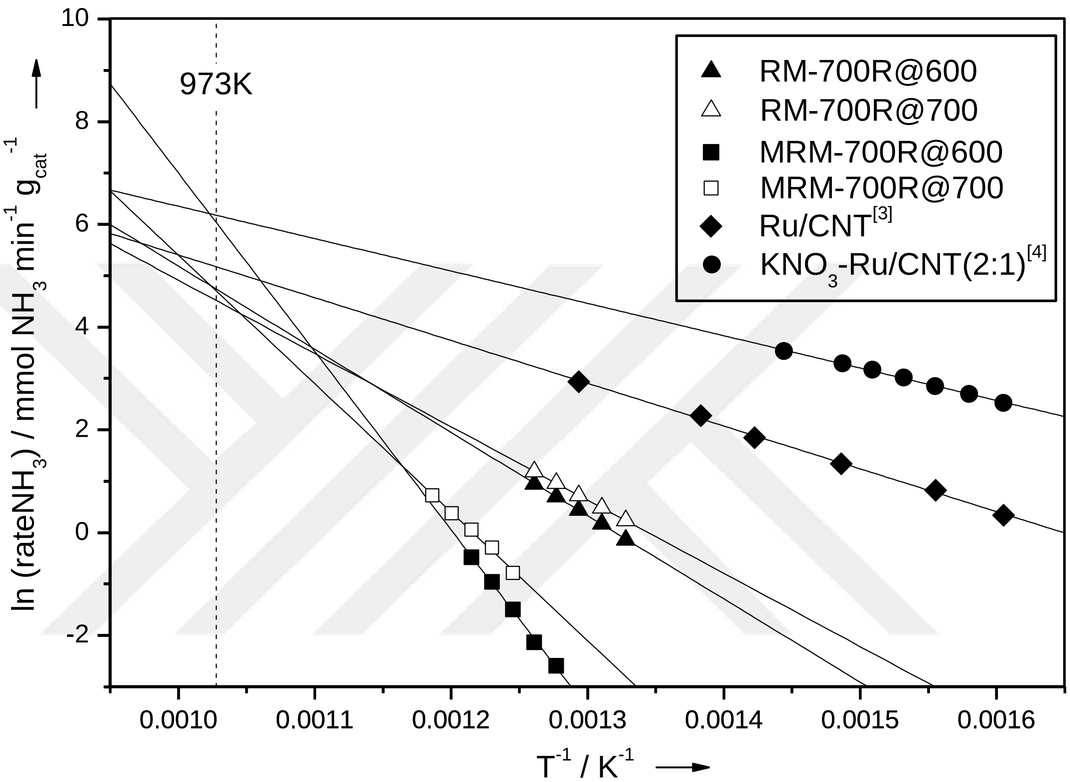

Figure 7.22. Activity comparison by Arrhenius plots in comparison with Ru/CNT [3], and KNO_3-Ru/CNT(2:1) [4]. It is noted that these values were obtained under differential conversion conditions, thus estimation to higher temperature is only valid under similar low NH_3 conversions.

In Figure 7.22 the activity of RM and MRM-700R@700 is compared with that of the best performing Ru-based catalysts, Ru/CNT,[3] and KNO_3 modified Ru/CNT catalyst[4] with a K/Ru atomic ratio of 2. We note that this graph provides a rough comparison between the literature data on best performing Ru-based catalysts and MRM-700R@700. The space velocity of MRM-700R@700 for obtaining the Arrhenius plot at differential conversions was

57 775 cm^3 NH_3 h^{-1} g_{cat}^{-1}. Space velocity for Arrhenius plot measurement of Ru/CNT and KNO_3-Ru/CNT(2:1) catalysts were 30 000 and 60 000 cm^3 NH_3 h^{-1} g_{cat}^{-1}, respectively. The dashed line is showing the location corresponding to the reverse of 700 °C (1/973 K). This rough estimation illustrates that MRM-700R@700 provides on par performance with the Ru-based catalyst at 700 °C. This difference in performance might be because of the higher apparent activation energy observed on MRM-700R@700, which provides higher performance at high temperature. It is noted that this estimation is only valid for differential conversion conditions, at which the Arrhenius plots were obtained.

7.4.11 Additional SEM images of MRM-700@600 and FE-SEM images of MRM-700R@700

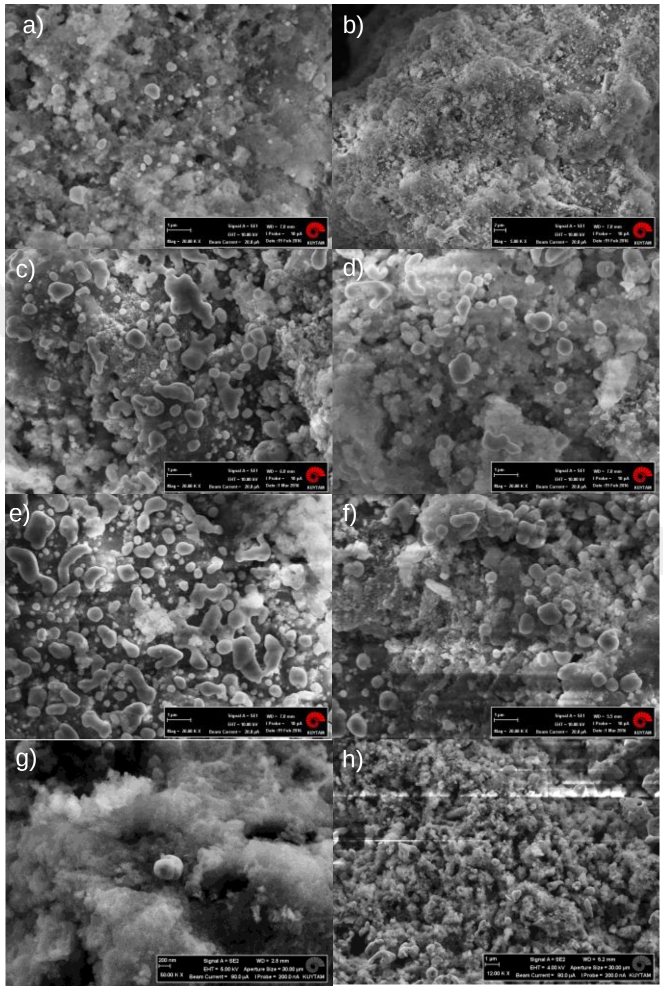

Figure 7.23. Additional SEM images of MRM-700R@600 at magnifications of 5 000× (in b), 20 000× (in a,c,d,e, and f) and additional FE-SEM images of MRM-700R@700 at magnifications of 50 000× (in g), 12 000× (in h) showing the dispersed iron nitride particles in different locations.

Additional images of MRM-700@600 are illustrated in Figure 7.23.

7.4.12 Induction Period for MRM-700R and RM-700R

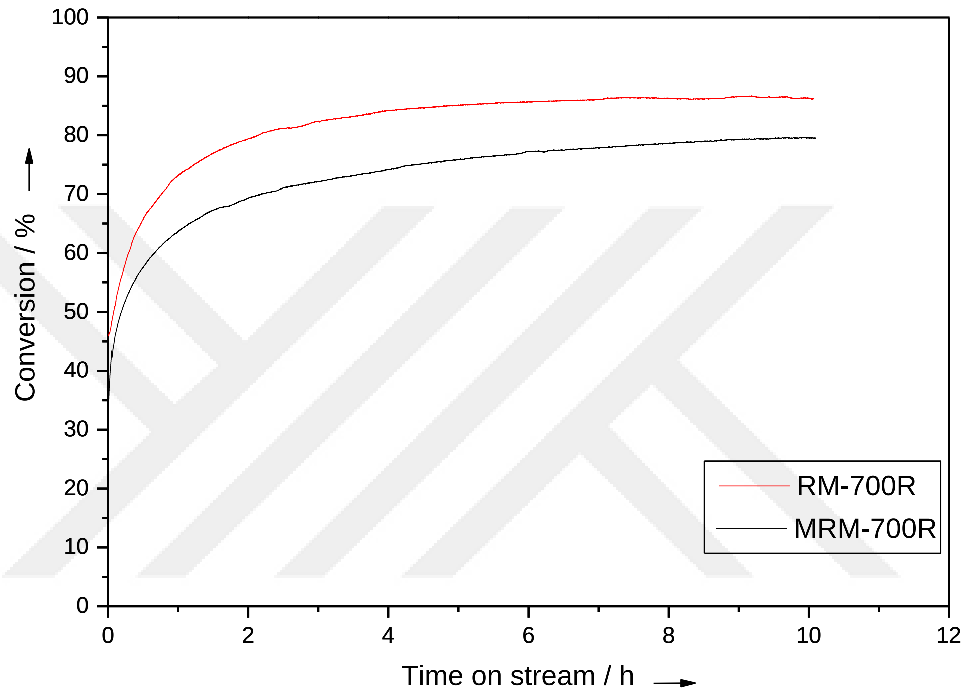

Figure 7.24. Induction period of RM-700R (in red) and MRM-700R (in black) at a constant space velocity of GHSV of 240 000 cm^3 NH_3 h^{-1} g_{cat}^{-1} at 700°C. Initial point, t = 0 h, indicates the time at which the ammonia flow was started.

According to Figure 7.24 the induction period is completed after approximately 10 h at 700 °C for RM-700R and MRM-700R. The resulting samples obtained at the end of this induction period were denoted as RM-700R@700 and MRM-700R@700, respectively. After the completion of this period, long-term H_2 production measurements were performed.

7.4.13 Comparison of activity with literature focusing on non-noble metal catalysts

Table 7.1. Chemical composition of RM, RM-700R, MRM and MRM-700R.

	Composition of chemicals (wt.%)											
Sample	Fe_2O_3	Fe	Al_2O_3	Si_2O	Na_2O	TiO_2	CaO	K_2O	SO_3	ZrO_2	CeO_2	Cl
RM	37.2	-	14.0	11.3	9.3	5.9	1.1	0.30	0.2	0.2	0.1	0.02
RM-700R	-	29.7	16.6	13.5	11.0	6.5	1.3	0.34	0.2	0.2	0.1	0.03
MRM	39.8	-	12.9	10.2	0.2	6.2	0.2	0.02	0.2	0.2	0.1	5.5
MRM-700R	-	35.4	17.8	17.2	0.4	8.0	0.2	0.02	0.1	0.2	0.2	0.3

Table 7. 2. Surface area, pore volume, pore size and N_2 adsorption capacity of RM and MRM at various pressures.

Sample	Surface area ($m^2\ g^{-1}$)	Pore volume ($cm^3\ g^{-1}$)	Pore size (nm)	Average nanoparticle size (nm)	Excess N_2 Adsorbed at 5 bar (cc(STP)/g)	Excess N_2 Adsorbed at 20 bar (cc(STP)/g)	Excess N_2 Adsorbed at 35 bar (cc(STP)/g)
RM	17.9	0.035	11.1	335.6	0.15	0.28	0.54
MRM	232.4	0.17	5.3	25.8	1.85	6.17	9.78

Table 7.3. Comparison of activity with literature.

Catalyst	Temperature / °C	Conversion / %	GHSV / $cm^3\ h^{-1}\ g_{cat}^{-1}$	Hydrogen production rate / mmol $min^{-1}\ g_{cat}^{-1}$	Reference
RM-700R@600	500	5.1	42 250	2.3	This study
RM-700R@700	500	6.8	44 118	3.1	This study
RM-700R@700	700	99.8	72 000	73.6	This study
RM-700R@700	700	86.2[a]	240 000	212.0	This study
MRM-700R@600	500	0.1	60 000	0.05	This study
MRM-700R@700	500	0.1	40 000	0.03	This study
MRM-700R@700	700	97.4	72 000	71.9	This study
MRM-700R@700	700	93.2	120 000	114.5	This study
MRM-700R@700	700	79.6	240 000	195.7	This study
C-Fe-2.33-400	700	90[a]	120 000	110.4	[5]
C-Fe-2.33-400	700	100[a]	60 000	61.3	[5]
Fe^{III}-Pc-800A-1	700	74.8	60 000	46.1	[6]
Fe-CNFs/CMFs-5	650	100	2 700	2.8	[7]

Fe-CNFs/mica	600	98.9	6 500	6.6	[8]
Fe_3O_4@CeO_2	600	89	24 000	21.8	[9]
α-Fe_2O_3-50@pSiO_2	750	80	120 000	98.1	[10]
Fe@meso-SiO_2-Cs (0.2)	650	100	30 000	33.5	[11]
90FeAl	600	100	18 000	18.3	[12]
K-Ni/MCM-41(TIE)	700	100	30 000	33.5	[13]
Nano-Ni@SiO_2(Si/Ni=0.4)	650	98.6	30 000	33.0	[14]
Ni/LA_2O_3 (40%Ni)	550	78.9	6 000	4.9	[15]
La-modified Ni/Al_2O_3 calcined at 500°C	600	100	6 000	6.2	[16]
La-modified Ni/Al_2O_3 calcined at 400°C reduced at 600°C	700	100	10 000	10.3	[16]
Co/MWCNTs	500	60	6000	3.7	[17]

[a] not stable, deactivates

References

[1] R.C.C. Costa, F.C.C. Moura, P.E.F. Oliveira, F. Magalhães, J.D. Ardisson, and R.M. Lago, Controed reduction of red mud waste to produce active systems for environmental applications: Heterogeneous Fenton reaction and reduction of Cr(VI), Chemosphere. 78 (2010) 1116-1120.

[2] H.Y. Lin, Y.W. Chen, and C. Li, The mechanism of reduction of iron oxide by hydrogen, Thermochim. Acta. 400 (2003) 61-67.

[3] S.-F. Yin, Q.-H. Zhang, B.-Q. Xu, W.-X. Zhu, C.-F. Ng, and C.-T. Au, Investigation on the catalysis of COx-free hydrogen generation from ammonia, J. Catal. 224 (2004) 384-396.

[4] S.J. Wang, S.F. Yin, L. Li, B.Q. Xu, C.F. Ng, and C.T. Au, Investigation on modification of Ru/CNTs catalyst for the generation of CO_x-free hydrogen from ammonia, Applied Catalysis B: Environmental. 52 (2004) 287-299.

[5] A.H. Lu, J.J. Nitz, M. Comotti, C. Weidenthaler, K. Schlichte, C.W. Lehmann, O. Terasaki, and F. Schüth, Spatially and size selective synthesis of Fe-based nanoparticles on ordered mesoporous supports as highly active and stable catalysts for ammonia decomposition, J. Am. Chem. Soc. 132 (2010) 14152-14162.

[6] H. Tüysüz, F. Schüth, L. Zhi, K. Müllen, and M. Comotti, Ammonia decomposition over iron phthalocyanine-based materials, ChemCatChem. 7 (2015) 1453-1459.

[7] J. Ji, X. Duan, G. Qian, P. Li, X. Zhou, D. Chen, and W. Yuan, Fe particles on the tops of carbon nanofibers immobilized on structured carbon microfibers for ammonia decomposition, Catal. Today. 216 (2013) 254-260.

[8] X. Duan, G. Qian, X. Zhou, Z. Sui, D. Chen, and W. Yuan, Tuning the size and shape of Fe nanoparticles on carbon nanofibers for catalytic ammonia decomposition, Applied Catalysis B: Environmental. 101 (2011) 189-196.

[9] H.Z. Cui, Y.Q. Gu, X.X. He, S. Wei, Z. Jin, C.J. Jia, and Q.S. Song, Iron-based composite nanostructure catalysts used to produce CO_x-free hydrogen from ammonia, Science Bulletin (2016) 1-7.

[10] M. Feyen, C. Weidenthaler, R. Güttel, K. Schlichte, U. Holle, A.H. Lu, and F. Schüth, High-temperature stable, iron-based core-shell catalysts for ammonia decomposition, Chemistry - A European Journal. 17 (2011) 598-605.

[11] Y. Li, L. Yao, S. Liu, J. Zhao, W. Ji, and C.T. Au, Cs-modified iron nanoparticles encapsulated in microporous and mesoporous SiO_2 for CO_x-free H_2 production via ammonia decomposition, Catal. Today. 160 (2011) 79-86.

[12] Y.Q. Gu, Z. Jin, H. Zhang, R.J. Xu, M.J. Zheng, Y.M. Guo, Q.S. Song, and C.J. Jia, Transition metal nanoparticles dispersed in an alumina matrix as active and stable catalysts for CO_x-free hydrogen production from ammonia, Journal of Materials Chemistry A. 3 (2015) 17172-17180.

[13] X.K. Li, W.J. Ji, J. Zhao, S.J. Wang, and C.T. Au, Ammonia decomposition over Ru and Ni catalysts supported on fumed SiO_2, MCM-41, and SBA-15, J. Catal. 236 (2005) 181-189.

[14] L. Yao, T. Shi, Y. Li, J. Zhao, W. Ji, and C.T. Au, Core-shell structured nickel and ruthenium nanoparticles: Very active and stable catalysts for the generation of CO_x-free hydrogen via ammonia decomposition, Catal. Today. 164 (2011) 112-118.

[15] H. Muroyama, C. Saburi, T. Matsui, and K. Eguchi, Ammonia decomposition over Ni/La_2O_3 catalyst for on-site generation of hydrogen, Applied Catalysis A: General. 443-444 (2012) 119-124.

[16] K. Okura, T. Okanishi, H. Muroyama, T. Matsui, and K. Eguchi, Promotion effect of rare-earth elements on the catalytic decomposition of ammonia over Ni/Al_2O_3 catalyst, Applied Catalysis A: General. 505 (2015) 77-85.

[17] H. Zhang, Y.A. Alhamed, A. Al-Zahrani, M. Daous, H. Inokawa, Y. Kojima, and L.A. Petrov, Tuning catalytic performances of cobalt catalysts for clean hydrogen generation via variation of the type of carbon support and catalyst post-treatment temperature, Int. J. Hydrogen Energy. 39 (2014) 17573-17582.

Chapter 8

ECONOMICAL EVALUATION OF HYDROGEN PRODUCTION FROM AMMONIA

8.1 Introduction

There are several suggested methods for hydrogen production, such as steam methane reforming, electrolysis, and coal gasification, which were mentioned in Chapter 2. Most of these methods are considered for the hydrogen production out of the vehicle. Most of the hydrogen production cost analysis studies in the literature contain hydrogen production capacities appropriate for the use in “hydrogen filling stations”. The hydrogen produced in these large scale units are designed such that the hydrogen produced will be filled to the storage tank of the vehicle afterwards. However, as mentioned in Chapter 2 and also in the following sections, this requires special methods of hydrogen filling to the vehicle and also the storage of hydrogen as liquid faces some safety problems. For this reason, in this thesis it is suggested to use ammonia as a fuel carrying the hydrogen to be used in vehicles, aiming to be converted to hydrogen on-board.

In this chapter first of all, a brief literature review is provided about hydrogen production costs by various methods. Hereafter, two main cases for cost analysis are investigated. The first case is that ammonia is used as a storage molecule and is used to transport hydrogen to the filling stations. In these filling stations ammonia should be converted to hydrogen at high H_2 production capacities, such as 1000 kg H_2/ day. The second case is for the utilization of ammonia as a direct fuel where it will be fed to the storage tank of a vehicle directly and will be converted to hydrogen on-board to run the vehicle. The cost analysis calculations will be conducted by using the highly active and stable modified red mud (MRM) based catalyst introduced in Chapter 7 (MRM-700R@700). Furthermore, the comparison of MRM-700R@700 catalyst and Ni- and Ru-based catalysts will be investigated.

8.2 Hydrogen Production Processes and Costs

The fossil fuel based natural gas (mostly CH_4 (methane)) can be used to obtain H_2 by natural gas reforming. Additional chemical processes for natural gas are partial oxidation and auto thermal reforming. Currently steam methane reforming is the most efficient, economical and widely used method. 95% of H_2 produced in the U.S. is produced by steam methane reforming [1]. This method has been used widely for decades in refineries and chemical industries. Even if steam methane reforming has lower greenhouse gas emissions compared to gasoline, CCS (carbon capture and storage) should be also employed for steam methane reforming. In steam methane reforming steam reacts with water vapor at high temperature and forms syngas. Syngas reacts with water to form CO_2 and H_2 by the water gas shift reaction. Even if steam methane reforming has lower greenhouse gas emissions compared to gasoline, CCS (carbon capture and storage) should be employed. For steam methane reforming system in large scale, high efficiencies and low costs are achieved but for small scale production due to the high cost of units, the process becomes less efficient and more costly. Hydrogen production cost by natural gas reforming at a very high capacity (approximately 170 000 kg H_2/day) is estimated according to Sherif *et al.*, as 1.46 \$/kg H_2 [2]. According to a report of IEA [3], similar production costs were found, such as 1.20-1.45 \$/kg H_2. These studies were conducted by detailed models. Penner claims that the production of hydrogen by steam methane reforming is most dependent on natural gas price [4] resulting in the following relatively simple relation.

$$H_2 \text{ [\$/kg]} = 0.286 \times \text{NG price [\$/MMBtu]} + 0.15 \quad \text{(equation 2)}$$

By setting the natural gas price of 2016 in USA [5], H_2 production cost becomes 1.00 \$/kg H_2 which is rather a rough estimate. DOE predicts [6] H_2 production costs as 2.00 \$/kg H_2 at a production scale of 1500 kg/day and expects this value to drop if natural gas prices drop below 5 \$/MMBtu as one can also see from the prediction of Penner in equation 2. These values make it feasible to produce hydrogen for fueling stations since these cost values can compete with gasoline. Reforming technology can be used also for bio-derived liquids such as ethanol. This resource suffers from high capital cost. However, this approach can lower significantly the greenhouse gas emission and dependency on fossil fuels. There are also some limitations, such as excess water use to hinder coking of the catalyst. Bioethanol reforming at a station capacity of 1500 kg H_2/day has a hydrogen production cost of 4.2-6.5 \$/kg H_2 [7].

Coal is one of the most attractive sources due to its low cost and abundance. Coal gasification process converts solid carbon to syngas by the addition of heat and water. Even if coal gasification is a mature process, it is more complex than steam methane reforming which results in higher costs [8]. Capital investment is one of the most important factors effecting cost. The cost is calculated as 2.04-2.41 \$/kg H_2 at 80% efficiency for a 6000 ton coal/day capacity with a capital cost of approximately 1 250 000 000\$ [9]. This high capital cost is mostly due to the integrated CCS which is a need to be implemented because of environmental issues. Biomass gasification is another method which can be done by the same method. Since the source of carbon is renewable, a smaller carbon foot print is achieved. However, other issues such as feedstock cost are relatively high.

Electrolysis of water is another option for hydrogen production where water is split into O_2 and H_2 using electricity. Its greatest benefits are zero carbon emission but it should be noted that this is only achievable if the electricity used for this technology is supplied by solar or wind energy [6]. The cost is largely affected by electricity costs. Hydrogen production costs are estimated as 3.61 \$/kg H_2 [3] and 4.20 \$/kg H_2 [6]. Even for a very high capacity (approximately 170 000 kg H_2/day) electrolysis based hydrogen production costs are still very high such that for electrolysis run with wind power it is 2.5 $/kg H_2 and for a plant run with solar thermal power it is determined as 4.7 $/kg H_2 [2]. For a lower capacity of 1500 kg H_2 /day a cost of 5-8 $/kg H_2 is calculated for electrolysis [7]. 80% of the cost for hydrogen production by electrolysis is determined by electricity price [10]. Silversand [11] showed in his calculations for H_2 production cost that electrolysis is the most costly method having also the highest capital cost. Silversand [11] emphasized that electrolysis has the highest sensitivity to electric-feedstock prices. According to Figure 8.1 the capital cost will add very little to production cost and it is very important to have a cheap feedstock. According to the sensitivity figures it is clear that electrolysis is not a feasible candidate to be used in the near future.

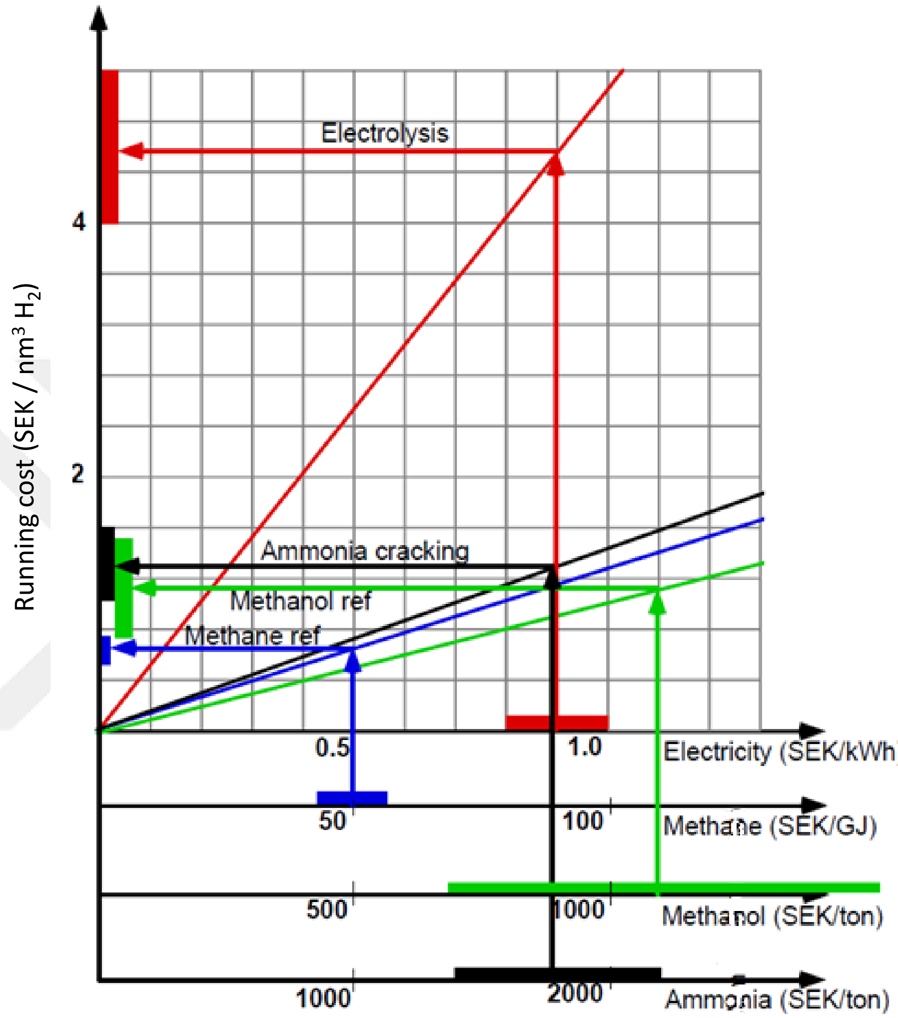

Figure 8.1. Comparison of running cost for various hydrogen production methods showing the sensitivity of fuel and electric prices [11]. (SEKis the abbreviation for Swedish Krona.)

Other methods which are still in development and cost estimates are premature are solar thermochemical water splitting, photoelectrochemical water splitting, photobiological hydrogen production and fermentation [6].

As the cases for steam methane reforming, coal gasification, biofluid reforming and electrolysis show, steam methane reforming and coal gasification has the lowest costs.

However these methods have still enormous greenhouse gas emissions and uses fossil fuels as resource. Electrolysis seems only environmental friendly option if the electricity is obtained totally from wind or solar energy which increases the costs substantially.

As it can be inferred from the brief literature review, most emphasis was put on hydrogen production by either fossil fuel based sources or by electrolysis (which is also indirectly fossil fuel based according to the electricity production method). In the following section a rough estimate about the hydrogen production cost by ammonia decomposition will be calculated in order to make a comparison with the above mentioned methods and corresponding costs.

8.3 Cost Estimation for Hydrogen Production by Ammonia to be used in Filling Stations

A Lindberg ammonia cracker is selected as the reactor producing 273 kg/day with an electrical power consumption of 140 kW having a weight of 5800 kg which has a cost of 155 000$ [12]. By employing four of these reactors 1092 kg H_2/day can be produced with a capital cost of 620 000$. This capital cost is also reasonable according to the estimation of the DOE report on ammonia for hydrogen production [13] and Silversand [11]. By assuming a lifetime of 10 years, the capital cost becomes 0.16$/kg H_2. Since ammonia decomposition by assuming 75% conversion (which is a common estimate for ammonia cracking units) and to produce 1092 kg H_2/day, 8250 kg NH_3/day should be processed. By using an ammonia price of 300 $/ton NH_3 [14], running cost due to ammonia price becomes 2.27 $/kg H_2. Since one unit will consume 140kW energy and by assuming 6.5 cent electricity price per 1 KWh [15], electricity for four units at an electricity cost of 0.8 $/kg H_2 is emerging. By adding up capital, electricity, and ammonia cost, a total cost of 3.2 $/kg H_2 is calculated which is in accordance with DOE estimation [13]. However, it should be noted that no catalyst cost was added since it was assumed that MRM catalyst investigated in Chapter 7 (MRM-700R@700) has no cost. For 75% conversion, approximately 1.8 kg catalyst is needed to produce 1092 kg H_2/day.

According to the experiments in Chapter 7, MRM-700R@700 has the capability of producing hydrogen at very high gas hourly space velocity values. If, on the contrary to the suggested 75% cracking efficiency, 100% efficiency is assumed in the above calculations, it is possible to produce hydrogen by using 5 kg of MRM-700R@700 catalyst. This would drastically decrease the running cost because of ammonia. Since less ammonia is needed under 100% conversion condition, running cost due to ammonia becomes 1.7 $/kg H_2 produced which ends up at a total cost of 2.65 $/kg H_2 which is very close to the target of DOE [13]. All mentioned calculations and cost determinations are summarized in Table 8.1. As seen in Table 8.1 increasing efficiency by increasing catalyst amount to be utilized does not add any cost to the system. It can be even considered that the usage of red mud (RM) may be even advantageous with economical gain for an aluminum production plat producing RM as waste. Because, these plants pay certain amount of penalty to the government every year for the disposal and/or storage of RM, which also comes with serious environmental impact.

Table 8.1. Summary of cost estimation for hydrogen production by ammonia.

	Capacity	**1092 kg H_2/day**	
	Lifetime	10 years	
	Capital cost	620 000 $ (4 Lindberg ammonia Crackers)	0.16 $/kg H_2
	Electricity cost	140 kW power consumption per cracker, 0.065$/kWh electricity cost	0.8 $/kg H_2
(75% efficiency)	Operating cost due to ammonia	Price of ammonia is 300$/ton	2.27 $/kg H_2
	MRM-700R@700 catalyst amount	1.8 kg	-
	Total cost	Capital + Electricity + Operating	**3.22 $/kg H_2**
(100% efficiency	Operating cost due to ammonia)	Price of ammonia is 300$/ton	1.70 $/kg H_2
	MRM-700R@700 catalyst amount	5.1 kg	-
	Total cost	Capital + Electricity + Operating	**2.65 $/kg H_2**

8.4 Comparison of Ru- and Ni- based Catalyst with MRM-700R@700 for on-Board Generation of Hydrogen

As generally modeled in the literature and also up to here, the hydrogen production by ammonia in fueling stations or small capacity plant scale was conducted. BMW presented the first hydrogen-powered car “BMW Hydrogen 7” having a liquid hydrogen fuel tank that takes up 8 kg which corresponds to approximately 170 liters [16]. Since hydrogen is stored at liquid in this car filling stations of several specifications are proposed by BMW. The calculations made up to this point is for the scenario if hydrogen is filled directly to the car by hydrogen filling stations as proposed by BMW. However, this method has several disadvantages for the usage in daily life. These disadvantages of hydrogen tank filling process are listed below.

- The car should be parked in a certain position,
- Battery voltage should be sufficient,
- No gas or crash warning should be detected by the car,
- Fuel tank level should not be higher than 80%,
- The pressure in the tank should not be less than 5.5 bar,
- The filler flaps should be fully open,
- The leakage test on the tank coupling should be successfully completed,
- Entire process takes 8 minutes [17].

As seen above, all of these steps are dangerous when compared to gasoline filling and takes 8 minutes to be completed. One advantages of this process may be that some of these steps and the actual filling of hydrogen trough the pipes are fully automatic. Nevertheless, this may arise other problems because if an electronic error occurs, the outcome may be fatal. This is why ammonia is suggested as a direct fuel and carrier of hydrogen.

First of all the unit prices of Ru- and Ni- based catalysts are determined to show the catalyst cost and needed catalyst amount calculations. In Table 8.2 the cost for Ru- and Ni-based catalysts are determined on a basis of $/kg. As seen while Ru has unit price of 1.35 $/kg, Ni has a unit price of 800$/ton. When considering the cost on atomic base, 1 Ni atom has an atomic mass of 58.7 amu whereas Ru has an atomic mass of 101 amu. While Ni is 1700 times cheaper than Ru on $/kg basis, it also supplies nearly twice more active sites per unit mass. Another important cost factor for the best performing Ru catalyst is the high cost due to CNT support.

Table 8.2. Cost comparison of Ru and Ni based catalysts

MRM-700R@700			Ni based catalyst (Ce10-NiO-SiO_2-350) [18]			Ru based catalyst (KNO3–Ru/CNTs (2:1) [19]		
Compounds	wt.%	Unit price	Compounds	wt.%	Unit price	Compounds	wt.%	Unit price
Fe	35.4	-	Ni	49.5	10.44 $/ton[20]	Ru	4.8	1.35 $/g [21]
Al_2O_3	17.8	-	CeO_2	10	298 $/kg[22]	KNO_3	9.6	800 $/ton [23]
SiO_2	17.2	-	SiO_2	40.5	0.6 $/kg[24]	CNT	85.6	200 $/kg [25]
Total catalyst cost ($/kg)		-	Total catalyst cost ($/kg)		30 $/kg	Total catalyst cost ($/kg)		236 $/kg

Secondly, an appropriate H_2 production capacity should be determined to be able to provide the same hydrogen amount to run the car by ammonia. BMW Hydrogen 7 consumes 3 kg H_2/ 100 km [17]. Assuming that the car is driven at a speed of 100 km/h for one hour, an estimation that the car will consume 3 kg H_2/h is appropriate which is in accordance with the literature [16]. All catalyst cost calculations are based on this capacity.

By using the catalyst costs determined, in Table 8.2, cost for various catalysts for filling station capacity (approximately 1000 kg H_2/h) and on-board use capacity (3 kg/h) is given. Other than capacity, cracking efficiency (conversion) and working temperature variations are also shown to represent several operating scenarios.

Table 8.3. Comparison of MRM-700R@700, Ru and Ni based catalyst for various working conditions.

Catalyst	Capacity / kg/day	Conversion / %	GHSV / cm^3 NH_3 h^{-1} g_{cat}^{-1}	H_2 production / mmol H_2 min^{-1} g_{cat}^{-1}	T /°C	Catalyst amount / kg	Catalyst cost / $
MRM-700R@700	1092	100	72000	72	700	5.14	-
		75	270327	200	700	1.83	-
	3	100	72000	72	700	0.34	-
		75	270327	200	700	0.12	-
Ni	1092	100	30000	33.24	650	12.3	370
		75	30000	29.09	600	16.4	494
	3	100	30000	33.24	650	0.81	24
		75	30000	29.09	600	1.08	33
Ru	1092	100	60000	67.1	500	6.2	1456
		75	60000	49.1	400	8.2	1941
	3	100	60000	67.1	500	0.41	96
		75	60000	49.1	400	0.54	128

According to Table 8.3, the cost of Ru-based catalyst and Ni-based catalyst at 100% conversion for a capacity of 1092 kg H_2/day is 1456 and 370 \$, respectively. Furthermore the cost of f Ru-based catalyst and Ni-based catalyst at 100% conversion for a capacity of 3 kg H_2/day (on-board hydrogen production capacity) is 96 and 24 \$, respectively. From these results it is shown that, Ru has the highest cost of catalyst as expected. Even if the Ni-based catalyst contains around 50% metal, it has a significantly lower cost. RM was assumed to have no cost. It was possible to compare the catalyst costs for 75% and 100% conversion at the same temperature for MRM-700R@700. However due to limited availability of data, the 75% conversion values for Ru- and Ni- based catalyst were obtained at different temperatures. One may expect that the catalyst amount used and catalyst costs should drop for Ru- and Ni-based catalysts for lower efficiency values on the contrary to the results in Table 8.3. However it should be noted that the temperature is also lower for 75% conversion condition. This lower temperature value may be advantageous to drop operating cost (electricity etc.) for high capacity systems. However for on-board generation in a car where an internal combustion engine consumes hydrogen, attempts for lowering temperature is not as necessary as for high capacity conditions. Lowering temperature and producing H_2 with only 75% conversion would also need necessary separation system which would require additional capital cost. To sum up, the catalyst produced from red mud is superior to Ru and Ni-based catalysts in terms of cost and environmental aspects.

8.5 Conclusion

H_2 production cost by NH_3 for large scale (approximately 1000 kg H_2/kg) was determined to be able to make a comparison with other hydrogen production methods. The H_2 production cost by ammonia was determined as 3.22 \$/kg H_2 for 75% conversion and as 2.65\$/kg H_2 for 100% conversion. An important factor is that there is no need to add any catalyst cost if MRM-700R@700 catalyst is used. According to the literature, H_2 production cost by steam methane reforming, coal gasification and electrolysis were determined as 1.20-1.45, 2.04-2.41, and 3.61 $/kg H_2, respectively. Coal gasification and steam methane reforming are prior to ammonia decomposition in terms of cost for large scale production at filling stations. However, ammonia possess other advantages, such as it is non-carbon containing, has an already existing infrastructure, is one of the most known chemicals and can be stored easily in vessels which enables the transportation of hydrogen safely. The cost of H_2 production by ammonia depends most on NH_3 price. If the price of NH_3 would drop to 100 $/ton the total cost for hydrogen production at a capacity of 1092 kg/day and 100% efficiency would drop to 1.5 $/kg H_2. Similarly if NH_3 price would increase to 700 $/ton -as it was in 2012[14]- the cost would increase to 4.9 $/kg H_2.

Considering a small scale, on-board generation of hydrogen by ammonia, MRM-700R@700 catalyst is an excellent option to be used. Because it does not add any cost to the system, unlike the cases with such as Ru- or Ni- based catalyst. The requirement of high temperature (700 °C) can be also accomplished due to the presence of an internal combustion engine which is already providing high temperatures in the on-board system. Therefore, the low working temperature of the best performing Ru catalyst, does not seem attractive due to its very high cost even though it performs well at low temperatures, such as at 500 °C. The usage of Ni-based catalyst still has significant costs since it has a lower activity a higher amount of it is needed. It should be noted that the catalyst cost calculated in Section 8.4 was not added to the total cost determined in Section 8.3. Since, these catalysts are still under investigation in laboratory scale and it is hard to determine the life time of both Ru and Ni-based catalyst. So it is challenging to estimate a lifetime for these catalysts. If the catalyst would not deactivate for a long period, such as 5 or 10 years, catalyst cost would affect the total cost on hydrogen production very weakly. However, if the catalysts should be changed each year a significant cost would occur due to the catalyst for both Ru- and Ni- based catalysts for either a large capacity or on-board hydrogen production capacity. However, there is no cost associated with MRM-700R@700 catalyst. The utilization of the industrial waste RM as a catalyst would both overcome the catalyst cost problem for the on-board hydrogen production by ammonia and would also serve as an environmentally friendly solution to the recycling of a hazardous waste.

References

[1] Hydrogen Production: Natural Gas Reforming. Retrieved from http://energy.gov/eere/fuelcells/hydrogen-production-natural-gas-reforming

[2] S. Sherif, T. Veziziglo, and F. Barbir, 1999, "Hydrogen Energy Systems," Wiley Encyclopedia of Electrical and Electronics Engineering, vol. 9, J. G. Webster (Editor), New York: John Wiley & Sons, pp. 370-402.

[3] Hydrogen Production & Distribution. Retrieved from https://www.iea.org/publications/freepublications/publication/essentials5.pdf

[4] S.S. Penner, Steps toward the hydrogen economy, Energy. 31 (2006) 33-43.

[5] Natural Gas Weekly Uptake. Retrieved from http://www.eia.gov/naturalgas/weekly/

[6] Hydrogen Production Technical Roadmap. Retrieved from http://www1.eere.energy.gov/vehiclesandfuels/pdfs/program/hptt_roadmap_june2013.pd

[7] J.J. Hwang, Sustainability study of hydrogen pathways for fuel cell vehicle applications, Renewable and Sustainable Energy Reviews. 19 (2013) 220-229.

[8] Hydrogen Production and Storage. Retrieved from https://www.iea.org/publications/freepublications/publication/hydrogen.pdf

[9] Production of High Purity Hydrogen from Domestic Coal: Assessing the Techno-Economic Impact of Emerging Technologies. Retrieved from http://www.netl.doe.gov/energy-analyses/pubs/H2fromcoaltech2010.pdf

[10] Current (2009) State-of-the-Art Hydrogen Production Cost Estimate Using Water Electrolysis. Retrieved from https://www.hydrogen.energy.gov/pdfs/46676.pdf

[11] F. Silversand, Catalytic Heat Exchangers for small-scale production of hydrogen – feasibility study. Retrieved from http://www.sgc.se/ckfinder/userfiles/files/SGC129.pdf

[12] T. Lipman, and N. Shah, Ammonia as an Alternative Energy Storage Medium for Hydrogen Fuell Cells: Scientific and Technical Review for Near-Term Stationary Power Demonstration Projects. Retrieved from http://www.intpowertechcorp.com/NH3_Cracker.pdf

[13] G. Thomas, and G. Parks, Potential Roles of Ammonia in a Hydrogen Economy. Retrieved from https://www.hydrogen.energy.gov/pdfs/nh3_paper.pdf

[14] Weekly Ammonia Spor Price, 2016. Retrieved from http://marketrealist.com/2016/03/ammonia-prices-hit-bottom/

[15] Electric Power Monthly, 2016. Retrieved from https://www.eia.gov/electricity/monthly/epm_table_grapher.cfm?t=epmt_5_6_a

[16] T. Wallner, H. Lohse-Busch, S. Gurski, M. Duoba, W. Thiel, D. Martin, and T. Korn, Fuel economy and emissions evaluation of BMW Hydrogen 7 Mono-Fuel demonstration vehicles, Int. J. Hydrogen Energy. 33 (2008) 7607-7618.

[17] BMW Hydrogen 7. Retrieved from http://www.wired.com/images_blogs/autopia/files/bmw_hydrogen_7.pdf

[18] L.-F. Zhang, M. Li, T.-Z. Ren, X. Liu, and Z.-Y. Yuan, Ce-modified Ni nanoparticles encapsulated in SiO2 for COx-free hydrogen production via ammonia decomposition, Int. J. Hydrogen Energy. 40 (2015) 2648-2656.

[19] S.J. Wang, S.F. Yin, L. Li, B.Q. Xu, C.F. Ng, and C.T. Au, Investigation on modification of Ru/CNTs catalyst for the generation of COx-free hydrogen from ammonia, Applied Catalysis B: Environmental. 52 (2004) 287-299.

[20] Nickel Price, 2016. Retrieved from http://www.infomine.com/investment/metal-prices/nickel/all/

[21] Ruthenium Price, 2016. Retrieved from http://www.infomine.com/investment/metal-prices/ruthenium/5-year

[22] CeO_2 price, 2016. Retrieved from https://www.alibaba.com/showroom/price-of-cerium-oxide-ceo2.html

[23] KNO_3 price, 2016. Retrieved from https://www.alibaba.com/showroom/potassium-nitrate.html

[24] Fumed SiO_2 price, 2016. Retrieved from https://www.alibaba.com/showroom/fumed-silica-price.html

[25] CNT price, 2016. Retrieved from https://graphene-supermarket.com/Multi-Walled-Carbon-Nanotube-Powder-100-gram

Chapter 9

CONCLUSIONS AND FUTURE WORK

The need for clean energy has been one of the most important issues in the last decades. One of the solutions suggested to overcome this problem is the use of CO_2-free hydrogen energy and to store and transport it safely and efficiently in ammonia. A cheap and active catalyst is needed to convert ammonia either at filling stations or on-board to hydrogen. Ruthenium catalysts are known as the most active ones for the decomposition of ammonia to hydrogen and nitrogen. However, the high cost and limited availability of it makes it impossible to decrease the catalyst costs.

Red mud (RM) which is an industrial waste produced in vast amount globally causes a huge environmental problem. It contains significant amounts of valuable components and finds therefore several application areas, one of which is in catalysis. A few studies showed that RM can be used as a support material to metal nanoparticles for ammonia decomposition. However, it is clear that only lowering the support material cost which is already very low when comparing to Ru, does not have a great effect on cost. The high iron oxide content of RM makes it an ideal candidate to utilize it as a catalyst itself.

In the first part of this study, RM and modified red mud (MRM) samples prepared by treating RM under simple conditions were characterized deeply. The changed parameters were the acid type, molarity of the acids, digestion temperature and calcination temperature. Modifications resulted in increased surface area and increased Fe_2O_3 content which are both desirable changes if RM will be utilized as a catalyst. Furthermore, acid molarity increase caused a linear increase in pore sizes for HCl treated samples, whereas it linearly decreased for H_2SO_4 treated samples. This fact is enabling to tune pore size properties of RM. An acid digestion temperature of 220 °C was proposed to digest RM in acid solution on the contrary to the literature where acid digestion was mostly performed at a digestion temperature of 85 °C. Since RM mostly needs to be modified before using it, this work provides a guideline for selection of the appropriate treatment methods according to the desired application areas. This study was also important in terms of the detailed characterization of Turkish RM.

In the second part, RM's application in catalysis for ammonia decomposition was investigated. The samples modified in the first part of this study were further treated under varying calcination and reduction temperatures and tested for ammonia decomposition at differential conversion conditions at 500 °C. Among all catalysts MRM-2 showed an exceptionally high activation energy indicating that this catalyst is extremely sensitive to temperature. This sample was further investigated at 700 °C and compared with other iron-based catalysts in the literature. MRM-700R@700 (MRM-2 in Chapter 4) provided hydrogen production rates of 72 and 196 mmol H_2 min^{-1} g_{cat}^{-1} for the corresponding space velocities of 72 000 and 240 000 cm^3 NH_3 h^{-1} g_{cat}^{-1}, respectively at 700 °C. This value is the highest ever reported for an iron based catalyst for ammonia decomposition. Furthermore, in this study the active species responsible for this stable and high activity were investigated deeply. It was determined that during the activation period under NH_3, the iron contained in MRM-700R is changing to iron nitride species of different nitriding degrees (Fe_xN). The iron to nitrogen ratio in these species is determined by the activation temperature and duration. It was elucidated that an activation period of 10 hours at 700 °C under NH_3 flow causes the formation of ε-Fe_2N species in the MRM-700R@700 catalyst, which is responsible for this high performance.

MRM-700R@700 showed superior activity to all other Fe-based catalysts in the literature and also can compete even with Ru-based catalysts at high temperatures. Even though iron is a non-noble metal and seems also applicable in ammonia decomposition due to its low cost, a significant cost may come due to the support material or synthesis technique such as the iron phthalocyanine-based catalyst or the Fe_2O_3/CMK-5 catalyst from the literature mentioned in Chapter 7. The latter one was known as the best performing iron-based catalyst suffering highly from stability problems. RM containing high amounts of valuable compounds with severe envrinmental impact can be utilized as a highly active catalyst. In addition to the utilization of a hazardous waste, using this high performing industrial waste based catalyst can pave the way for the on-board hydrogen generation for ammonia, providing clean energy for transportation by lowering greenhouse-gas emissions. By the cost analysis it was shown that, using cost-free MRM-700R@700 is highly feasible for on-board hydrogen generation.

In this study the aim was investigating the highest performing catalyst among all MRM samples prepared and elucidating the reasons for this high performance. For future work, the performances of other MRM samples will be correlated to chemical and physical characteristics. As investigated in Chapter 5, characteristics, such as pore volume, surface area and iron content varies significantly in these samples which may have effects on the performances. By characterizing the catalysts before and after reaction, differences in iron nitride phases and their nanoparticle sizes can be also investigated to establish a correlation between these and catalytic activity. Furthermore, other parameters of the modification of RM, such as the temperature of digestion, the exposure time of RM to acid in the acid digester, the amount of RM used for a certain amount of acid can be tuned for producing a more desirable MRM sample having higher iron content or a more porous structure.

Finally, as a future work in a different direction with the aim of utilizing RM and its modified counterparts, one can focus on investigating different reactions for which exceptionally high iron content of RM and/or MRM can help to reach high catalytic performance.